X–Ray Investigation of Ultra–Thin Spin–Crossover Molecular Films

LALMINTHANG KIPGEN

Dissertation
zur Erlangung des Grades eines
Doktors der Naturwissenschaften (Dr. rer. nat.)

Am Fachbereich Physik
der Freien Universität Berlin

Berlin, im Februar 2019

Tag der Disputation: 09. Mai 2019
1. Gutachter: Prof. Dr. Wolfgang Kuch
2. Gutachter: Prof. Dr. Katharina Franke

ABSTRACT

This thesis concerns with the investigation of two closely-related spin-crossover molecules (SCMs) — [Fe(H_2B(pz)$_2$)bipy] (pz = pyrazole; bipy = 2,2′-bipyridine) and [Fe(H_2B(pz)$_2$)phen] (phen = 1,10-phenanthroline) — and their derivatives in submonolayers and in ultra-thin films deposited mainly on a highly-oriented graphite (HOPG) substrate (apart from Au(111) and Bi(111) substrates) with the aim of gaining insight into the fundamental processes governing the spin switching in such systems, using x-ray absorption spectroscopy (XAS).

In a submonolayer of the SCM [Fe(H_2B(pz)$_2$)bipy] deposited on an HOPG substrate, x-ray-induced HS→LS transition, termed as reverse-SOXIESST, is observed at 5 K for the first time — apart from the observation of soft x-ray-induced excited spin-state trapping (SOXIESST) already reported in the literature for the bulk material. The switching rates are found to be highly dependent upon the photon fluxes. This observation is rationalized as the spin switching processes being essentially caused by the interaction between the x-ray-induced secondary electrons and the molecules. The observed SOXIESST and reverse-SOXIESST phenomenon is analogous to light- and electron-induced spin switching reported in the literature. Both thermal- and light-induced spin transition of [Fe(H_2B(pz)$_2$)bipy] deposited on an HOPG substrate in coverage ranging from submonolayers to multilayers (of up to 10 monolayers (ML)) is systematically probed for cooperative effects and its evolution. In the thermal-induced spin transitions, the submonolayers exhibit an apparent anticooperativity, while a free-molecule-like behaviour is indicated at the monolayer; yet, the multilayers, starting from the double-layer, evidenced cooperativity in their spin-transition processes, with the interaction energy increasing to about 60% of the reported bulk value for the 10-ML sample. The light-induced spin transitions — albeit highly efficient — are free from cooperative effects. The photo-induced metastable HS state of the submonolayers at low temperatures is highly unstable, and showed a clear departure in the mode of spin relaxation from the bulk material.

The SCM [Fe(H_2B(pz)$_2$)phen] is methylated with two ([Fe(H_2B(pz)$_2$)$_2$(phen−me$_2$)]) and four ([Fe(H_2B(pz)$_2$)$_2$(phen−me$_4$)]) methyl compounds at the phen ligand. The daughter molecules exhibit spin-crossover behaviour entirely different from the parent molecule upon contact with an HOPG surface; while [Fe(H_2B(pz)$_2$)phen] is found to undergo complete spin transition with light and temperature, about 50% of [Fe(H_2B(pz)$_2$)$_2$(phen−me$_2$)] molecules are trapped in the HS state within the accessible temperature range; [Fe(H_2B(pz)$_2$)$_2$(phen−me$_4$)] molecules lose their spin-crossover behaviour altogether upon contact with the HOPG surface. Similar spin-crossover behaviour is exhibited by the parent and the daughter molecule [Fe(H_2B(pz)$_2$)$_2$(phen−me$_2$)] on Au(111) and Bi(111) substrates: both the molecules undergo decomposition, resulting in the loss of spin-crossover on Au(111), while just about 50% of both types of molecules retain their spin-crossover on Bi(111) substrate.

KURZFASSUNG

Diese Arbeit befasst sich mit der Untersuchung zweier eng miteinander verwandter Spin-Crossover Moleküle (SCM) [Fe(H_2B(pz)$_2$)bipy] und [Fe(H_2B(pz)$_2$)phen] und ihrer Derivate, welche in Submonolagen und ultradünnen Schichten auf hochorientiertem pyrolytischem Graphit (HOPG), sowie auf Au(111) und Bi(111) als Substrat aufgebracht wurden. Mit Hilfe von Röntgenabsorptionsspektroskopie (XAS) werden Erkenntnisse über fundamentale Prozesse beim Schalten der Spinzustands in diesen Systemen erlangt.

In Submonolagen des SCM [Fe(H_2B(pz)$_2$)bipy] auf HOPG bei 5 K werden erstmalig röntgeninduzierte HS→LS–Übergänge, hier reverse-SOXIESST genannt, beobachtet, neben dem aus der Literatur für Festkörper aus Spin-Crossover Molekülen bereits bekannten, durch weiche Röntgenstrahlung induzierten Excited Spin-State Trapping (SOXIESST). Die beobachteten Schaltraten hängen stark vom Photonenfluss ab. Diese Beobachtung wird damit erklärt, dass der Spin–Schaltprozess hauptsächlich durch die Wechselwirkung von röntgeninduzierten Sekundärelektronen mit den Molekülen verursacht wird. Die beobachteten SOXIESST und reverse-SOXIESST Phänomene verhalten sich analog zu licht- und elektroneninduziertem Spin-Schalten wie in der Literatur berichtet. Beide, thermisch und licht induzierte Spin-Schaltvorgänge von [Fe(H_2B(pz)$_2$)bipy] auf HOPG werden systematisch auf kooperative Effekte und deren Entwicklung, u.A. in Abhängigkeit von der Molekülbedeckung - von Submonolagen bis 10 Monolagen - untersucht. In den thermisch induzierten Spin-Schaltvorgängen weisen Sub-Monlagen offenbar Anti-Kooperativität auf, während für die Monolage ein Verhalten wie bei quasi freien Molekülen beobachtet wird. Die Multilagen dagegen, beginnend mit der Doppellage, zeigen Kooperativität in ihren Spin-Schaltprozessen wobei die Wechselwirkungsenergie für die 10-Monolagen-Proben auf bis zu 60% von Literaturwerten für Festkörper zunimmt. Die lichtinduzierten Spin-Schaltprozesse - obwohl hoch effizient - zeigen keinerlei kooperativen Effekte. Der photo induzierte metastabile HS–Zustand der Submonolagen ist bei tiefen Temperaturen sehr instabil und zeigt klare Abweichungen in der Art der Spin-Relaxation gegenüber dem Festkörpermaterial.

Die SCM [Fe(H_2B(pz)$_2$)phen] wurden am phen-Liganden mit zwei ([Fe(H_2B(pz)$_2$)$_2$(phen−me$_2$)]) bzw. vier ([Fe(H_2B(pz)$_2$)$_2$(phen−me$_4$)]) Methyl–Gruppen methyliert. Die Molekülderivate zeigen in Kontakt mit dem HOPG–Substrat ein stark unterschiedliches Spin-Crossover-Verhalten im Vergleich zur Stammverbindung. Während an Fe-phen unter Licht- und Temperatureinfluss ein vollständiger Spin-Crossover beobachtet wird, verbleiben im experimentell zugänglichen Temperaturbereich etwa 50% der [Fe(H_2B(pz)$_2$)$_2$(phen−me$_2$)] Moleküle in HS-Zustand. [Fe(H_2B(pz)$_2$)$_2$(phen−me$_4$)] Moleküle verlieren auf dem HOPG-Substrat ihre Spin-Crossover-Eigenschaften komplett. Ähnliches Spin-Crossover-Verhalten wird bei der Stammverbindung und dem Derivat [Fe(H_2B(pz)$_2$)$_2$(phen−me$_2$)] auf Au(111) und Bi(111) Oberflächen beobachtet: beide Moleküle zerfallen teilweise, was auf Au(111) zum Verlust der Spin-Crossover-Eigenschaften führt während auf Bi(111) jeweils noch etwa 50% beider Molekültypen ihre Spin-Crossover-Eigenschaften behalten.

CONTENTS

"A composer is a guy who goes around forcing his will on unsuspecting air molecules, often with the assistance of unsuspecting musicians."

— Frank Zappa

MOLECULES TO THE RESCUE?

From the invention of microprocessor chips in the 1960s, silicon-based microelectronics (or information technology (IT)) has evolved to become an indispensable part of our lives, encompassing every facet — transportation, commerce, communication, entertainment, health care, and governance. The startling pace of advancement in IT is powered by what is called "Moore's law". In 1965, Gordon Moore — co-founder of Intel Corp. — predicted that the size of transistors on a microprocessor chip will shrink by a factor of two every two years. This prediction — which came to be known as "Moore's law" — has proven to be remarkably accurate for the past 5 decades![1] To appreciate the effect transistor scaling has had on the working of microprocessor chips, consider this: As compared to Intel's first-generation microprocessor chip, 1971 4004, the fifth-generation Core i5 processor launched in 2015 offers 3,500 times more performance, is 90,000 times more energy efficient at about 60,000 times lower cost [1]. (The transistor's feature size of the fifth-generation is $\sim$700 times smaller than that of the first generation; 14 nm and 10 μm feature sizes, respectively. As of May, 2017, IBM claimed to have built the world's first transistor of feature size 5 nm [2].)

Can transistor scaling based on Moore's law go on? Or more pertinently, for how long? In an article in *Nature* (February, 2016), Waldrop writes [3]:

> "Top-of-the-line microprocessors currently have circuit features that are around 14 nanometres across, smaller than most viruses. But by the early 2020s, says Paolo Gargini, chair of the road-mapping organization, even with super-aggressive efforts, we'll get to the 23-nanometre limit, where features are just 10 atoms across. Is that a device at all? Probably not — if only because at that scale, electron behaviour will be governed by quantum uncertainties that will make transistors hopelessly unreliable."

What will be the impact of the demise of Moore's law on human civilization? Well, hitting the dead end of Moores law will not, in itself, be a disaster; but our continued reliance on silicon-based microelectronics (probably) would. To elaborate, here's a quote from Nicola Spaldin, professor at ETH Zürich, Switzerland [4]:

[1] Moore's original prediction was the transistor's size shrinkage by a factor of 2 every year; he revised it to every two years in 1975. Moore's law isn't actually a law — it's more like "rule-of-thump"

> "...silicon revolution will soon be forced to come to an end...while this might not seem so disastrous (certainly the controls on my smartphone are already smaller than I can see without my reading glasses), it is in fact a profound problem for society: As living standards improve in emerging regions and the internet of things becomes more widespread, worldwide use of microelectronics is expanding more rapidly than ever before, so that by most projections more than half of the world's energy will be consumed by information technologies within a couple of decades [5]. And this is not sustainable."

In order to continue along the computing performance and energy-efficiency incremental trajectory of the last 50 years, as well as to sustain our use of IT, it is not hard to see why silicon transistors should be ditched in favour of new materials.

Over the course of the last few decades, a range of new materials have been suggested as potential candidates to replace silicon, such as spintronics — spin, rather than charge is used to process classical as well as quantum information [6–8]; multiferroics — magnetic and electric moments coexist within a single material, and magnetic properties can be controlled electrically [4, 9]; carbon nanotubes [10]; quantum computers — computing devices based on quantum laws [11–13]; topological insulators — insulating in the bulk, but conducting at surfaces [14]. But none have made beyond the laboratory settings so far, except for the application of spintronics in data storage [15]. Recognizing the need to wean away from the existing silicon-based technology, both the EU and the US have recently made significant investments in quantum computing in particular [16–18].

Then, there is *molecular spintronics* — a multidisciplinary research field comprising organic spintronics, molecular magnetism, molecular electronics and quantum computing (Fig. 1) [19, 20].[2] The gist of molecular spintronics is this: to use single or few molecules as functional building blocks for conventional applications and beyond, directly relying on molecular properties or interface properties of molecules and inorganic electrodes.

Such single-molecule-based devices may be superior/advantageous to conventional devices. For a start, devices with a single molecule as an electronic unit will be the ultimate limit of miniaturization. By simple and cheap chemical procedures, the electronic and structural properties of molecules can be more easily varied/tuned and mass-produced than in the case of tuning the electronic units of conventional solid-state devices — which is, of course, done by (rather costly and tedious) lithography techniques. In recent years, research on molecular spintronics has focussed on coupling/depositing molecules on inorganic substrates, and has spawned a new class of research field within molecular spintronics, called molecular spinterfaces. The interest in such systems (inorganic-substrate/molecule) stems

[2] The concept of exploiting the intrinsic properties of molecules for electronics was put-forward for the first time by Aviram and Ratner in the early 1970s. A brief history of molecular electronics can be found in ref. 21

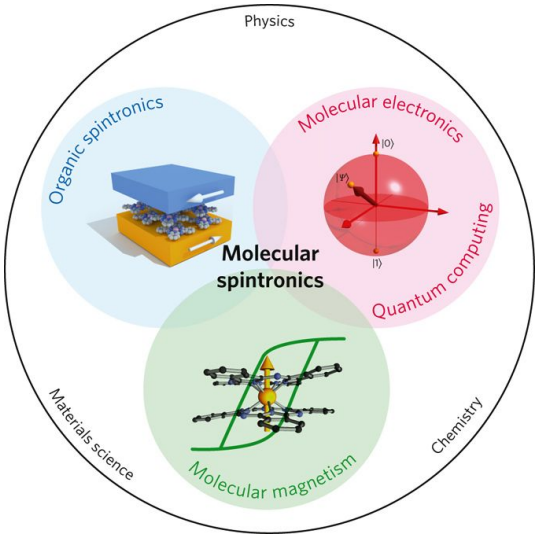

Figure 1: Molecular spintronics. Figure reproduced from ref. 20 with permission

from the fact that entirely new functionalities can be created at the interface(s) of such systems, which can potentially be exploited for practical applications [22–27]. And more crucially, any single-molecule device would necessarily entail connecting a molecule with a solid surface.

The other important aspect is that molecules will bring their intrinsic quantum-mechanical nature — spin, for example — and new functionality(s) that can exploited, which otherwise will not be possible with conventional solid-state devices. Spin-crossover molecules (SCMs) are a case in point. SCMs are a class of molecules consisting of a central transition metal ion — Fe(II) ion in about 90% of known SCMs — surrounded by organic ligands; the molecule can exist in two spin states, commonly referred to as high-spin state (paramagnetic) and low-spin state (diamagnetic for Fe(II)). The molecular spin state can be reversibly switched by subjecting it to light, temperature, pressure, electric or magnetic field, a phenomenon commonly referred to as spin crossover [28]. Plus, a single-SCM exhibits different conductivities at the two different spin states: high conductivity in the high-spin state, and low-conductivity in the low-spin state, with spin-filtering effects [29, 30].

This means that SCMs can be used both as passive and active components in information technology: the two magnetic states can serve as the two different bits for information storage, and varying conductivity behaviour of the two spin states means SCMs can potentially serve as transistors. Using SCMs for storage devices where information can be processed by light (or electric field) promises to be much more energy-efficient than the existing storage devices. [3]

However, the molecules' sensitivity to external stimuli has proven to be a

[3] Energy is dissipated largely in conventional storage devices from controlling the magnetic properties by magnetic field

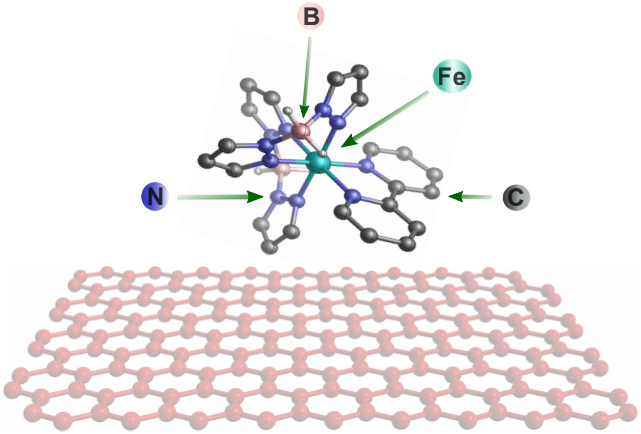

Figure 2: Rendition of the spin-crossover molecule $[Fe(H_2B(pz)_2)bipy]$ deposited on highly-oriented pyrolytic graphite surface. A typical SCM structure has six N atoms (of the organic ligands) in direct coordination with a central transition metal, forming an octahedral geometry

double-edged sword. Spin-crossover molecules are rather fragile, and when they come in contact with solid surfaces – which is a prerequisite for any single-molecule device realization – the spins are quenched in either one or both of the states (coexist), or only a small percentage of the molecules retains its spin-state bistability. The reasons may vary; for one, even an inert surface like gold could cause fragmentation of the molecules, while molecular distortion from the usual octahedral symmetry – responsible for the bistability – due to interaction with surfaces could also result in the loss of bistability. In fact, the coexistence of the spin states on surfaces is so common that it came to be regarded as the true thermodynamic phase.

This thesis presents the complete and reversible switching between the two spin states of the SCM $[Fe(H_2B(pz)_2)bipy]$ deposited on a highly oriented graphite surface, with coverages ranging from submonolayers (about 40% and 80% of a monolayer) to multilayers of up to 10 monolayers, using temperature and light, investigated with x-ray absorption spectroscopy; a rendition of the system is shown in Fig. 2. It is observed that SCMs in reduced dimensions retain much of their behaviour from the bulk material, like exhibiting cooperative effects in the temperature induced, and non-cooperative effects in the light-induced spin transitions. However, the light-induced HS state at low temperatures is highly unstable relative to the bulk-material behaviour. The clean spin-state switching shown here, along with the earlier works by Bernien *et al.* [31], clearly debunked the more prominently held view of the spin-state coexistence as being an intrinsic property of spin-crossover molecules when in contact with solid surfaces, but rather a property dependent upon molecule-substrate combinations.

Realizing electronic/spintronic devices from single or few molecules is still in the exploratory phase, as new physics is being accumulated; this phase is simi-

lar to the period between the conceptual understanding of transistors and the invention of the complementary metaloxidesemiconductor (CMOS) technology that kick-started the microelectronics revolution [19]. And as such, researches that lead to fundamental understanding of the behaviour of multifunctional molecules such as SCMs on solid surfaces will help in realizing molecule-based devices.

*"Excuse me. Are you the Judean People's Front?" F*** off! Judean Peoples Front? Were the Peoples Front of Judea!"*

— Monty Python, Life of Brian

1

SPIN–CROSSOVER MOLECULES

The aim of this chapter is to give a brief introduction to the reader about spin-crossover molecules and its associated phenomena, with emphasis on the processes that have the most relevance in the context of this thesis. The chapter starts with a brief introduction of the basic theory behind the spin-crossover phenomenon — the ligand field theory. It is then followed by a short discussion on the spin transition caused by two of the most commonly used stimuli to induce spin transition (and are used in this thesis) — temperature and light. In view of the importance of the light-induced spin transition, the theory relating to the relaxation of the metastable high-spin state — induced by light illumination at low temperatures — to the low-spin state is also given. The chapter ends with a brief literature overview of the state-of-the-art of the works on the surface-deposited spin-crossover molecular systems.[1]

[1]The terms spin crossover, spin transition and spin switching are used interchangeably in this thesis, albeit some authors used the term spin transition to refer specifically to those spin-crossover molecules (SCMs) that exhibit an abrupt change from one spin state to the other. Likewise, the term bistability is used here to mean the ability of SCMs to exist in two spin states, albeit some authors used the term to mean the presence of hysteresis in the temperature-induced spin transition.

1.1 Introduction

The thermal-induced spin transition — which later on came to be known as spin crossover (SCO) with the two spin states commonly referred to as the high-spin (HS) state and the low-spin (LS) state — was discovered in 1931 by Cambi and co-workers [32] in an iron(III)-based dithiocarbamate complex, but it took about three decades thence until the phenomena came to be fully understood in terms of the ligand field theory. Ewald *et al.* [33] pointed out that the volume change accompanying the spin-state change — larger and smaller volume in the HS and LS states, respectively — *via* an expansion (or contraction) of the metal ligand bond-lengths strongly influence the strength of the electrostatic energy — called the ligand-field energy — acting on the central metal; volume contraction increases the ligand field strength, driving the system to the LS state, while volume expansion decreases the ligand field strength, driving the system to the HS state. The SCO phenomenon was, since then, discovered in complexes based on other transition metals such as Co [34, 35], Mn [36, 37], and Cr [38]. In the following, a brief explanation of the ligand field theory of SCO using Fe(II)-based ($3d^6$) complexes is given. Fe(II)-based spin-crossover molecules are paramagnetic (HS state, $S = 2$) at room-temperature, while diamagnetic (LS state, $S = 0$) at low temperatures (generally ≤ 100 K).

1.1.1 Ligand field theory

The Spin-crossover phenomenon can aptly be called a tale of two energies: energy due to the ligand field and the spin-pairing energy or the electron-electron repulsion. First, consider a free Fe(II)-ion; the 3d orbital is occupied by six electrons, which are, of course, degenerate. But when the Fe(II)-ion is bonded with organic ligands — more specifically for SCMs, six N atoms in direct coordination with the Fe(II)-ion in an octahedral symmetry — the 3d orbital then splits into two energy levels termed as t_{2g} (lower level) and e_g (upper level), with the subset of orbitals d_{xy}, d_{yz}, d_{zx} at the t_{2g} and d_{z^2} and $d_{x^2-y^2}$ at the e_g. This splitting of the 3d-orbital is caused by what is called the ligand field energy — denoted by the parameter 10Dq — produced by the organic ligands surrounding the central Fe(II)-ion.

Depending upon the strength of the ligand field relative to the spin-pairing energy (Δ), the six electrons are distributed in two ways. For the case when $10Dq < \Delta$, Hund's rule of maximum multiplicity is obeyed and the electrons occupy both the energy levels, with the resultant total spin $S = 2$ imparting paramagnetic character to the molecule. On the other hand, if $10Dq > \Delta$, it becomes energetically favourable for electrons to be paired-up and occupy only the lower t_{2g} level resulting in total spin $S = 0$ and a diamagnetic molecule, as depicted in Fig. 1.1.

The competition between the two energies resulting in the change in the molecular spin-state is best depicted by the Tanabe-Sugano diagram [39], as shown in Fig. 1.2. At this point, it is informative to give some background description on the spin-pairing energy or the electron-electron repulsion. For a free transition metal

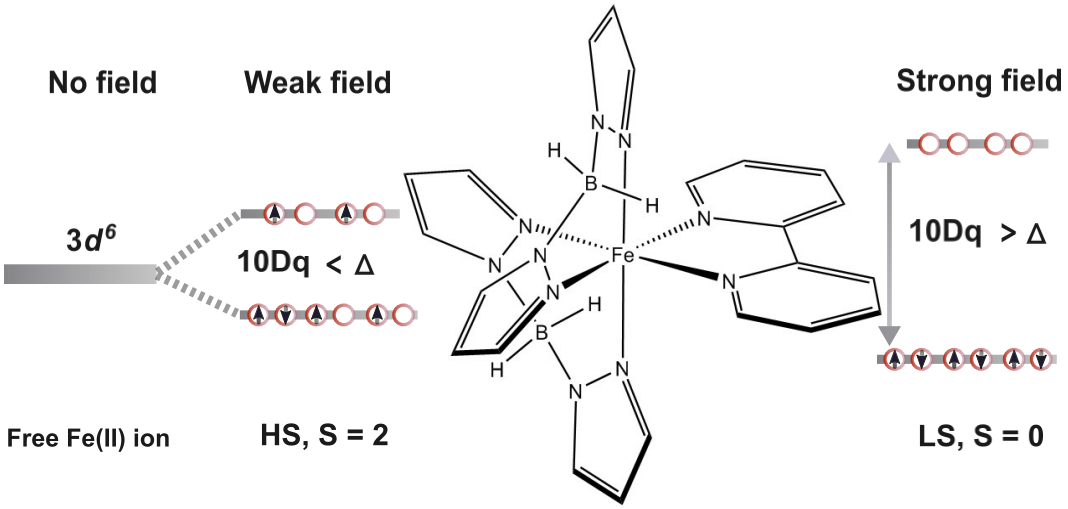

Figure 1.1: Schematic diagram depicting the splitting of the 3d orbitals of an Fe(II)-based spin-crossover molecule by the octahedral ligand field. Depending upon the relative strength of the ligand field (10Dq) to the spin-pairing energy (Δ), the molecule is in the high-spin state (S = 2) or the low-spin state (S = 0). The molecule shown in the Figure is [Fe($H_2B(pz)_2$)bipy]. Note the octahedral coordination of six N atoms to the central Fe(II)-ion — a requirement of spin crossover

ion, the electron-electron repulsion between the d electrons gives rise to a series of states characterized by their spin-multiplicity $2S+1$ and their orbital moment L, and denoted by the term symbol ^{2S+1}L, following the Russel-Saunders coupling scheme. The energies of these states can be calculated using the so-called Racah parameters of electron-electron repulsion, namely, B and C [33].

Back to the Tanabe-Sugano diagram of Fig. 1.2: the electronic energies of the excited states relative to the ground state are depicted as a function of the ligand field strength — with both energies expressed in units of the Racah parameter B. In the absence of the ligand field, the ground state of the metal ion is ^5D, following the Hund's rule. With the introduction of the ligand field — or more specifically, the octahedral ligand field — the ^5D state splits into the ground $^5T_{2g}(t_{2g}^4 e_g^2)$ state, and the excited $^5E_g(t_{2g}^3 e_g^3)$ state; only up-to a critical value of the ligand field, defined as the point where the ligand field parameter 10Dq becomes equal to the spin-pairing energy $\Delta = 2.5B + 4C$ [33], the $^5T_{2g}$ remains the ground state. On further increasing the ligand field strength above the critical value, the $^1A_{1g}(t_{2g}^6)$ state originating from the ^1I free ion term becomes the electronic ground state. In short, for $10\text{Dq} \leq 2.5B + 4C$, the molecule is in the HS state; for $10\text{Dq} > 2.5B + 4C$, the molecule is in the LS state.

The question is: how are the energies modulated in order to change the spin state (or the magnetic character) of the molecule? The spin-pairing energy Δ is unaffected — or changed marginally — from a change in the spin-state; what is being changed significantly is the ligand field strength as a result of the change in the Fe-

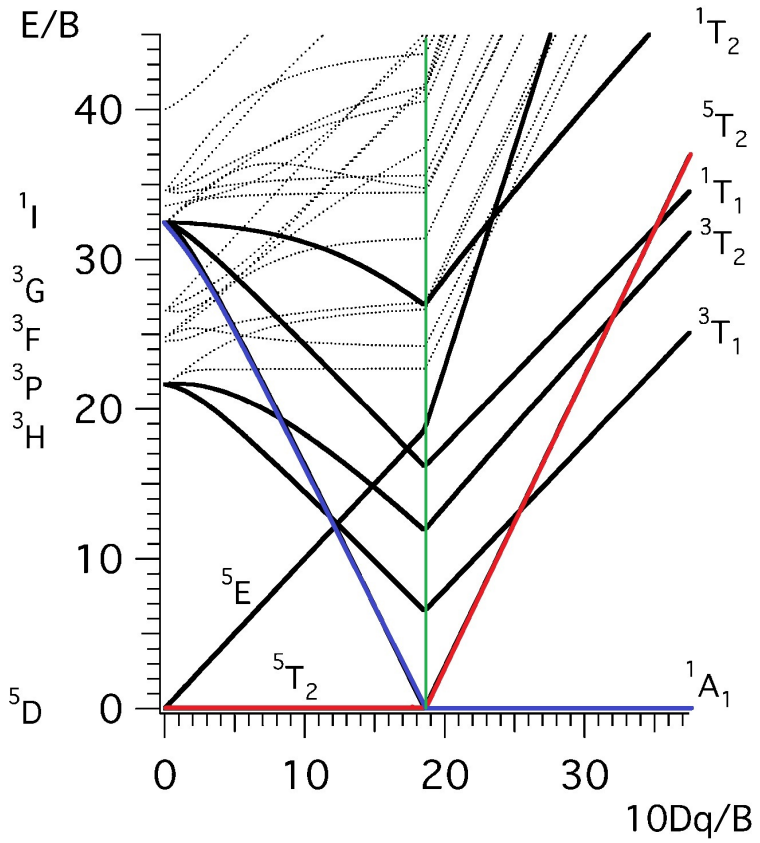

Figure 1.2: Tanabe-Sugano diagram depicting the excited ligand-field states with respective to the ground state, versus the ligand field strength for an Fe(II) ion. Both energies are expressed in units of the Racah parameter B. For the ligand field strength of up-to the critical point — indicated by vertical green line — the ground state is represented by the $^5T_{2g}$ term (HS state, red line); above this critical value, the $^1A_{1g}$ term originating from the ^1I free ion term becomes the ground state (LS state, blue line). Figure adapted from ref. 39

N bond length when the molecule undergoes spin-crossover [33]. SCMs undergo volume contraction and expansion at the LS state and the HS state, respectively — brought about by a the respective decrease or increase in each of the six Fe-N bond lengths by about ≈ 0.2 Å [33]. The relative ligand field strength in the HS and the LS states can be estimated: the parameter defining the ligand field strength 10Dq varies as a function of Fe-N bond length, as r^{-n}, where n = 5-6 [33]. The relative ligand field strength between the two spin states is:

$$\frac{10Dq^{LS}}{10Dq^{HS}} = \left(\frac{r_{HS}}{r_{LS}}\right)^n \tag{1.1}$$

Using average values of $r_{HS} = 2.2$ Å and $r_{LS} = 2.0$ Å, the ratio of the above equation is estimated to be $\sim$1.75. This value have been experimentally verified [33].

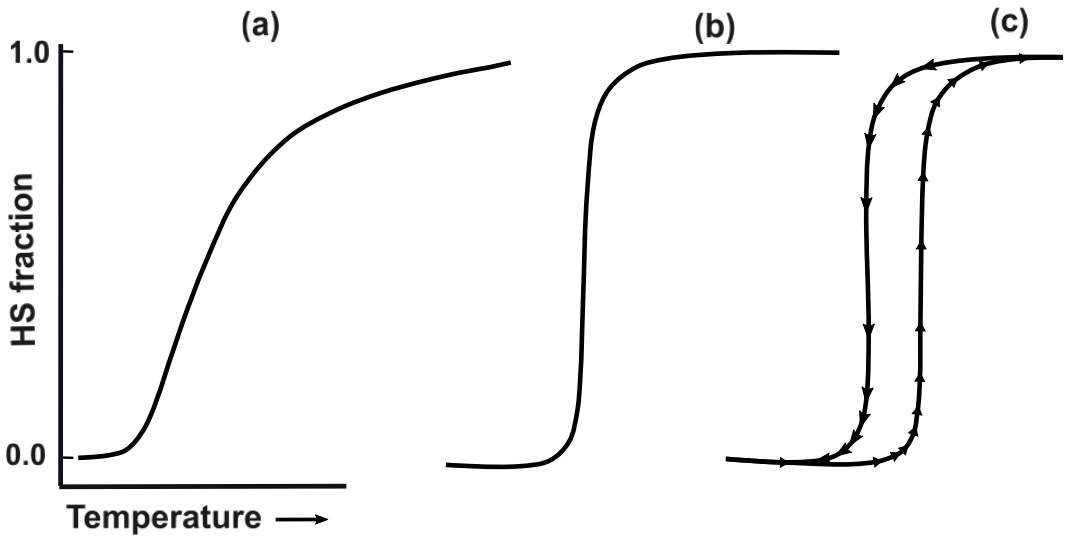

Figure 1.3: Sketch showing different types of thermal-induced spin-transition curves, depending upon the nature of interactions among the molecules during the process. The spin-transition curve shown in (a) could be due to anti-cooperative, non-cooperative, or a rather weak cooperative interactions; the abrupt spin transition as shown in (b) is due to strong cooperative interaction between the spin transiting centres; the hysteresis loop in (c) is due to even stronger cooperative interactions. Arrows indicate direction of temperature change

1.1.2 Thermal-induced spin crossover

The most commonly used stimulus to investigate spin-crossover phenomenon is temperature. The thermal-induced spin-crossover curve may be gradual, abrupt, or exhibit hysteresis loop — akin to a ferromagnetic curve — as shown in Fig. 1.3 (a—c). The thermal spin-crossover curve may even exhibit step-like features for some dinuclear SCMs (but not shown in the Figure) [40]. The form of the curve — gradual, abrupt or hysteresis — is a pointer to the nature of interaction (or non-interaction) of the molecules while undergoing spin transition; for non-interacting or anti-cooperatively interacting molecules, the spin transition is gradual (Fig. 1.3 (a)), or even more gradual in the latter case. On the other hand, the thermal curve characterized by an abrupt (or hysteresis) in the spin transition curve, as shown in Fig. 1.3 (b) & (c), is an indication of strong cooperative interactions between the spin-transiting centres.

In the case of non-interacting molecules, the spin transition can be treated within the framework of the van't Hoff's model, as an equilibrium between two phases, with the transition from one phase to the other driven by the differences in the Gibb's free energy G[2]. Consider a system consisting of N non-interacting SCMs at constant pressure. The Gibb's free energy of the system can be written as:

$$G(T,P,N) = \gamma_{_{HS}}\, G_{HS} + (1-\gamma_{_{HS}})\, G_{LS} - TS_{mix} \tag{1.2}$$

[2] $G(P,T) = H - TS$; H and S being enthalpy and entropy, respectively.

where $G_{HS,LS}$ refers to the Gibb's free energy in the HS and the LS states, respectively; S_{mix} is the entropy of mixing, and $\gamma_{HS,LS}$ refers to the HS and the LS fractions, respectively. The entropy of mixing S_{mix} can be further expressed as:

$$S_{mix} = k_B \ln\left(\frac{N!}{N_{HS}!N_{LS}!}\right) \tag{1.3}$$

Using the Sterling's approximation $\ln(N!) \approx N\ln(N) - N$, the above equation can be written as:

$$S_{mix} = -Nk_B[\gamma_{HS}\ln\gamma_{HS} + (1-\gamma_{HS})\ln(1-\gamma_{HS})] \tag{1.4}$$

At equilibrium, $\frac{\partial G}{\partial \gamma_{HS}} = 0$:

$$\frac{\partial G}{\partial \gamma_{HS}} = \Delta H - T\Delta S + Nk_B\gamma_{HS}\ln\left(\frac{\gamma_{HS}}{1-\gamma_{HS}}\right) = 0$$

The above Equation can be re-arranged as:

$$T = \frac{\Delta H}{\Delta S + Nk_B\ln\left(\frac{\gamma_{HS}}{1-\gamma_{HS}}\right)} \tag{1.5}$$

where $\Delta H = H_{HS} - H_{LS}$ denotes the enthalpy change, while $\Delta S = S_{HS} - S_{LS}$ denotes the entropy change. Using Equation 1.5, the transition temperature $T_{1/2}$ — defined as the temperature at which $\gamma_{HS} = 0.5$ — can be expressed as: $T_{1/2} = \frac{\Delta H}{\Delta S}$.

As already stated in the preceding paragraphs, for spin-crossover molecular systems exhibiting cooperative effects, the nature of interactions can be two-fold — antagonistic or anticooperative interactions, and cooperative interactions. Anticooperative interactions refers to those interactions that promote chess board-like assembly (or "unlike-spin pairings" HS-LS) of the two spin species during the spin transition, similar to the spin (or magnetic domain) arrangements in antiferromagnetic materials, while cooperative interactions refers to those interactions that tend to promote "like-spin" pairings (HS-HS or LS-LS) during the spin transition, similar to the spin (or magnetic domain) arrangements in ferromagnetic materials. The presence of strong cooperative interaction is marked by an abrupt, as well as the presence of hysteresis in the temperature-induced spin transition.

Different models have been proposed over the years to explain cooperative SCO, such as: Ising-based model where the two spin states are described with pseudo-spin operators and interact *via* nearest neighbour elastic coupling [41]; long-ranged elastic interactions arising from the change in volume and shape of molecule accompanying the spin crossover [42]; vibronic model that takes into account quantum mixing between the two spin states that might result from higher order spin-orbit coupling [43]. There are also theories which propose that the contributions to cooperativity from magnetic interactions between the transition metal centres could be as significant as that from elastic interactions [44, 45]. There are, yet, reports of cooperativity to be electrostatic in origin [46, 47]. A macroscopic

thermodynamic model, based on the mean-field approach proposed by Slichter and Drickamer (S-D) [48], is one of the most widely used model to describe cooperative effects. In the S-D model, an additional free energy term $G_{int} = \Gamma\dot{\gamma}_{HS}(1-\gamma_{HS})$ — where Γ is a phenomenological interaction parameter — is introduced into Equation 1.2; albeit the origin of Γ is not defined. At equilibrium, this leads to an implicit equation of the form:

$$\ln\left(\frac{1-\gamma_{HS}}{\gamma_{HS}}\right) = \frac{\Delta H + \Gamma(1-2\gamma_{HS})}{RT} - \frac{\Delta S}{R} \tag{1.6}$$

where R is the universal gas constant. The experimental input in Equation 1.6 is γ_{HS}. Γ is negative for anticooperative interactions while positive for cooperative interactions. This equation will be used to explore cooperative effects in [Fe(H_2B(pz)$_2$)bipy] molecules deposited on a highly oriented pyrolytic graphite (HOPG) surface with coverages ranging from submonolayers to multilayers, presented in Chapter 4.

The origin of both ΔH and ΔS can be traced to the electronic and vibrational change accompanying the spin-state transition. In most cases, the amount of electronic and vibrational contributions to the two thermodynamic parameters may differ; for ΔH, the electronic contribution (ΔH_{el}) is dominant, while in the case of ΔS, vibrational contribution (ΔS_{vib}) is larger over the electronic contribution (ΔS_{el}):

$$\Delta S = \Delta S_{vib} + \Delta S_{el} = \Delta S_{vib} + R\ln(g_{HS}/g_{LS}) \tag{1.7}$$

where $g_{LS,HS} = (2S_{LS,HS}+1)$ denotes the electronic degeneracies of the spin states, respectively. As an example, for a powder-crystal of [Fe(H_2B(pz)$_2$)bipy], ΔS_{vib} is estimated as $35.9\,\mathrm{J\,K^{-1}\,mol^{-1}}$, using Raman Spectroscopy [49]. The electronic contribution to the total entropy change ΔS for an Fe(II)-based spin-crossover molecule — using Equation 1.7 — is $\sim 13.4\,\mathrm{J\,K^{-1}\,mol^{-1}}$.

1.1.3 Light-induced excited spin-state trapping

At low temperatures (below 40 K), it is possible to switch SCMs from the LS ground state to the metastable HS state of long lifetime by irradiating it with light. This phenomenon is termed as light-induced excited spin-state trapping (LIESST), and has been discovered by Decurtins *et al.* [50] in 1984 while irradiating crystals of [Fe(ptz)$_6$](BF$_4$)$_2$ (ptz = 1-propyltetrazole) at 514 nm. Two years later, reverse-LIESST process — re-population to the LS ground state from the metastable HS state — was discovered by Hauser *et al.* by irradiation at 820 nm, proving the reversibility of the spin switching processes [51]. The quantum efficiency of LIESST at low temperature (10 K) is shown to be of the order of unity [52].

The mechanism of LIESST process is understood in terms of the potential energy landscape (PES) drawn in a configurational coordinate diagram of the totally symmetric metal-ligand stretch vibration, as shown in Fig. 1.4. The LS and HS potential wells are separated along the x-axis by a distance proportional to the Fe-N

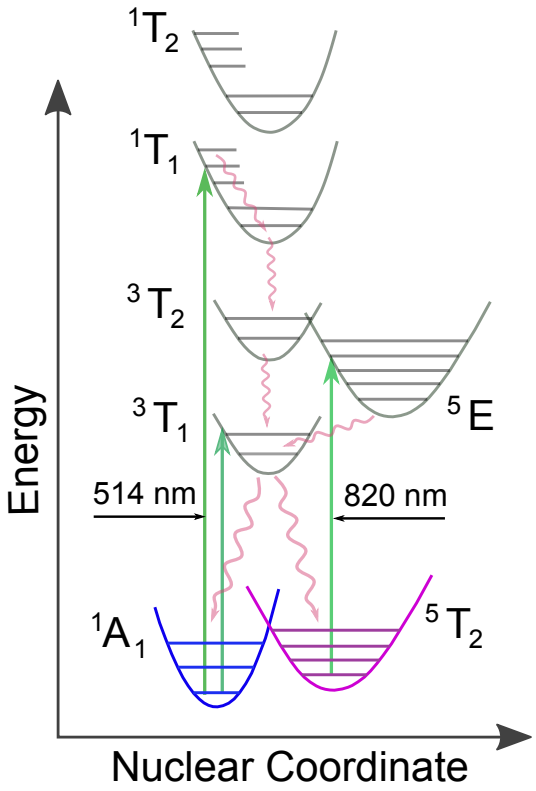

Figure 1.4: Schematic representation of LIESST and reverse-LIESST process in SCMs along the totally symmetric metal-ligand stretch vibrations. $^1A_1$ and $^5T_2$ are the LS and HS states, respectively; $^1T_{1,2}$ are the metal-to-ligand charge transfer states, and $^3T_{1,2}$ represent the intersystem crossings

bond-length difference between the two states; the difference of the zero-point energy of the two wells (along the y-axis) — which in a first order approximation, is equal to the enthalpy difference between the two states — is of the order of the thermally accessible energies, k_BT [33]. The LIESST process can be described as, thus: electrons at the LS state are excited to the metal-to-ligand charge transfer singlet state (MLCT, $^1T_1$) following the Frank-Condon principle, with light of wavelength 514 nm, which then undergo ultrafast relaxation to the quintet HS state $^5T_2$ *via* the intersystem crossing (ISC). The ISC should necessarily involve triplet states $^3T_{1,2}$, as direct transitions from LS (S = 0) to HS (S = 2) are forbidden.

1.1.4 High spin to low spin decay

The photo-induced HS state — owing to its metastable character — decays into the ground LS state, depicted by the PES diagram of Fig. 1.4. The relaxation process can be divided into two regimes — the low temperature regime ($\leq$40 K), where the process occurs *via* quantum tunnelling and is independent of temperature; and the thermally activated regime, where the relaxation is determined by cooperative effects and deviates strongly from the simple Arrhenius law. The theoretical ex-

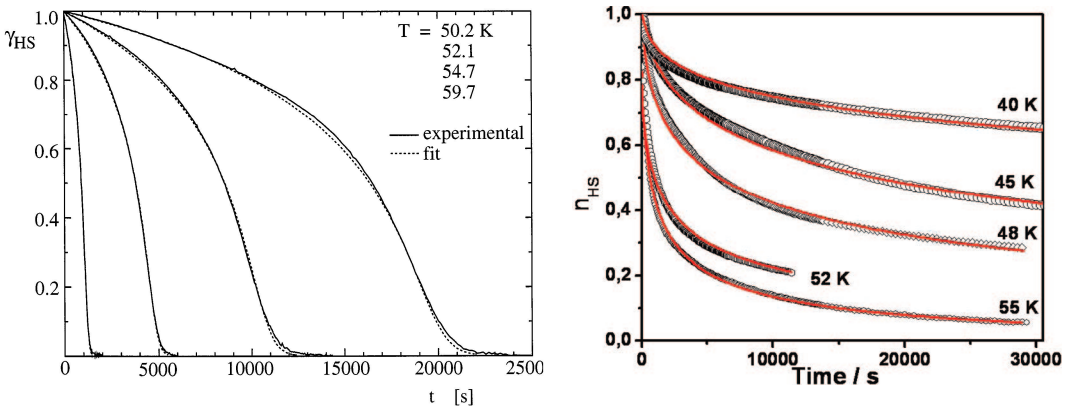

Figure 1.5: HS→LS relaxation in the solid state at the thermally activated regime. Left panel: Sigmoidal-type relaxation behaviour of SCMs exhibiting cooperativity. Reproduced from ref. 54, with permission from Elsevier; Right panel: Stretched-exponential decay exhibited by disordered systems. Figure reproduced with permission from ref. 55. Copyright © 2008, American Chemical Society

planation of the relaxation process at the low temperature regime was given by Buhks *et al.* [53] in the framework of non-adiabatic multiphonon processes in the strong coupling limit. In the low temperature regime, the metastable HS state is characterized by a rather long lifetime, with the rate constant given by [54]:

$$k_{HL}(T \to 0) = \frac{2\pi}{\hbar^2 \omega} \beta^2 F_n(T \to 0) \tag{1.8}$$

where $\hbar\omega$ is the vibrational frequency of the metal-ligand breathing mode with typical values of $\sim$250 cm^{-1} and a corresponding force constant f of $2\times$ 10^5 dyne cm^{-1}; β_{HL} is the electronic coupling matrix element of the second order spin-obit coupling with value of $\sim$150 cm^{-1} [54]; $F_n(T \to 0)$ is the thermally averaged Frank-Condon factor — accounts for the thermal population of all the vibrational levels of the HS state at T→0 — and has the form:

$$F_n(T \to 0) = \frac{e^S S^n}{n!} \tag{1.9}$$

where the Huang-Rhys factor $S = \frac{1}{2}\frac{f\Delta Q_{HL}^2}{\hbar\omega}$ estimated to be $\sim$45; ΔQ_{HL} is a measure of the change in the bond-length during the HS to LS transition estimated to be $\approx$ 0.5 Å; n is the reduced energy given by $n = \Delta E_{HL}^0/\hbar\omega$, where ΔE_{HL}^0 is the vertical displacement between the LS and HS wells. The experimental values of $k_{HL}(T \to 0)$ range from 10^{-6} s^{-1} to 10^6 s^{-1} [54].

In the thermally activated regime — generally $\geq$ 40 K — the nature of the HS→LS relaxation is determined by cooperative effects, and the disorder in the structure; for SCMs exhibiting strong cooperativity, the relaxation curve is sig-

moidal type, while for disordered (amorphous) systems, the relaxation curve exhibits a stretched exponential behaviour (an initial fast decay, and then slowed down considerably with time), shown in Fig. 1.5. The sigmoidal behaviour is explained by Hauser by introducing an acceleration factor α in the decay equation [54]. The acceleration of the decay process is proportional to the LS contents, indicating its origin as due to cooperativity between the spin-transiting centres:

$$\frac{\partial \gamma_{HS}}{\partial t} = -k_{HL}\, \gamma_{HS} \exp[\alpha(1-\gamma_{HS})] \tag{1.10}$$

where k_{HL} is the decay constant; γ_{HS} denotes the HS fraction. The Hauser acceleration factor α can be related to the interaction parameter Γ of the S–D model by a constant p, as $\alpha = p\,\Gamma$ [54]. The value of p is governed by the value of the reduced energy n: for $n \leq 1$, $p = 2\ln(S)/\hbar\omega$, while for larger values of n, $p = 2\ln(S/n)/\hbar\omega$.

On the other hand, the stretched exponential decay observed in disordered systems is attributed to the distribution in the activation energies from site to site [54]; the relaxation curve can be fitted by introducing a gaussian distribution of activation energy into the decay equation. It should also be noted that in diluted systems (doped-SCMs) free from cooperative effects, the HS→LS decay is characterized by a mono-exponential function. The question is: How would the HS→LS relaxation curve of SCMs exhibiting anticooperativity look like? Following Equation 1.10, the decay parameter α will assume negative values, and the form of the decay curve will be a stretched exponential, similar to disordered systems. This line of reasoning will be used in explaining the relaxation behaviour of submonolayers of the complex [Fe(H_2B(pz)$_2$)bipy] deposited on an HOPG surface, presented in Chapter 4 Section 4.4.

1.2 Spin-crossover molecules on surfaces: state-of-the-art

A basic or fundamental understanding in the nature of spin transition / switching for SCMs in contact with solid surfaces is a prerequisite when it comes to exploiting SCMs for applications in single-molecule-based devices. The advent of investigations of SCMs deposited on surfaces, or in thin films, is relatively recent. This can be mainly attributed to two main factors: (i) the fragility of the spin-crossover molecules, *i.e.*, upon contact with a surface results either in a complete or partial loss of the spin switch-ability, or the molecules tend to undergo fragmentation (which will be outlined in the following paragraphs); and (ii) the poor processability in thin films. Nevertheless, great efforts have been made recently in the growth of thin films and nanostructures, which revived interest in the field [56].

Techniques used for the growth of thin films of SCMs include Langmuir-Blodgett techniques [57],[3] spin-coating method [58], drop-casting method [59],

[3]This is the first ever report of thin films of SCMs

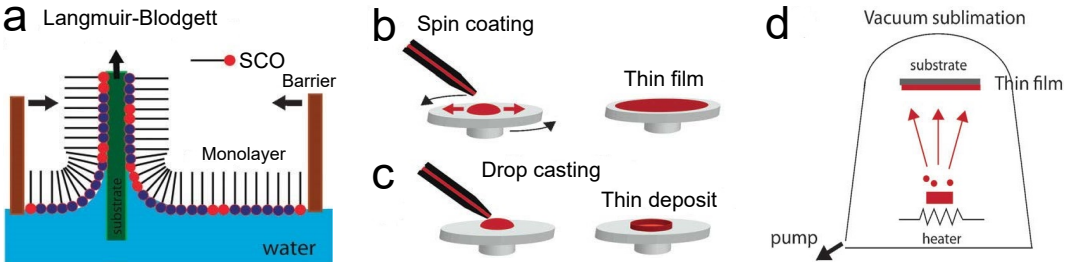

Figure 1.6: Sketch of the main methods used in the growth of spin-crossover molecular thin films. (a) Langmuir-Blodgett, (b)spin coating, (c) drop casting, and (d) vacuum evaporation/sublimation. Figure adapted from ref. 56 with permission

nano-patterning using lithography techniques [60], and vacuum sublimation [61–63], shown in Fig. 1.6. Of the aforementioned thin film growth techniques, vacuum sublimation offers certain advantages over the other techniques, namely, that the technique produces high quality thin films, where both the thickness and the morphology can be controlled precisely; this makes it easily integrable with the existing thin film fabrication techniques used in the electronics industry. However, it is hampered by the scarcity of SCMs stable against sublimation. In fact, vacuum evaporable/sublimable SCMs reported so far numbered less than 20 [31, 64, 65].

X-ray absorption spectroscopy (XAS) and scanning tunneling microscopy (STM) are the two widely used techniques in investigating SCMs in direct contact with a solid surface (submonolayer or monolayer coverage). The techniques, though powerful in revealing the surface spin states, come with certain limitations; STM can provide information only on the local properties, and they have never been used in the systematic investigation of the thermodynamic parameters involved in the spin-crossover phenomena, while x rays and the x-ray generated secondary electrons — mainly from the surface on which the molecules are deposited — of the XAS technique can bring about undesirable effects such as in causing ligand modification, or inducing a spin-state change while recording the data [31, 66, 67].

With regard to the utility of STM in identifying the molecular spin states, one can infer it directly from the size-dependent topography and electrical conductivity difference between the two spin states — SCMs in the LS state(s) are smaller in size, and exhibit lower conductivity as compared to those in the HS state(s), apart from the presence or absence of Kondo resonance in the HS or LS states, respectively [68]. Due to certain technical challenges, there is a limitation on the surface (substrate) on which STM-based studies can be carried out. STM-based studies are done almost invariably on gold surface. As for the XAS technique, the spin-state identification is also straight-forward: the spectral profile of the $L_{2,3}$ edge (or just the L_3 edge) of the central Fe(II)-ion is distinctly dissimilar for the HS and LS molecules, and can be used as a fingerprint of the spin states [64, 69]. In the following is given

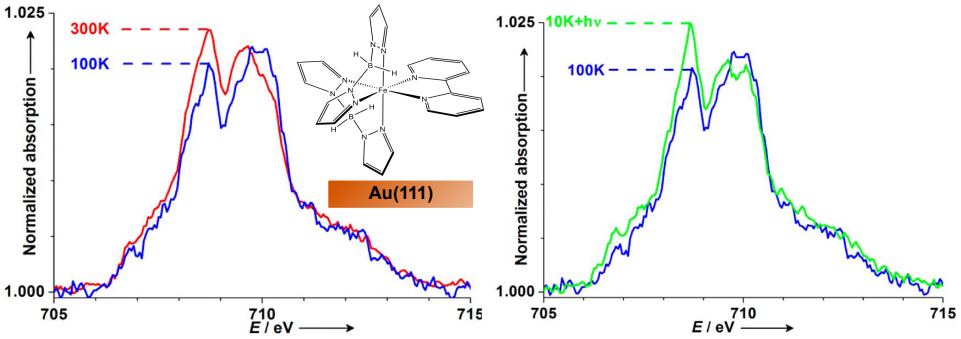

Figure 1.7: [Fe(H_2B(pz)$_2$)bipy] at Au(111) surface, investigated by x-ray absorption spectroscopy. Left panel: Fe L_3 XA spectra recorded at 300 K (red) and at 100 K; the spin-state switching is readily inferred from the change in the absorption intensity corresponding to the HS state at ∼708.7 eV or the LS state at ∼709.8 eV. Right panel: Spectral profile comparison between that recorded at 100 K and after illumination with green light at 10 K. The HS (or LS) fraction is estimated by fitting th spectra to that of a linear combination of reference HS and LS spectra of the molecular powder sample [70]. Figure adapted from ref. 70 with permission. Copyright © 2013, American Chemical Society

a brief literary overview of SCMs investigated on surfaces, which is by no means exhaustive and not necessarily in chronological order.

There are three widely investigated SCMs on surfaces, prepared by vacuum sublimations: the two closely-related molecules [Fe(H_2B(pz)$_2$)bipy] and [Fe(H_2B(pz)$_2$)phen], and [Fe(phen)$_2$(NCS)$_2$]. One of the earliest XAS-based investigation of SCM-surface systems is that of [Fe(H_2B(pz)$_2$)bipy] deposited on Au(111) surface by Warner *et al.* [70]. The authors reported both temperature and light-induced switching in about 20% of the molecules in contact with the surface, of coverage estimated to be between 0.03 to 0.14 ML. The amount of molecules undergoing the spin-state change is inferred from the change in the absorption intensity for the peaks corresponding to the HS and LS states in the Fe L_3 spectra, shown in Fig. 1.7. However, it has been pointed out by Kuch and Bernien [71] that Warner *et al.* might have probably erred in their estimation of the molecular coverage; the reported value of between 0.03 — 0.14 ML could in fact, be more than a monolayer. The molecules undergoing spin switching are the ones not in contact with the surface.

This is in light of the results of the investigations of the closely-related molecule [Fe(H_2B(pz)$_2$)phen] of submonolayer and higher coverages on Au(111) surface. By using combined XAS and STM studies, Gopakumar *et al.* [72] proved conclusively that those molecules in direct contact with the gold surface are decomposed into the HS [Fe(H_2B(pz)$_2$)] molecule and the phen ligand; the molecular integrity — and hence the spin crossover — is preserved only for those molecules decoupled

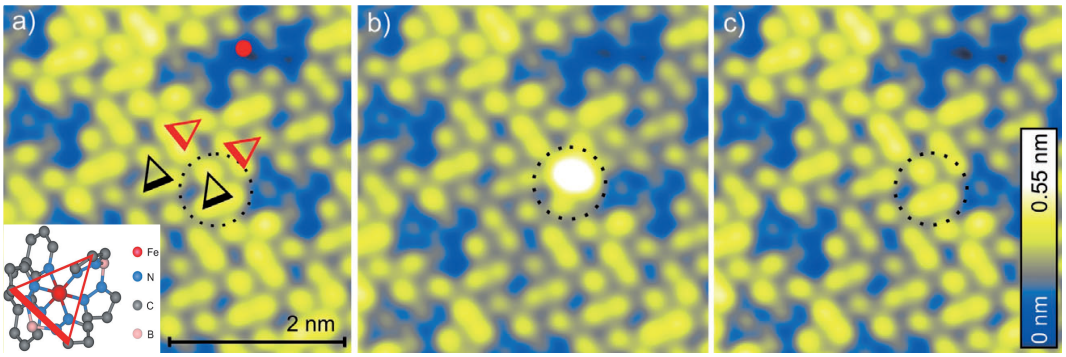

Figure 1.8: Electron-induced spin-state switching in a double-layer of [Fe(H_2B(pz)$_2$)phen] on Au(111), as seen from STM topographs. Dotted circles indicate a molecule at LS (a), switched to HS (b) and back to LS (c). Red dot in (a) indicates the STM-tip position; triangle in (a) connect the three pyrazole loops of the molecule, as shown in the inset. Figure adapted from ref. 68 with permission. Copyright © 2012, John Wiley and Sons

from the surface, *i.e.*, at the bilayer or higher.

In fact, the first report on the STM-based electron-induced spin switching — termed as electron-induced spin-state trapping (ELIESST), analogous to LIESST — was reported by Gopakumar *et al.* for [Fe(H_2B(pz)$_2$)phen] molecules lying at the second layer of Au(111) surface: the LS to HS transition is obtained by applying a sample voltage in the range of 2.5 - 3.0 V with the STM tip positioned at a nanometre above the molecules, and a HS to LS transition is observed when the sample voltage is maintained in the range of 1.6 - 1.8 V and the current strongly increased [68]. Molecules in the HS state are marked by an increase in their apparent height relative to the LS molecules, consistent with the higher volume expected of HS molecules [49, 73]. Molecules in the LS state — while switching from the HS state — are marked by a sudden drop in the tunnelling current; this is attributed to the relative lower conductivity of LS molecules, consistent with theoretical calculations/predictions [29]. This is shown in Fig. 1.8.

In an STM-based investigation of a bilayer of [Fe(H_2B(pz)$_2$)bipy] deposited on Au(111), Pronschinske *et al.* reported the coexistence of both the spin states at room temperature, with no apparent change in the spin-state compositions on cooling the sample to 131 K [74]. This is a clear departure from the bulk behaviour where the molecule exist in the HS state at room temperature and switched to the LS state on lowering the temperature, with a transition temperature of about 161 K [49, 73]. The authors attributed the spin-state coexistence down to the substrate-induced packing / molecular assembly on the surface. Beniwal *et al.* [75] investigated the same system — a bilayer of [Fe(H_2B(pz)$_2$)bipy] on Au(111) — and reported the same spin-state coexistence at all temperatures, albeit they reported spin transition in 12 ± 6% of the molecules; using a combination of XPS (x-ray absorption spectroscopy) and XAS, the authors quantified the spin-state compositions as

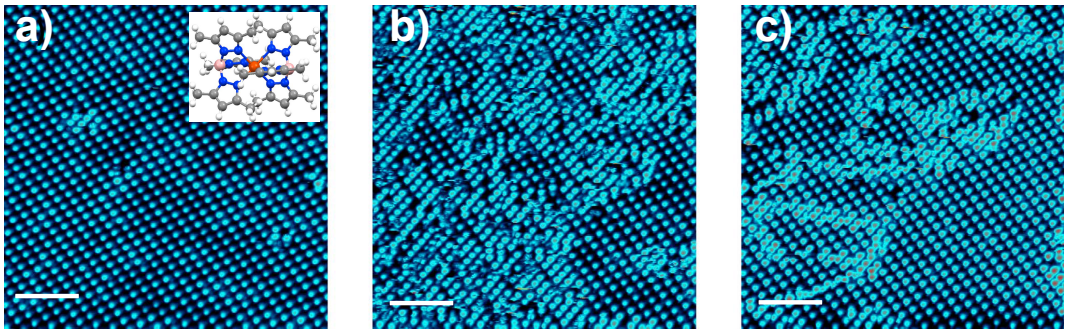

Figure 1.9: STM topography of light-induced spin switching at 4.6 K. (a) STM image (V = 0.3 V, I = 20 pA, scale bars, 10 nm) showing the co-existing HS and LS state superstructures of the pristine sample — a monolayer of $[Fe^{II}((3,5\text{-}(CH_3)_2Pz)_3BH)_2]$ on Au(111) — recorded at 4.6 K; (a) After 9 h and 45 min of blue-light illuminations; (c) The relaxed state recorded after 9 h and 45 min of stopping blue-light illumination. Bright and larger-sized dots represent HS molecules. The inset of (a) is the molecular structure. Figure adapted from ref. 76

$71 \pm 6\%$ HS at room temperature, and $59 \pm 6\%$ at low temperature (80 K). The similar amount of molecules undergoing spin switching as reported by Beniwal *et al.* [75] and by Warner *et al.* [70] for a bilayer and a 'submonolayer' of the same system, respectively, would support the arguments given in ref. 71 that the molecular coverage of ref. [70] is in fact, more than a monolayer.

Bairagi *et al.* [76] reported light-induced spin switching in a monolayer of an SCM $[Fe^{II}((3,5\text{-}(CH_3)_2Pz)_3BH)_2]$ deposited on a Au(111) surface at 4.6 K, probed with STM. The molecules retained their integrity on the surface, albeit a small amount of HS molecules is present at 4.6 K. Under blue-light illumination, the molecules appear brighter and larger — an indication of LS to HS state switching. The STM image showing the light-induced LS→HS state switching after 9 h and 45 min of illumination, and the spin relaxation after 9 h and 45 min of stopping the illumination is shown in Fig. 1.9. Interestingly, the authors also reported a collective behaviour in the spin-state switching, with a long-range order of alternately arranged HS and LS states, akin to the cooperative effects observed in the bulk materials [77]. The alternate arrangements in the two spin states would necessarily imply an anticooperative interactions, leading to a smooth/gradual spin transition.

The authors followed it up with an XAS investigation, wherein the spin-state compositions of a monolayer on Au(111) was estimated as 100% HS at room temperature, and $32 \pm 6\%$ HS at 80 K [78]. The authors claimed the presence of hysteresis in the temperature-induced spin-crossover curve, implying the presence of cooperative interactions. However, the presence of about $32 \pm 6\%$ HS molecules at all temperatures is expected to promote anticooperative interaction, leading to a gradual spin transition, as is observed [78].

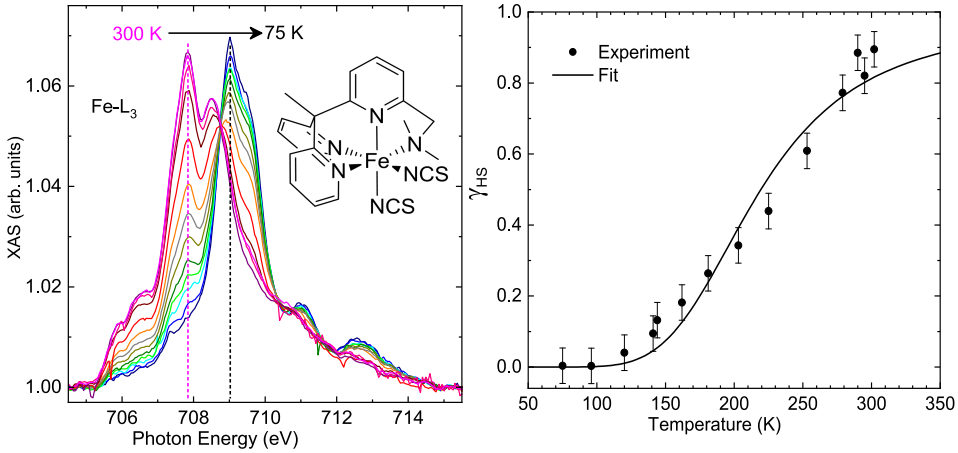

Figure 1.10: Clean spin-state switching on a highly-oriented graphite surface. Left panel: Fe L_3 spectra of 0.8 ML of $[Fe(NCS)_2L]$ on HOPG, with the room-temperature spectral peaks at 707.8 and 708.1 eV representing the HS state and gradually transforming to the low-temperature spectral peak at 709.0 eV representing the complete conversion to the LS state. Right panel: Plot of the γ_{HS} (HS fraction) variation with temperature (dots) and the model fit (solid line). γ_{HS} is obtained by using the spectra at 300 K and that at 75 K as the reference HS and LS spectra; a linear combination of the two would yield any other intermediate spectrum. Figure adapted from ref. 64 with permission. Copyright © 2012, American Chemical Society

The first report of "clean" spin-state switching as well as the earliest report of SCMs in direct contact with a solid surface is of 0.8 ML $[Fe(NCS)_2L]$; L = 1-(6-[1,1-di(pyridin-2-yl)ethyl]-pyridin-2-yl)-N,N-dimethylmethanamine] deposited on a highly oriented graphite surface (HOPG) by Bernien *et al.* [64], using the XAS technique. The molecular coverage of less than a monolayer is found to undergo a gradual spin-state transition from the HS state at room temperature to the LS state at low temperature (75 K), shown in Fig. 1.10; the spin transition was treated quite satisfactorily as a non-interacting system given by Equation 1.5. The spin-crossover was further confirmed with the branching ratio — defined as the ratio between the integrated Fe-L_3 intensity to the $L_{2,3}$ intensity — which was found to vary from 0.74(2) at 300 K to 0.64(2) at 75 K. The reduction is due to a decrease in the 3d spin-orbit coupling energy due to the vanishing magnetic moment in the LS state, and can be used as a measure of spin transition [79, 80]. Bernien *et al.* also reported the clean spin-state switching induced by both temperature and light, for a 0.4 ML of $[Fe(H_2B(pz)_2)phen]$ deposited on an HOPG surface; the light-induced LS→HS state transition at 5 K is found to be highly efficient [31], which is promising for their potential applications as optical memory and display elements [81]. $[Fe(H_2B(pz)_2)bipy]$ on the same substrate is also investigated — in the context of this thesis, given in Chapter 4 — wherein the evolution of cooperative effects is systematically explored in coverages ranging from submonolayers to multilayers.

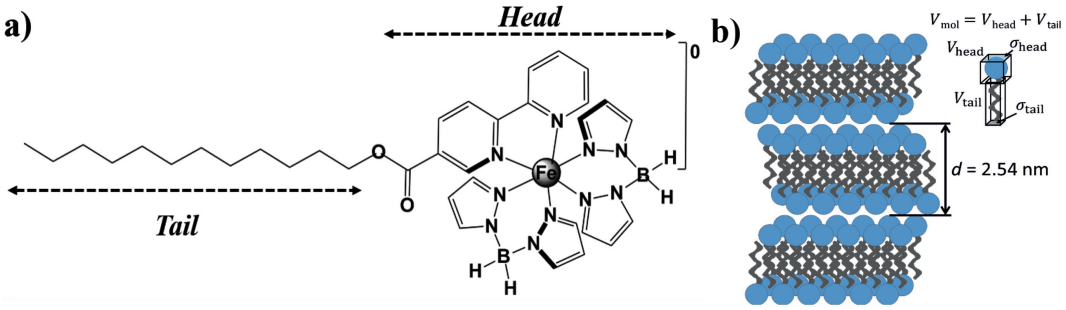

Figure 1.11: Self-assembled monolayers due to addition of carbon chains. (a) [Fe($H_2B(pz)_2$)bipy] functionalized with $C_{12}H_{25}$ "tail"; (b) Scheme of the molecular arrangements of ultrathin films — interlayer interlocking provided by the "tails" supposedly aided in the formation of self-assembled monolayers. Figure taken from ref. 85 with permission. Copyright © 2018, John Wiley and Sons

The other widely investigated SCM on a surface is [Fe$(phen)_2(NCS)_2$] [82]; it has been investigated on surfaces such as Cu(100), Cu_2N/Cu(100), Cu(111), Co/Cu(111), Co(100), Au(100), and Au(111) [82]. Unlike [Fe($H_2B(pz)_2$)bipy] and [Fe($H_2B(pz)_2$)phen], [Fe$(phen)_2(NCS)_2$] is found to stay intact on an Au surface, besides the other surfaces listed above. Nevertheless, the molecule is reported to be coexisting in both the spin states at 4.2 K in both Cu and Au surfaces, coupled with the loss of SCO property [82]. Gruber *et al.* attributed the spin-state coexistence as due to the specific adsorption sites on the substrate: some sites favouring the HS state, and yet other sites favouring the LS state [82, 83]. Gueddida *et al.* [84] found this indeed to be the case: by an *ab initio* calculation, the adsorption energy — the energy required to detached the molecule from the surface — of the HS and LS states are calculated as - 2.22 and - 2.62 eV, respectively. The adsorption energy difference between the two spin states — ∼0.4 eV — is much higher than the 0.17 eV energy difference of the two spin states for a free molecule, leading to the spin-state locking.

A promising route towards depositing self-assembled SCMs in ultra-thin films is reported by Kumar *et al.* [85], where the SCM [Fe($H_2B(pz)_2$)bipy] is functionalized with a long carbon chain $C_{12}H_{25}$ at the bipyridine ligand, forming [Fe$(H_2B(pz)_2)_2(C_{12}$-bipy)] (C_{12}-bipy = dodecyl [2,2-bipyridine]-5-carboxylate), shown in Fig. 1.11; the overall structure resembles a classical amphibilic molecule — the pseudohydrophilic head comprising the Fe-atom, and the hydrophobic tail comprising the carbon chain ($C_{12}H_{25}$) — the self-assembly occurring via intermolecular hydrophobic interactions. The amphiphile-like molecular organization of the molecule into double layers separated by tails is further established by an x-ray diffraction measurements.[4]

[4]The works on tuning the spin-crossover behaviour of surface-deposited SCMs are initiated in the framework of this thesis, in collaboration with Naggert and Ossinger of CAU-Kiel. The results are presented in Chapter 5

From the transition width ΔT of the thermal-induced spin transition curve — defined as the temperature difference at which 80% of the molecules are in the HS and LS states, respectively — one can make a comparison between the cooperativity in the spin transition processes between different SCMs; the lower is ΔT, the higher is the cooperativity. From the data provided by Kumar *et al.* [85] for a 10-nm thin film of [Fe(H_2B(pz)$_2$)$_2$(C_{12}-bipy)] deposited on SiO_x substrate and investigated by XAS, ΔT is estimated as ≈ 71 K. This is higher than $\Delta T = 50(4)$ K reported for a similarly thick film (about 10 monolayers) of the parent molecule [Fe(H_2B(pz)$_2$)bipy] prepared on an HOPG surface [65], indicating that the addition of carbon chains to the ligands doesn't promote cooperativity in ultra-thin films.

The role of the molecule-substrate interaction in preserving the SCO property is also shown vividly by Miyamachi *et al.* [86], wherein by introducing a thin insulating spacer layer of Cu_2N between [Fe(phen)$_2$(NCS)$_2$] and a Cu(100) substrate, the previously 'trapped' spins can be switched with an electric field *via* an STM tip. Similar behaviour was reported by Jasper-Toennies *et al.* [87] in an Fe(III)-based SCM deposited on the same substrate system. Rohlf *et al.* [88] reported that an Fe(II)-based low-spin complex — showing no SCO behaviour in the solid state — exhibit both light- and soft x-ray-induced excited spin-state trapping at low temperatures (28 K) in the thin film. This is interesting in view of the avenue it offers for engineering SCO in reduced dimensions.

From the foregoing discussion, it is clear that despite the challenges associated with SCM-surface systems at the very basic level, such as in retaining the integrity of the molecule or the SCO phenomenon, one can overcome these problems by a suitable choice of molecules and substrate combinations. However, the reports of such suitable systems are lacking so far.

"He wished he had some kind of x-ray vision for the human heart."
— Kim Edwards, The Memory Keeper's Daughter

2

METHODS AND TECHNICAL ASPECTS

The discovery of x rays in 1895 by Wilhelm Conrad Röntgen would certainly rank as one of the most significant scientific discoveries of all times. Besides their use in x-ray imaging for medical applications — which is well known — x rays are used as search light to peer through and unravel the intrinsic properties of materials. The mode of production of x rays (and the x-ray-based characterization techniques) have undergone huge sophistications: from first generation synchrotrons of the 1950s that were designed for the study of high-energy particle physics, with synchrotron radiation as a by-product, to the soon-to-be-operational highly tunable and powerful x-ray sources, namely, x-ray free-electron lasers, produced in synchrotron radiation facilities.

The technique employed in this thesis is called near-edge x-ray absorption fine structure (NEXAFS) spectroscopy, also sometimes called as x-ray absorption near-edge spectroscopy (XANES), or simply x-ray absorption spectroscopy (XAS) that operates in the soft x-ray regime (100—5000 eV). The aim of this chapter is to provide a fair description of the methods used in conducting the experimental work in the context of this thesis, both technical and theoretical — x-ray absorption spectroscopy (XAS), sample preparation, right down to estimating the molecular coverage on a surface.

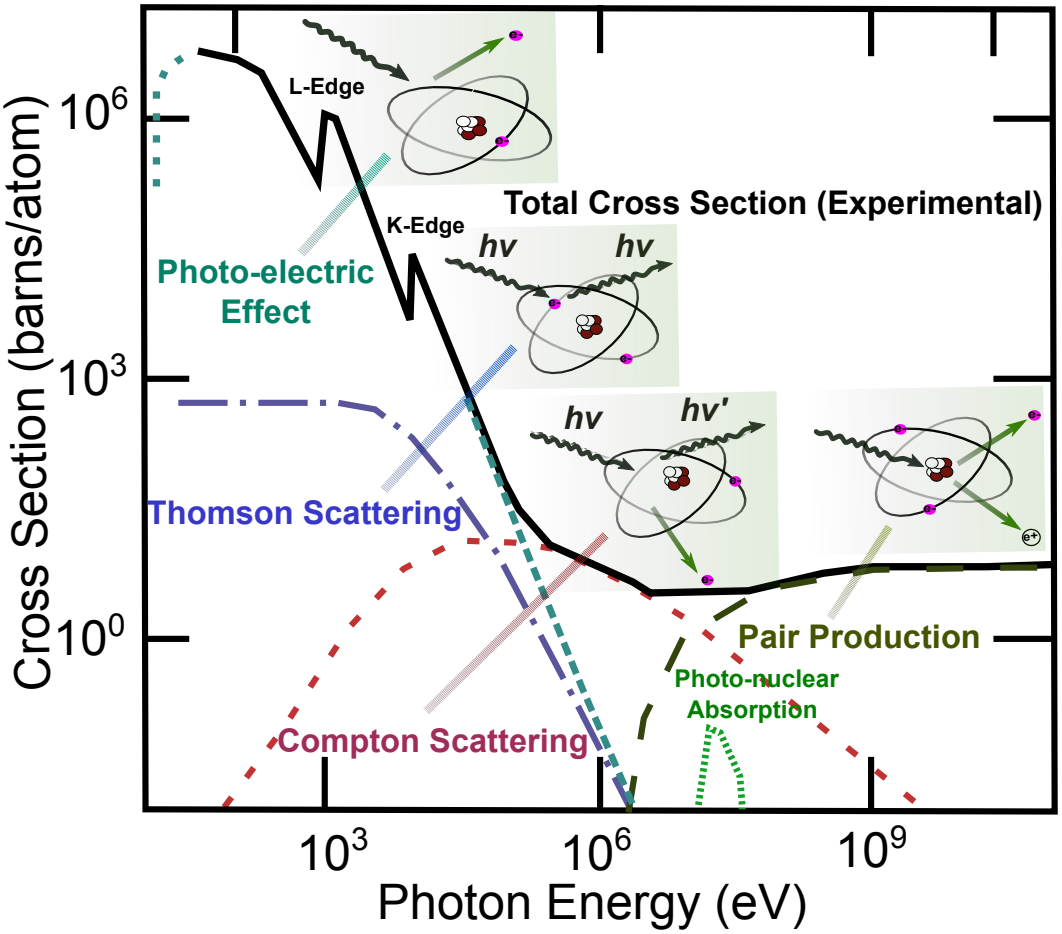

Figure 2.1: Graphical representation of the various interaction mechanisms of x rays with matter in terms of the energy-dependent absorption cross-section, in the case of a Cu-metal sample as an example. Figure adapted from ref. 89

2.1 X-ray—matter interaction

The different mechanisms by which x rays interact with matter is shown graphically in Fig. 2.1 in terms of the energy-dependent absorption cross-section, taking a Cu-metal sample as an example. The energy range of interest in the framework of this thesis is the so-called soft x-ray regime. In this regime, x ray and matter has three modes of interactions — photoabsorption (photo-electric effect), Thomson and Compton scatterings, which are elasic and inelastic scatterings, respectively — albeit photoabsorption is the dominant mechanism. The photo-absorption cross-section (hereafter referred to as absorption cross-section) is characterized by distinctive peaks (or edges) corresponding to the excitation of core-electrons at $1s$, $2s$, $2p_{1/2}$, $2p_{3/2}$, $3s$, ... which are labeled respectively as K, L_1, L_2, L_3, M_1, ...

The photoabsorption mechanism can be understood in terms of a one-electron model; the x-ray photon of energy $E = \hbar\omega$ induces excitation of electron of $|i\rangle$ state

of energy E_i into a continuum of final states $|f\rangle$ with density $\rho(E_f)$ and energy $E_f = E_i + E$. The absorption cross-section is defined as the ratio of the number of electrons excited per unit time (transition probability) to the photon flux, as:

$$\sigma(\hbar\omega) = \frac{w_{i\to f}}{I_{ph}} \tag{2.1}$$

Using *Fermi's golden rule*, the transition probability $w_{i\to f}$ can be expressed as:

$$w_{i\to f} = \frac{2\pi}{\hbar}|\langle f|\mathcal{H}_{int}|i\rangle|^2\rho(E_f)\delta(E_f - E_i - \hbar\omega) \tag{2.2}$$

where $\mathcal{H}_{int}$ denotes the interaction operator representing the time-dependent perturbation of the Hamiltonian of the atom. If $\mathbf{A}(\mathbf{r}, t)$ is the vector potential of the electromagnetic field of the photon, then $\mathcal{H}_{int}$ has the form:

$$\mathcal{H}_{int} = -\frac{e}{2mc}\mathbf{A}\cdot\frac{\hbar}{i}\nabla \tag{2.3}$$

In the soft x–ray regime, which is the energy range of interest of the x-ray characterization technique used in the context of thesis, namely, NEXAFS, the vector potential — expressed in terms of electromagnetic plane waves with the wave vector $\mathbf{k}$, frequency ω and polarization vector ϵ — can be expanded under the condition that $\mathbf{kr} \ll 1$, as:

$$\vec{A}(\vec{r}, t) = A_0\vec{\varepsilon}\mathrm{e}^{i(\vec{k}\cdot\vec{r}-\omega t)} = A_0\vec{\varepsilon}\mathrm{e}^{-i\omega t}\left\{1 - i\mathbf{kr} + \frac{1}{2}(i\mathbf{kr})^2 + \ldots\right\}. \tag{2.4}$$

The terms on the right hand side describe the electric dipole (E1), magnetic dipole (M1), electric quadrupole transitions (E2) ..., respectively. The latter have to be taken into account in the hard x-ray range as for example at the L edges of the rare earths [90]. In the dipole approximation (*i.e.*, the zeroth order of $\mathbf{A}$), the transition probability then reduces to:

$$w_{i\to f} = \frac{\pi e^2 A_0^2\omega}{2\hbar^2c^2}\,\hbar\omega\,|\langle f|\epsilon\mathbf{r}|i\rangle|^2\rho(E_f)\delta(E_f - E_i - \hbar\omega) \tag{2.5}$$

Finally, on plugging-in the above expression into Equation 2.1, the photoabsorption cross-section becomes —

$$\sigma(\hbar\omega) = \frac{4\pi e^2}{\hbar c}\,\hbar\omega\,|\langle f|\epsilon\mathbf{r}|i\rangle|^2\rho(E_f)\delta(E_f - E_i - \hbar\omega) \tag{2.6}$$

where the photon flux I_{ph} expressed as $I_{ph} = A_0^2\omega/(8\pi\hbar c)$ — the energy flux divided by the photon energy.

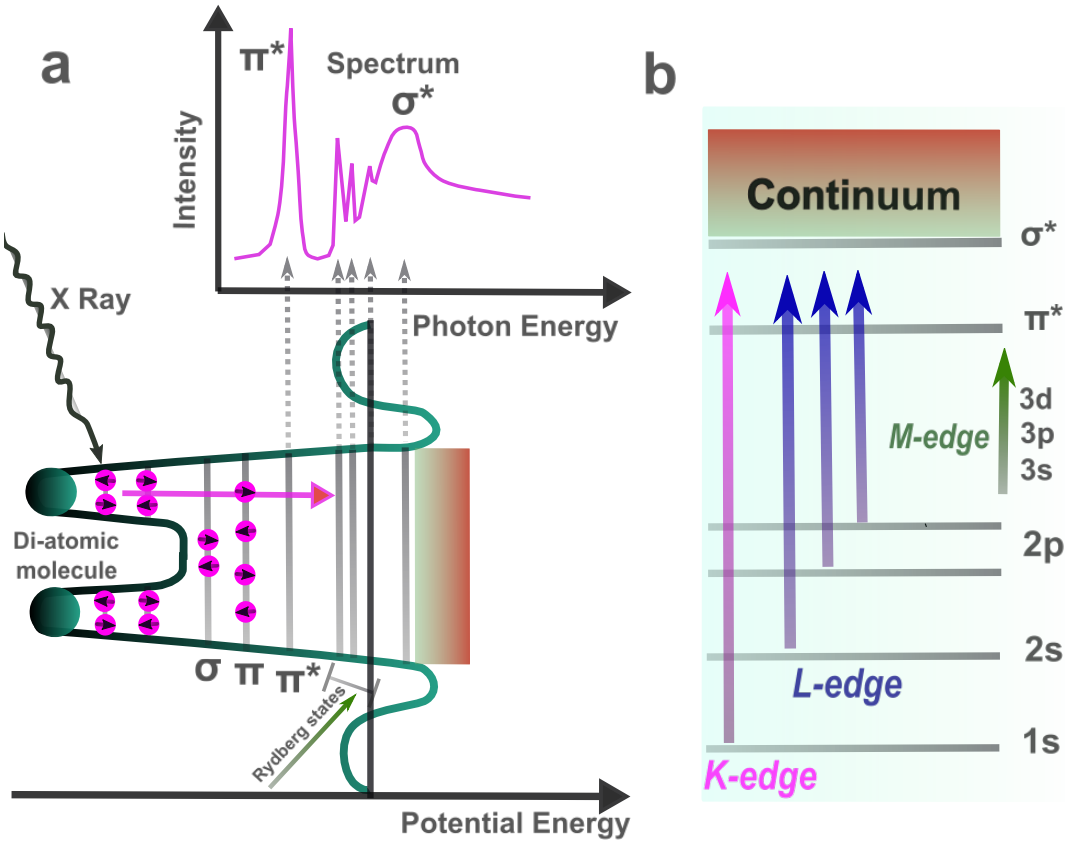

Figure 2.2: (a) Sketch of near-edge x-ray absorption fine structure spectrum of a hypothetical diatomic system; (b) Sketch of the K-edge, L-edge, and M-edge arising from orbitals with principle quantum numbers 1, 2 and 3, respectively

2.2 Near-edge x-ray absorption fine-structure spectroscopy

Near-edge x-ray absorption fine-structure (NEXAFS) spectroscopy is a powerful technique in unravelling the structural and the electronic properties of molecules adsorbed on surfaces. NEXAFS was developed in the 1980s with the main intention of determining the structural/orientation of "light" molecules — composed of low-Z elements such as carbon, nitrogen, oxygen and flourine — adsorbed on surfaces. Since then, it has been applied to a cross-section of "bulky molecules" in unravelling electronic and also the magnetic properties — in the case of magnetic molecules. Spin-crossover molecules are a case in point.

In NEXAFS technique, the core electrons are excited to the unoccupied states above the Fermi level and below the ionization threshold. The spectrum is obtained by varying the energy of the photons in an energy range of some electron volts close to an absorption edges such as the *K*, *L* or *M* — schematically depicted in Figure 2.2. The spectral profile is a fingerprint of the electronic distribution — the unoccupied density of states as a function of energy — which may originate from valence states in the case of solids or from atomic or molecular orbitals in the case of molecules.

The technique provides element-selective information about the chemical state and the surrounding environment. This, combined with the high sensitivity, makes it tp emerge as one of the widely used tool among researchers in investigating surfaces and adsorbates on substrates. The low penetration depth of x rays of about 20 nm at the Fe, Co, and Ni $L_{2,3}$ edges — in the energy range of $\sim$700 eV — together with the short escape depth of photoelectrons in bulk material of the corresponding elements, makes NEXAFS measurements highly surface sensitive.

The utility of the NEXAFS technique in probing the electronic properties and the molecular orientation on surfaces can be understood from an evaluation of matrix elements as given in Equation 2.6, which ultimately calls for an appropriate description of the initial and final states. Again, considering the one-electron model; the x ray absorption creates a core-hole which is bound strongly to the valence electrons due to electrostatic interactions. This leads to a strongly localized excitation that can be described satisfactorily within the framework of atomic physics. The initial and final states are then expressed in terms of atomic orbitals (AOs), as: $|i\rangle = \sum_{m_l,m_s} a_{i,m_l,m_s}|n,l,m_l,s,m_s\rangle$ and $|f\rangle = \sum_{m'_l,m'_s} b_{f,m'_l,m'_s}|n',l',m'_l,s,m'_s\rangle$. Expanding the matrix element (dipole operator) into spherical harmonics to describe left- and right circularly ($q=-1$ and ($q=1$), respectively) , and linearly ($q=0$) polarized radiation yields [91]:

$$\sigma(\hbar\omega) = \frac{4\pi^2e^2}{3\hbar c\varepsilon_0}\hbar\omega R\Big|\sum_{q,m_l,m'_l}\varepsilon_q a_{i,m_l,m_s}b^*_{f,m'_l,m_s}\langle l',m'_l|Y_{1,q}|l,m_l\rangle\Big|^2\rho(E_f)\delta(E_f-E_i-\hbar\omega), \tag{2.7}$$

where $R = |\langle n',l'|r|n,l\rangle|^2$ denotes the squared radial part. Since the dipole operator does not act on the spin summation over m_s, m'_s cancels due to orthonormality $\langle m_s|m'_s\rangle = \delta_{m_s,m'_s}$. The radial part determines the strength of the transition whereas the orientation dependence is contained in the angular part. It can be evaluated using Wigner 3-j symbols:

$$\langle l',m'_l|Y_{1,q}|l,m_l\rangle = (-1)^{-m'_l}\sqrt{\frac{(2l+1)(2l'+1)3}{4\pi}}\begin{pmatrix} l' & 1 & l \\ -m'_l & q & m_l\end{pmatrix}\begin{pmatrix} l' & 1 & l \\ 0 & 0 & 0\end{pmatrix}$$

from which the dipole transition selection rules are deduced as $\Delta s = 0$, $\Delta m_s = 0$, $\Delta l = \pm 1$, and $\Delta m_l = q$. The angle-dependent absorption can be calculated by rotating the final state successively around the z, y', and z'' axes by three Euler angles using Wigner's D-matrix $\mathcal{R}(\alpha,\beta,\gamma)|l,m_l\rangle = \sum_{m'_l} D^{(l)}_{m'_l,m_l}|l,m'_l\rangle$.

A more realistic and detailed description of the spectra can be done within the framework of the multiplet theory in which the initial state $|nl^{2(2l+1)}n'l'^N\rangle$ with N valence electrons and the final state $|nl^{2(2l+1)-1}n'l'^{N+1}\rangle$ are constructed from Slater determinants of atomic obitals. Programs such as XAS4CTM [92] based on Cowan's code [93] and multiX [94] have been developed to simulate the experimental XA spectra; the former has been applied to simulate the Fe $L_{2,3}$ spectra of a spin-crossover molecule at the two different spin states [31, 70].

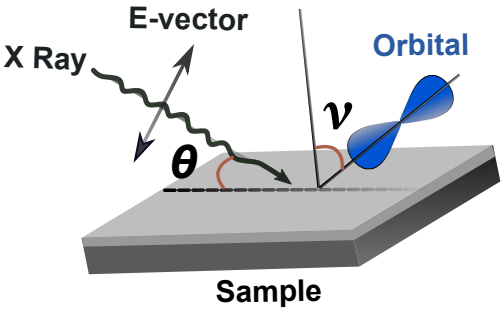

Figure 2.3: Unoccupied p orbital probed with linearly polarized X rays with an angle of θ between their $\vec{E}$ vector and the surface normal. ϑ is the tilting angle of the orbital given as the angle between its symmetry axis $\vec{o}$ and the surface normal

2.2.1 X-ray natural linear dichroism

To restate: In NEXAFS spectroscopy, resonances in the vicinity of the absorption edge are analysed. As we can see from equation 2.6, the intensity of a certain transition depends on the relative orientation of the transition matrix element and the polarization vector. This is referred to as X-ray natural linear dichroism and can be used in an angle-dependent measurement to determine the orientation of the atomic or molecular orbitals.

At the K edge, transitions from $1s$ to $2p$ are probed. The initial state is given by a single s orbital with isotropic charge distribution. Using linearly polarized X rays, the final state has zero angular momentum and the absorption cross section scales with $\cos^2$ of the angle between the symmetry axis $\vec{o}$ of the p orbital and the $\vec{E}$ vector of the X rays (Fig. 2.3). This can be used to determine the orientation of unoccupied π^* and σ^* molecular orbitals.

For adsorbed molecules, only their orientation relative to the surface is well defined, whereas they display a distribution of angles azimuthally. For substrates with higher than 2-fold symmetry or random azimuthal orientations of the molecules, we obtain the relative intensity as a function of the tilting angle ϑ of the unoccupied orbital and the angle θ between the $\vec{E}$ vector of the X rays and the surface normal [95]:

$$I(\theta) = \cos^2\theta\cos^2\vartheta + \frac{1}{2}\sin^2\theta\sin^2\vartheta.$$

We can now determine the tilt angle of a molecular orbital from the intensity ratio $r(\theta_1,\theta_2) = I(\theta_1)/I(\theta_2)$ of NEXAFS measurements at two different incidence angles and by solving this equation for ϑ. However, this procedure relies on the assumption that all molecules display the same tilting angle. With increasing disorder, the resonance intensity becomes independent of the incidence angle resulting in a ratio of $r(\theta_1,\theta_2) = 1$ and an apparent orientation of the orbital of $\vartheta = 54.7°$. A spectrum independent of the orientations of the molecules, commonly referred to as

the isotropic spectrum, can be obtained by measuring at $\theta = 54.7^{\circ}$, *i.e.* the magic angle.

At the $L_{2,3}$ edges, transitions from a $2p$ initial state to an unoccupied $3d$ orbital are excited. The angular dependence is usually not suitable to determine the orientation of an adsorbate, since the electronic transition is more complex than at the K edge. In the one-electron picture, 4 and 2 initial states are involved at the L_3 and L_2 edge, respectively. The final states are given by the five d orbitals in cubic symmetry, each with an anisotropic charge distribution. If the orientation of an adsorbed complex is known, for example from its K-edge angular dependence, the occupation of the individual $3d$ orbitals can be investigated as they display a different angle-dependent intensity. This can be explained as depicted in Fig. 2.3: with greater overlapping of the $\vec{E}$ vector of the x rays and the π^*–orbitals, the higher will be the XA intensity. In the depiction of Fig. 2.3, the maximum XA intensity will be obtained at the grazing angle between the x-ray beam and the surface of the sample.

2.3 Synchrotron radiation source

The present day high brilliance and highly focussed and controlled x rays are produced in what is called synchrotron radiation facilities. It is based on the fact that an accelerated charge, such as when moving on a curved path, generate electromagnetic waves. A synchrotron radiation facility typically consists of a booster, storage ring with the associated wigglers/undulators and bending magnets, beamlines, and end-stations where the actual experiments are performed — a sketch of the same is shown in Fig. 2.4. The booster is made of curved magnetic sections for focussing and bending the electron beams and straight-path sections for acceleration, which altogather form a closed circular path. The electron beams are synchronously accelerated and constrained to orbit the circular path until it attains a speed close to the speed of light, upon which it is released to the storage ring.

The storage ring consists of two modes to generate x rays — the so-called wigglers or undulators housed in the linear sections that constrained the electron beams (bunch) to move in a zig-zag path by an alternately-arranged opposite poles of magnets, and bending magnets at locations in the ring that allowed the electron beams to orbit the storage ring. Although the synchrotron radiation may span a wide spectrum, the actual characteristics such as the frequency and the maximum intensity would depend on factors such as the number and energy of electrons in the storage ring. The x rays are then conveyed to the beamlines; a typical beamline set-up of Bessy II is shown in shown in Fig. 2.4. One of the main features of the beamline is the monochromator, through which the tuning of x rays, such as in selecting a particular wavelength or the nature of polarization is performed.

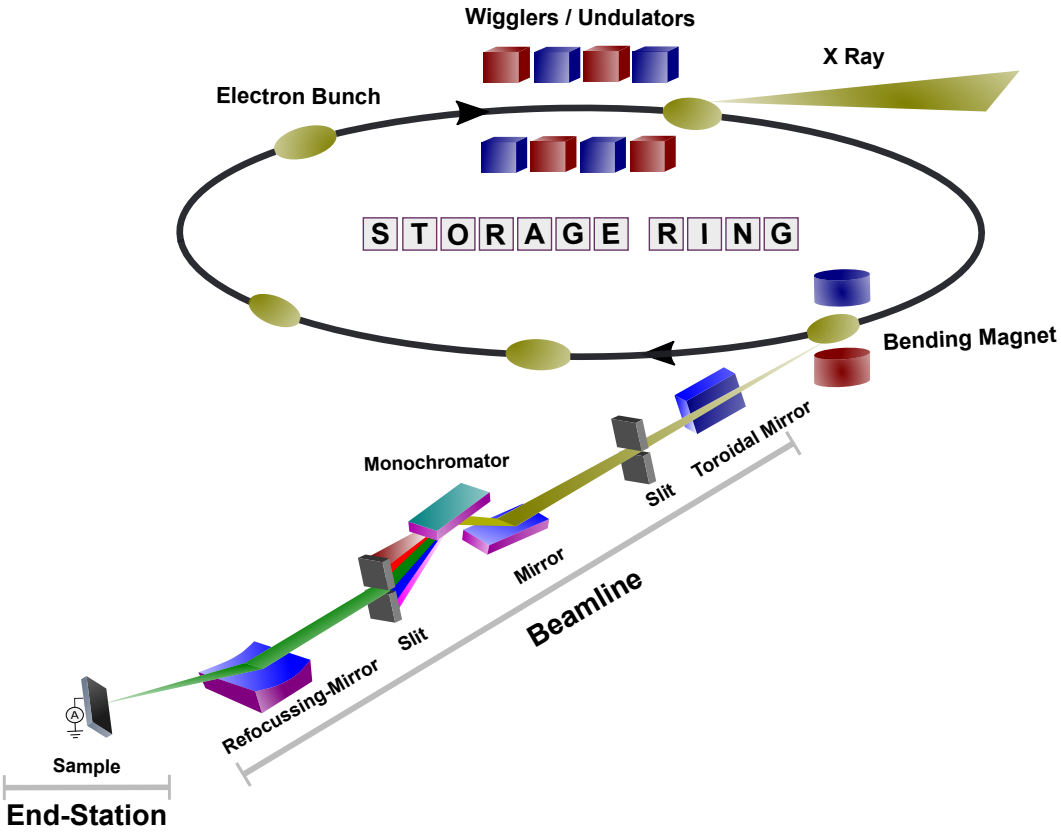

Figure 2.4: Sketch of the generation of x rays, along with a typical Beamline structure in BESSY II

2.4 Beamlines and end-stations

All the samples in the framework of this thesis are prepared and characterized *in-situ* at the beamlines UE56/2-PGM1, UE46-PGM1, and PM2 of BESSY II. In the case of beamline UE56/2-PGM1, the group-owned UHV chamber, of base pressure of about 8×10^{-10} mbar is used as the end-station. The chamber is equipped with characterization tools such as low-energy electron diffraction (LEED), x-ray photoelectron specroscopy (XPS), Auger spectroscopy and a sputtering unit. The chamber consist of two manipulators; the first manipulator is housed in the main chamber, where both the sample preparation and XAS measurements can be carried out. However, low-temperature measurements required for investigating spin-crossover molecules cannot be carried out at the first manipulator as it can only attain a minimum temperature of around 90 K on cooling with liquid helium. The second manipulator housed in an auxiliary chamber — connected to the main chamber — serves the purpose of low-temperature measurements of as low as 17 K. The UE56/2-PGM1 is an undulator-based beamline that provides soft x rays of energy in the range of 60—1300 eV, with linear (horizontal or vertical) as well as circular polarizations.

VEKMAG-PM2 is a dipole-based beamline, and can provide both linear and

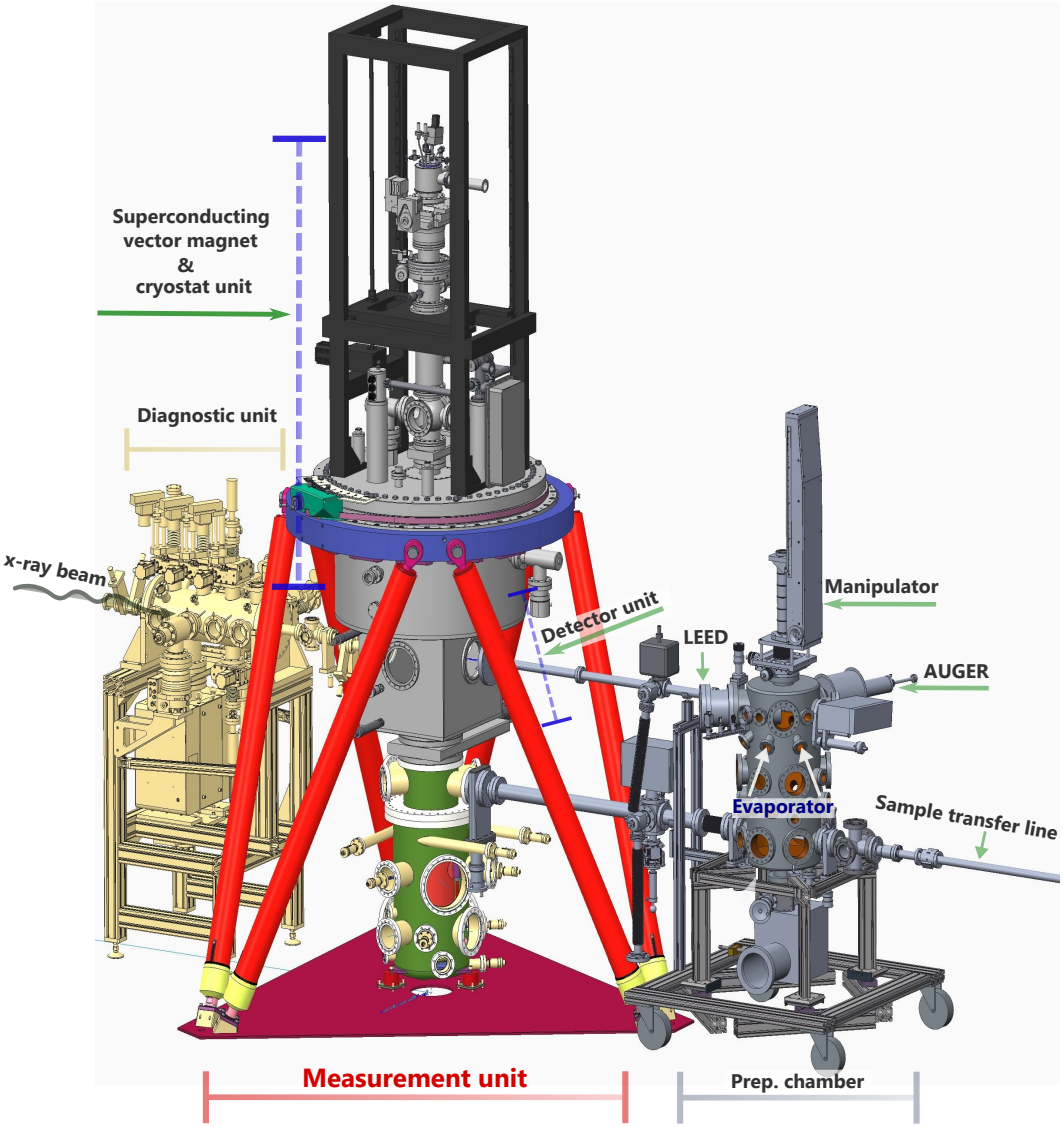

Figure 2.5: Sketch of the end-station at the PM2-VEKMAG beamline of BESSY II

circular polarizations with an estimated photon flux of about $\sim 1.6 \times 10^9$ photons s^{-1} mm^{-2}. The beamline is equipped with an end-station that consists of a separate sample preparation chamber and a measurement unit; the schematic representation is shown in Fig. 2.5. The sample preparation chamber (prep. chamber), as the name implies, is essentially designed for *in-situ* preparation of samples at a base pressure of about 2×10^{-10} mbar. The Auger spectroscopy and LEED of the prep. chamber allows one to assess the substrates' quality. For vacuum cleaning of Bi(111) and Au(111) substrates, the prep. chamber has a flashing stage made of molybdenum crucible for annealing, and a sputter unit. The prep. chamber's manipulator — and the sample — can be cooled to about 90 K with liquid nitrogen; this allows for deposition of molecules susceptible to desorption, and to carry out some preliminary XAS measurements at low temperatures. The sample can then be transferred to the

measurement unit through the horizontal transfer line, as indicated in Fig. 2.5. The measurement chamber with a base pressure of about 2×10^{-10} mbar, in turn, consists of an upper-part that houses a superconducting vector magnet and a cryostat, and a lower-part that houses a detector system. Apart from XAS measurements, XMCD measurements — requiring high magnetic fields to investigate the magnetic properties — can be done as well, as the superconducting vector magnet can generate 9 T in the beam direction, 2 T perpendicular to the beam direction and in the horizontal plane, and 1 T in the vertical plane. The cryostat at the upper-section of the chamber is attached to the manipulator and reaches down to the beam-focus location. The temperature at the sample position can be varied between 8—500 K, and with a cooling shield can go down to as low as 2.5 K.

The UE46-PGM1 beamline is undulator-based, capable of providing both linear and circular polarizations with a photon flux estimated at the sample position of about $\sim 1.6 \times 10^{10}$ photons s^{-1} mm^{-2}, which is roughly an order of magnitude higher than that of the VEKMAG-PM2 beamline. The photon flux is then attenuated by around a factor of 15 by placing an Al-foil in the path of the x-ray beam.[1] The end-station of the UE46-PGM1 beamline — called the high-field diffractometer — also consists of measurement unit and a prep. chamber. While the measurement unit have similar base pressures, the prep. chamber of the high-field diffractometer is higher than that of VEKMAG-PM2 by roughly an order of magnitude. The measurement unit has a superconducting magnet that can generate a magnetic field of up to 7 T along the x-ray beam direction. The cryostat can cool the sample to as low as 5 K. Most of the XAS studies presented in this thesis are performed in this beamline.

For investigating light-induced spin transitions at low temperatures, green LED (light emitting diode) — of wavelength $\lambda = 520$ nm, full width at half-maximum of 30 nm, and optical power of about 400 mW — is employed. Most of the optical measurements were carried out at the high-field diffractometer end-station. A focused light beam at the sample position is created by using an aspherical collimator and a spherical lens of focal lengths 32 and 500 mm, respectively. By means of a power meter, the photon flux density of the green LED at the sample position is estimated to be $4.2(8) \times 10^{14}$ photons s^{-1} mm^{-2}.

2.5 Processing of XA signal

2.5.1 Signal detection

One of the crucial challenges when investigating minute amount of molecules (sub-monolayers) deposited on a surface using x rays is in obtaining an optimized x-ray absorption (XA) signal from the molecules with respect to the XA signal coming from the substrate (background signal), because of the dominant signal from the

[1] SCMs are sensitive to photon fluxes

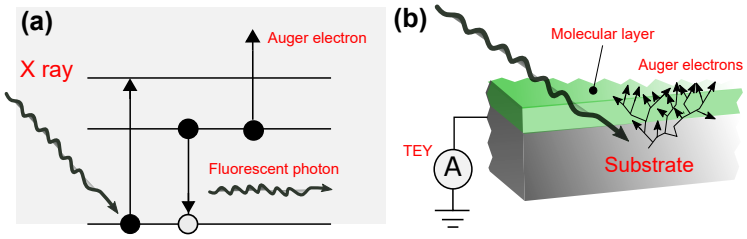

Figure 2.6: Sketch of: (a) core-electron excitation by soft x-ray absorption, and the subsequent deexcitation by emission of flourescent photons or the Auger electrons; (b) signal detection by TEY mode

latter. The mode of detecting the XA signal — which is proportional to the absorption cross-section — can be categorized as transmission, flourescent, and electron detection modes. The latter two arise from the de-excitation radiatively by emission of flourescent photon, or non-radiatively by Auger electron emission following the x-ray absorption process and subsequent scattering of low-energy electrons. This is depicted in Fig. 2.6 (a).

While the transmission mode is suitable for gas-based experiments where the molecular density can be easily varied, it becomes problematic for studying molecules on surfaces — mainly due to the requirement of thin substrates and the large background signal. Detection of XA signal based upon fluorescent photon is especially suitable for experiments in the gas-phase, the bulk samples (due to higher penetration depth of photons as compared to electrons), and in probing the ultrafast dynamics of molecules [96].

The third method used in detecting the XA signal is based on collecting the electron yield upon x-ray absorption, which is further sub-divided into three detection modes — Auger electron yield (AEY), partial electron yield (PEY), and total electron yield (TEY). The AEY mode involves selective detection of Auger electrons produced in a particular transition by means of an energy filter with its pass energy centred around that particular transition; this results in a large signal-to-background ratio. However, any occurrence of photoemission peaks within the window (pass energy) will increase the background signal and may interfere with the measurements. The PEY mode, on the other hand, involves detecting those electrons whose kinetic energies are greater than a certain threshold energy. By this procedure, the inelastically scattered Auger electrons contribute to the actual signal from the molecules, while low-energy electrons are filtered out. The PEY mode offers a higher signal, but lower signal-to-background ratio as compared to the AEY mode. The PEY measurements are realized by making use of a retarding grid detector: applying a negative grid potential prevents electrons with kinetic energy less than the threshold from entering the detector.

The TEY mode — which is the method used for acquiring the XA signal in the context of this thesis — involves collecting electrons of all energies from the sample, dominated by low-energy electrons with kinetic energy below about 20 eV. This is

shown in Fig. 2.6 (b). The TEY mode is the simplest set-up, and offers the highest signal but lowest signal-to-background ratio of all electron-yield-based signal detections. Between the signal detections based on flourescence and electron yield modes, the latter is more suitable for studying molecules on surfaces due to the much smaller mean free path of electrons, thereby being more sensitive to surface-lying molecules as compared to photons. Moreover, de-excitation by non-radiative Auger decay upon x-ray absorption dominates over the radiative flourescence decay by more than two orders of magnitude, at the K edge of N and C, and at the $L_{2,3}$ edge of transition metals.

2.5.2 Signal normalization

The measured XA signal for molecules on surfaces typically consists of a large background component from the substrate. In addition, the accuracy/quality of the signal is directly affected by any intensity variation of the x rays. The x-ray intensity may vary with time or with photon energy; the time variations might result from instabilities in the electron beam in the storage ring, and the intensity variation with photon energy may arise from the energy-dependent reflectivity or diffraction of the x-ray optics used in the beamlines. Therefore, it is imperative to consider the background subtraction and normalization of the signal in order to obtain a reliably quantifiable data.

The time– and photon energy–dependent intensity variations of x rays as mentioned above, can be prevented from affecting the acquired data by normalizing the signal obtained from the sample with the drain current of a Au grid in the case of the end stations at UE56/2-PGM1 and UE46-PGM1, or a Pt grid in the case of VEKMAG end station — placed upstream to the experiment. Further, the signal from a clean (adsorbate-free) substrate is also recorded so as to remove any possible artefacts in the spectra. The final XA signal (spectra) solely from the molecular adsorbate is then given by:

$$I = \frac{I_{sample} / I_{grid}^{sample}}{I_{substrate} / I_{grid}^{substrate}} \tag{2.8}$$

where, I_{sample} is the TEY signal from the adsorbate plus substrate, and I_{grid}^{sample} is the corresponding signal simultaneously measured from the grid; $I_{substrate}$ is the TEY signal from a clean, adsorbate-free substrate — and $I_{grid}^{substrate}$ is the corresponding signal simultaneously recorded from the grid. The spectra as given by equation 2.8 is further divided by their pre-edge intensity; in this way, the displayed spectra represent the relative contribution of the adsorbate over the whole energy range.

2.6 Sample preparation

The UHV chamber (preparaton chamber in the case of high-field diffractometer and VEKMAG end-stations) is fitted with a home-built molecular evaporator made of a tantalum Knudsen cell, from whence the molecular powder is evaporated onto the substrate. The evaporation rate is controlled from the frequency change of a quartz crystal attached to the Knudsen cell. The construction details of the evaporator are mentioned elsewhere [97]. Prior to the deposition, the evaporator (and the molecule in it) which is pumped separately from the chamber, is baked out for about 6—12 hours at around 90—120 řC, and then degassed to remove any residuals or contaminants. The pressure of the evaporator is usually in the range of 6×10^{-8} mbar before opening the valve to the main vacuum chamber for deposition. The various spin-crossover molecules (SCMs) investigated in the framework of this thesis have slightly different evaporation temperatures, but are generally in the range of 150—170°C. The molecules [Fe(H_2B(pz)$_2$)phen] and [Fe(H_2B(pz)$_2$)bipy] are synthesized by our collaborators at Christian-Albrecht Universität Kiel, in the group of Prof. Tuczek, following the procedures according to Real *et al.* [73]. Derivatives of the aforementioned molecules, such as [Fe(H_2B(pz)$_2$)$_2$(phen−me$_4$)], are synthesized according to the procedure mentioned in refs. 63, 98.

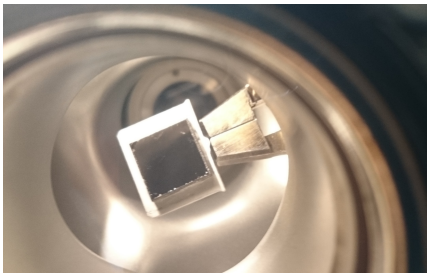

Figure 2.7: Typical image of the HOPG substrate — still on the wobble stick — taken right after cleaving the surface using a carbon tape in vacuum

The substrates used are Bi(111) and Au(111), and highly-oriented pyrolytic graphite (HOPG). It should be mentioned that HOPG is the more widely used substrate in the framework of this thesis, as it is — so far — the only known surface on which SCMs exhibit complete and reversible spin transition. Before molecule deposition, Bi(111) and Au(111) substrates are subjected to repeated annealing and sputtering cycles to rid the surfaces of contaminants; sputtering with Ar^+ at 600 eV and annealing at 350 K in the case of Bi(111), and sputtering with Ar^+ at 1.5 keV and annealing at ∼810 K in the case of the Au(111) single crystal.

The HOPG substrate (ZYA) of dimension $12 \times 12 \times 2\,\text{mm}^3$ and mosaic spread angle of $0.4(1)^\circ$ is purchased from Structure Probe, Inc. (West Chester, USA). A clean HOPG surface is obtained by cleaving away layers of the ambient-exposed surface with a double sided carbon tape in a load-lock, maintained at $\sim 10^{-7}$ mbar.

Fig. 2.7 shows a typical atomic force microscopy (AFM) image of an HOPG surface right after its surface is cleaved inside the vacuum chamber. It should be mentioned that repeated cleaving is often performed if the previous attempts couldn't yield flake-free surface. Having a large defect- and flake-free area of the surface is required for spin-crossover measurements, as prolonged x-ray exposure on a particular spot may alter the molecule or induce spin transitions, and the measurement spots needs to be changed from time to time so as to mitigate this effect.

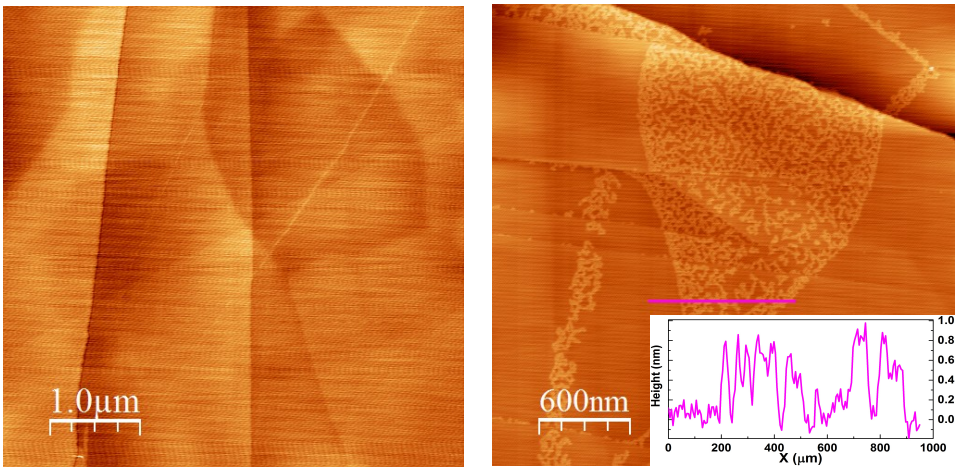

Figure 2.8: Left panel: AFM image of a clean HOPG surface, recorded at ambient conditions; Right panel: AFM image of a submonolayer of [Fe(H_2B(pz)$_2$)phen] on HOPG, also recoded at ambient conditions. Inset: Line profile (of the magenta line) as indicated

In the framework of this thesis, an emphasis is laid on investigating SCMs that are actually in contact with a surface. The modes of attachments and the self-assembly — crystallite formation or otherwise — of the molecules on the surface might play a crucial role in determining its spin switching behaviour. Towards the goal of understanding the nature of molecular arrangements on the surface, a series of atomic force microscopy (AFM) imaging of submonolayers of SCMs [Fe(H_2B(pz)$_2$)phen] and [Fe(H_2B(pz)$_2$)bipy] deposited on HOPG are performed. Fig. 2.8 (right-panel) shows one such AFM image of a submonolayer of [Fe(H_2B(pz)$_2$)phen] deposited on an HOPG surface, recorded at room temperature. The line profile in Fig. 2.8 (right-panel inset) reveals an island height in the range of 1.0 nm, which is consistent with the height of a molecule. Although the morphology of the molecular islands in vacuum may be different, one can conclude that no 3D crystallites are formed and that all the molecules are in contact with the surface. A submonolayer of [Fe(H_2B(pz)$_2$)bipy] on HOPG is also found to have the same structural arrangements [65]. The AFM (of Nanotec Cervantes) measurements are carried out *ex-situ* in ambient conditions in tapping mode using a Si cantilever of stiffness 2.7 N/m with a resonance frequency of 75 kHz.

2.6.1 Molecular coverage estimation

The frequency shift of a quartz micro balance integrated into the evaporator was used as a relative measure of the thickness of the molecular layer. The absolute thickness was estimated by comparing the integrated Fe L_3 XAS intensity at low molecular coverage to that of an Fe octaethyl-porphyrin (Cl)/Cu(001) reference sample which had been measured both with STM and XAS [99].

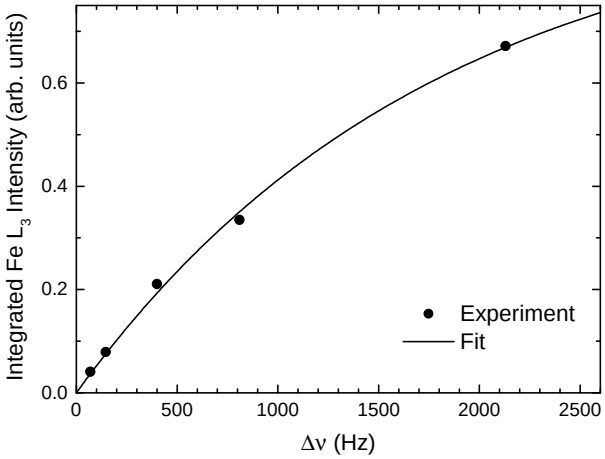

Figure 2.9: Thickness dependence of the absorption signal. The dots represent the integrated Fe L_3 absorption signal as a function of frequency change of the quartz crystal for the samples ranging from 0.35(4) to 10(1) ML. The solid line is the best fit of the data to Equation 2.11

The total electron yield for an adsorbate layer (A) of thickness Δx on a semi-infinite substrate (C) and a gold grid reference (G) — assuming that the attenuation length of the secondary electrons λ_e is material-independent and much smaller than that of the x rays ($\lambda_e \ll 1/\mu$, μ being the x rays absorption coefficient) — is given by [100, 101]:

$$Y_{\text{sample}} \sim \left(1 - \mathrm{e}^{-\frac{\Delta x}{\lambda_e}}\right)\lambda_e \mu_A + \mathrm{e}^{-\frac{\Delta x}{\lambda_e}}\lambda_e \mu_C \,, \quad Y_{\text{grid}} \sim \lambda_e \mu_G \tag{2.9}$$

After normalizing to the gold grid and to the clean substrate, the signal is normalized to the pre-edge absorption coefficient of the adsorbate. Assuming constant absorption of the substrate and grid in the relevant energy range ($\mu_C = \mu_C^{\text{pre}}$, $\mu_G = \mu_G^{\text{pre}}$) yields:

$$Y_{\text{sample/grid}} / Y^{\text{pre}}_{\text{sample/grid}} = \frac{\left(1 - \mathrm{e}^{-\frac{\Delta x}{\lambda_e}}\right)\frac{\mu_A}{\mu_C^{\text{pre}}} + \mathrm{e}^{-\frac{\Delta x}{\lambda_e}}}{\left(1 - \mathrm{e}^{-\frac{\Delta x}{\lambda_e}}\right)\frac{\mu_A^{\text{pre}}}{\mu_C^{\text{pre}}} + \mathrm{e}^{-\frac{\Delta x}{\lambda_e}}} \approx 1 + \frac{\mu_A - \mu_A^{\text{pre}}}{\mu_C^{\text{pre}}}\frac{\Delta x}{\lambda_e} + \ldots \tag{2.10}$$

In the low-coverage regime this signal is proportional to the ratio of the resonance intensity of the adsorbate and the absorption coefficient of the substrate after subtracting unity. To compare the adsorbate signal on different substrates, the ratio of

their absorption coefficients must be known. On metals the efficiency of electron extraction from the substrate changes with molecular coverage due to the change in work function. The XA intensity ratio between HOPG and Cu(001) substrates in the pre-edge region of the Fe L_3 edge has been determined by XA measurements under identical conditions with normalization to the gold grid. For clean HOPG and Cu(001) substrates the intensity ratio is $0.84(8)$ and decreases to $0.65(7)$ for a coverage of one monolayer. The reference sample has an areal density of 0.14 Fe ions/nm^2. Following ref. 31 and 72, an areal density of 0.82 Fe ions/nm^2 is assumed for 1 ML. Comparing the integrated Fe L_3 intensity of the two samples with lowest coverage, we obtain a factor of $205(25)$ Hz/ML that relates the frequency shift to the number of monolayers.

To analyze the thickness dependence of the absorption signal, the pre-edge signal can be subtracted after normalizing to the gold grid. Using the same assumptions as above yields:

$$Y_{\text{sample/grid}} - Y^{\text{pre}}_{\text{sample/grid}} \sim \left(1 - \mathrm{e}^{-\frac{\Delta x}{\lambda_e}}\right) \frac{\mu_A - \mu_A^{\text{pre}}}{\mu_G^{\text{pre}}}. \tag{2.11}$$

The best fit of this relationship to the experimental data is shown in Fig. 2.9. A comparably high value of $\lambda_e = 1780(230)\,\text{Hz} = 8.7(1.6)\,\text{ML}$ for the attenuation length of the electron yield is obtained. This may be attributed to a less dense packing of the atoms in the molecular layer and a lower degree of electronic conjugation compared to metals or graphite.

"Almost all aspects of life are engineered at the molecular level, and without understanding molecules we can only have a very sketchy understanding of life itself."

— Francis Crick

3

SPIN CROSSOVER ON A GRAPHITE SURFACE

This chapter explores the temperature-, light- and soft x-ray-induced spin-crossover in a submonolayer of [Fe(H_2B(pz)$_2$)bipy] deposited on an HOPG surface, with particular emphasis on the x-ray-induced process. While the x-ray-induced low-spin → high-spin state switching recorded at 5 K — commonly referred to as soft-x-ray-induced excited spin-state trapping (SOXIESST) — is saturated at about 84% conversion for a photon flux of $\sim 1 \times 10^{11}$ photons s^{-1} mm^{-2}, spin switching by either light or temperature is remarkably complete and highly efficient, mirroring the bulk behaviour. This study is an attempt at a closer examination of the interaction of spin-crossover molecules with soft x rays, necessitated by the emergence of x-ray absorption spectroscopy as one of the most effective tools to investigate spin-crossover molecules on surfaces. Apart from exhibiting SOXIESST phenomenon, the system also exhibits reverse-SOXIESST, i.e., high-spin → low-spin state conversions. Based upon the observed spin-state switching rates, a case is made for SOXIESST to be resulting from the interactions between x-ray-induced secondary electrons and the spin-crossover molecules. Further, the spin-state switching rates are found to be highly dependent upon the flux of the x-ray beam; this observation is a pointer for the necessary precautions to be undertaken while using XAS to investigate spin-crossover molecules.

The main results from this chapter have been published in:
J. Phys. Condens. Matter **29**, (2017) 394003.

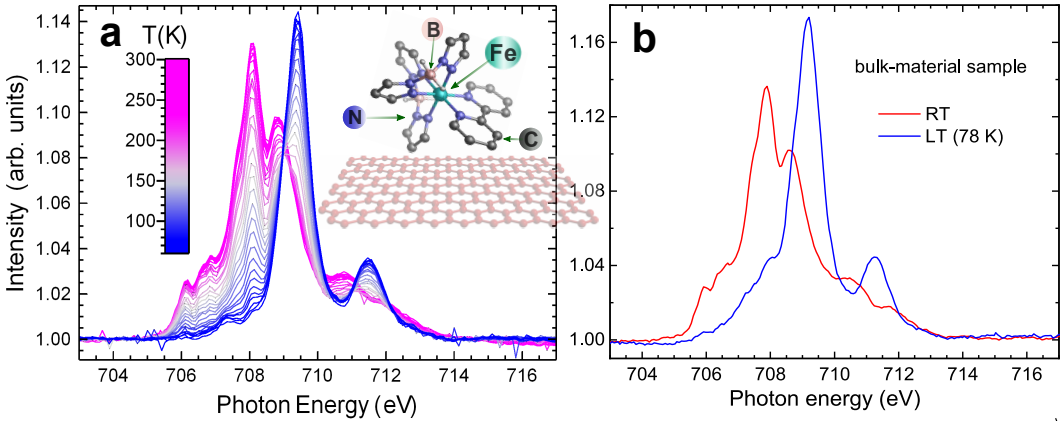

Figure 3.1: Spin state as revealed by x-ray absorption spectroscopy. (a) Temperature-dependent Fe L_3 edge XA spectra of 0.8 ML of [Fe(H_2B(pz)$_2$)bipy] on HOPG from 300 to 50 K; (b) The corresponding spectra of the bulk-material sample recorded at 300 K (magenta) and at 78 K (blue) of [Fe(H_2B(pz)$_2$)bipy]. Insets of (a) is a rendition of [Fe(H_2B(pz)$_2$)bipy] deposited on an HOPG substrate

3.1 Temperature- and light-induced spin transition

Unless otherwise stated, the XA spectra are recorded with the x-ray beam damped with an Al-foil, which reduces the photon flux I_0 by about a factor of 15. This is done so as to mitigate the effect of x rays — during the data acquisition — in the spin-state while investigating the their effects with temperature or light. Fig. 3.1 (a) shows the temperature-dependent Fe L_3-edge XA spectral shapes of 0.8 ML of the SCM [Fe(H_2B(pz)$_2$)bipy] adsorbed on an HOPG substrate (hereafter referred to as "the sample"), recorded simultaneously as the sample temperature is decreased from room-temperature (RT), down to low-temperature(s) (LT), at the rate of 4 K min^{-1}. The RT and LT spectra show contrasting line shapes: the RT spectrum is characterized by two main peaks at 708.3 and 709.1 eV, while the LT spectrum — at 70 K and down to 50 K — is characterized by a single peak at 709.8 eV; the spectra at any other intermediate temperature is a linear combination between the two.

The change in the spectral patterns (as described above) has been established as reflecting the change in the electronic structure — and hence the change in the spin state — of SCMs; the RT spectrum representing the high-spin state and the spectrum at 70 K representing the low-spin state [31, 64, 69]. The change in the spin state with temperature can be further confirmed by comparing with the XA characteristics of [Fe(H_2B(pz)$_2$)bipy] in the bulk, which is reported to exhibit HS→LS state conversion with temperature, light, and pressure [49, 73, 96]. Fig. 3.1 (b) shows the Fe L_3-edge XA spectra of the bulk[1] [Fe(H_2B(pz)$_2$)bipy] measured at RT and at 70 K: The spectra recorded at similar temperatures bore similar patterns, confirming the

[1]The bulk sample for XAS measurements is prepared by crimping the molecular power onto an indium foil

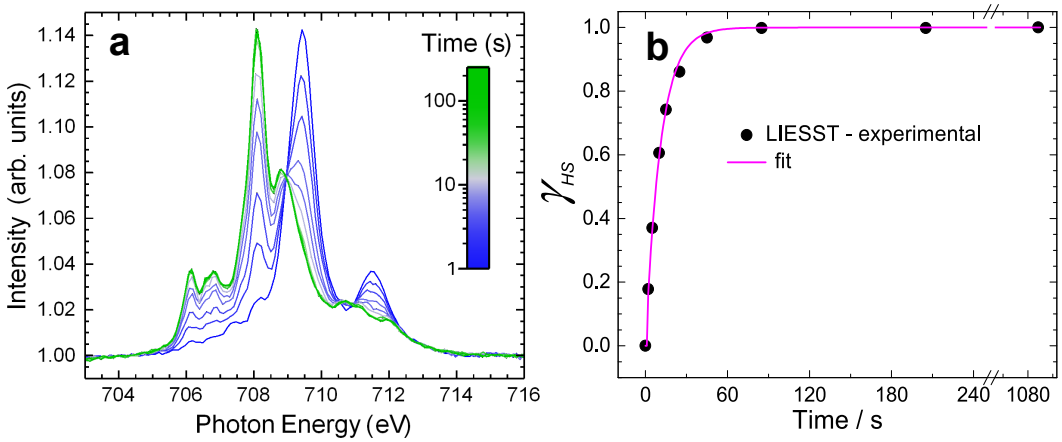

Figure 3.2: Light-induced excited spin-state trapping at 5 K. (a) Fe L_3-edge XA spectra of 0.8 ML of [Fe(H_2B(pz)$_2$)bipy] on HOPG at 5 K recorded successively after exposure to green LED for a particular duration; (b) Growth of HS fraction γ_{HS} with duration of illumination

spin-crossover of [Fe(H_2B(pz)$_2$)bipy] in direct contact with the HOPG surface.

It is worth noting that — although not shown in the Figure — the spectra recorded below 50 K successively at the same spot on the sample show a gradual increase in the peak intensities corresponding to the HS state, at the cost of a corresponding reduction of the peak intensity corresponding to the LS state; this is due to the x-ray-induced LS $\rightarrow$ HS state conversion, which is commonly referred to as soft x-ray-induced excited spin-state trapping (SOXIESST) [66]. The SOXIESST rate is dependent upon the photon flux of the x-ray beam. The LS spectra at low-temperatures (below 70 K) can be obtained at any other locations not previously exposed to the x-ray beam.

The sample also exhibits a complete conversion from LS-to-HS state at low-temperatures on illumination with light. The light-induced spin-state conversions — commonly referred to as light-induced excited spin-state trapping, LIESST [50] — is highly efficient, with the conversion time constant estimated to be $\approx 20.1(3)\,s^{-1}$ for a photon flux of $4.2(8) \times 10^{14}$ photons $s^{-1}mm^{-2}$. The LIESST measurements are carried out at 5 K with a green LED of wavelength 520 nm; the sample is illuminated for a particular duration, and the spectra recorded after each exposure, shown in . The HS fraction — γ_{HS} — corresponding to a particular spectral shape is estimated by fitting it to a linear combination between the spectrum recorded before illumination ($\gamma_{HS} = 0$) and the saturated spectrum obtained after prolong illumination of about 10 min ($\gamma_{HS} = 1$), which are taken as reference LS state and HS state, respectively. This is shown in Fig. 3.2 (b).

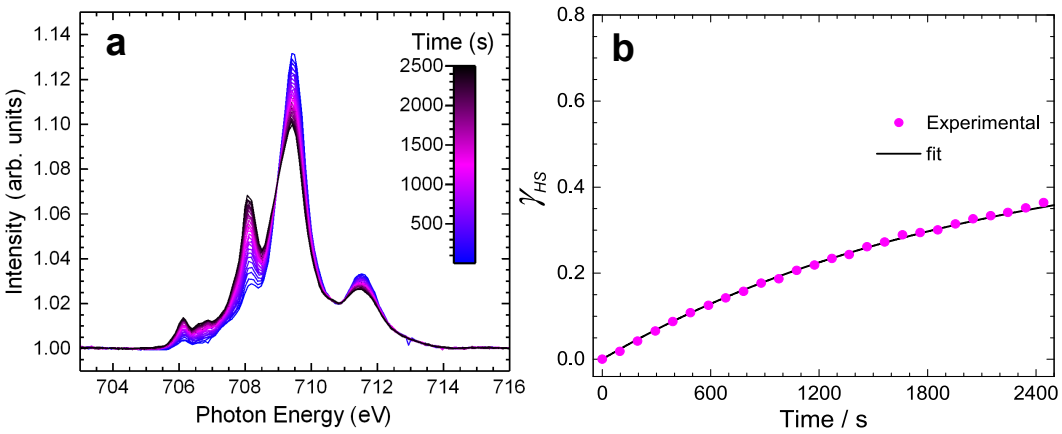

Figure 3.3: (a) Time evolution of x-ray-induced spin-state switching of 0.8 ML of [Fe(H_2B(pz)$_2$)bipy] on HOPG at 5 K traced by the Fe L_3 XA spectral change; and (b) the estimated γ_{HS} from the spectra shown in (a) with the fit using model (I). The x-ray beam is damped with a thin Al-foil that decreased its intensity by a factor of 15.

3.2 X-ray-induced spin transition

The SOXIESST phenomenon in SCO complexes is appreciable only at low temperatures, for the sample under investigation, <70 K. As the sample is prone to x-ray-induced switching at 5 K, in order to follow a proper build-up of the HS state by x rays, starting from the LS state, the first spectrum of the series is recorded at a virgin spot on the sample, and if there is any trace of a peak (or bump) at 708.3 eV indicative of the presence of x-ray-induced HS state, the temperature is increased to 80 K to obtain the pure LS state and subsequently cooled to 5 K. In any case, if a spectrum shows no bump at 708.3 eV, it is taken as the pure LS spectrum. Fig. 3.3 (a) shows the change in the Fe L_3 spectral shape of the sample at 5 K, recorded successively at the same spot with an x-ray beam whose photon flux $\mathbf{I_0}$ is damped with an Al-foil. The time stamp for each spectrum as it is recorded successively one after the other is taken as the time when the resonance peak (708.3 eV) is reached during the scan. Fig. 3.3 (b) shows the quantified build-up of γ_{HS} with x-ray exposure.

In order to estimate the rate constants of the switching process, a simple model (hereafter referred to as model (I)), LS $\rightleftharpoons$ HS, is applied. The differential rate equation of the process can be written as:

$$\frac{d\gamma_{HS}}{dt} = k_{1d}\gamma_{LS} - k_{2d}\gamma_{HS} \tag{3.1}$$

where k_{1d} and k_{2d} are the rate constants for the transitions LS $\rightarrow$ HS and HS $\rightarrow$ LS, respectively (d in the subscripts stands for "damped x-ray beam"). Solving the above equation and fitting it with the experimental data by the method of least squares, yields the values of k_{1d} and k_{2d} as $3.50\,(3)\times10^{-4}\,\mathrm{s}^{-1}$ and $2.3\,(1)\times10^{-4}\,\mathrm{s}^{-1}$, respectively, with the saturation γ_{HS} at $\sim$0.60(5). This is the x-ray contribution to

the switching process while investigating spin-crossover complexes at low temperatures, and is highly dependent upon the photon flux, as will be shown in the following. Here, for the damped x-ray beam, the possibility of SOXPC is not taken into account as the HS spectrum can be obtained by light illumination after the SOXIESST series measurements.

Fig. 3.4 (b) shows the x-ray-induced spin-state switching with the full photon flux $\mathbf{I_0}$, *i.e.,* without damping the beam with Al foil, where the switching is carried out both ways: the so-called SOXIESST (LS $\rightarrow$ HS), when starting from the LS state, represented by the lower curve, and reverse-SOXIESST (HS $\rightarrow$ LS), when starting from the HS state — obtained by illumination with green LED — represented by the upper curve. It must be mentioned that this is the first report of reverse-SOXIESST. The reverse-SOXIESST measurements are done after the sample has been saturated to the HS state by exposure to green light. Also shown in Fig. 3.4 (a) & (c) are the Fe L_3 edge XA spectra at two different exposure times to the x-ray beam at 106 s and 900 s, respectively.

For a quantitative modelling of the kinetics, in addition to model (I), a second model (hereafter referred to as model (II)), LS $\rightleftharpoons$ HS, LS $\rightarrow$ LS', and HS $\rightarrow$ LS', is applied. The LS' state refers to the altered and irreversible low-spin component that results from the interaction of the SCO complex in the LS state with the x rays, by a process termed as soft x-ray-induced photochemistry (SOXPC) by Collison *et al.* [66], who observed this phenomenon for the first time. No related report of this phenomenon is to be found in the literature since then. The origin of SOXPC is still unknown at the molecular level.

In SOXIESST, the spin switching saturates at $\sim$84(5)% HS state while the reverse-SOXIESST process is much slower, attaining about $\sim$13(5)% switched to the LS state for the same amount of x-ray exposure, as shown in Fig. 3.4 (b). Incomplete switching by x rays was also reported in bulk $Fe(phen)_2(NCS)_2$, with saturation at about 90% HS state on exposure to a photon flux of 12 % of $\mathbf{I}_0$ [102], while complete switching is reported for the same bulk molecule with a photon flux $\mathbf{I}_0$ [66], apparently before the onset of SOXPC. According to model (II), the differential rate equations for each species are given by the following mass balance simultaneous equations,

$$\frac{d\gamma_{LS}}{dt} = -k_{1f}\gamma_{LS} + k_{2f}\gamma_{HS} - k_{3f}\gamma_{LS} \tag{3.2}$$

$$\frac{d\gamma_{HS}}{dt} = k_{1f}\gamma_{LS} - k_{2f}\gamma_{HS} - k_{4f}\gamma_{HS} \tag{3.3}$$

$$\frac{d\gamma_{LS'}}{dt} = -\left(\frac{d\gamma_{HS}}{dt} + \frac{d\gamma_{LS}}{dt}\right) \tag{3.4}$$

where k_{1f}, k_{2f}, k_{3f}, and k_{4f} are the rate constants for the transitions LS $\rightarrow$ HS, HS $\rightarrow$ LS, LS $\rightarrow$ LS', and HS $\rightarrow$ LS', respectively. (The f in the subscripts stands for

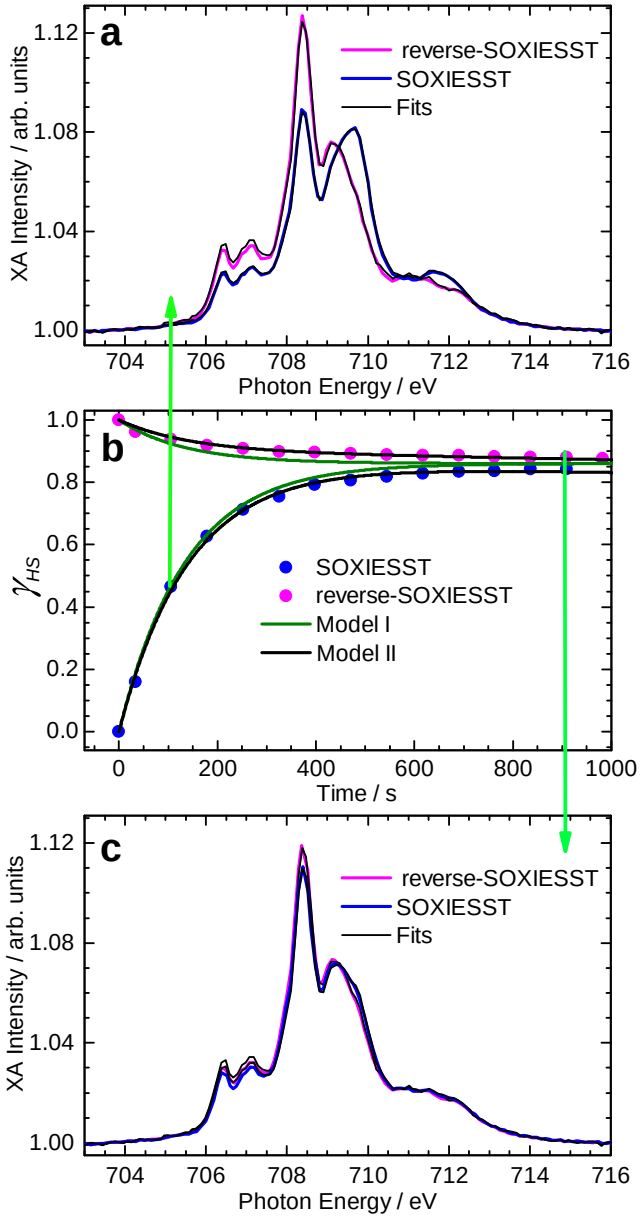

Figure 3.4: (b) Time evolution of x-ray-induced spin-state switching of 0.8 ML of [Fe(H_2B(pz)$_2$)bipy] on HOPG at 5 K, with an intensity $\mathbf{I}_0$. The orange and black lines are the fits from model (I) and model (II), respectively. (a) and (c) represent the Fe L_3 edge XA spectral shapes after x-ray exposure times of 106 s and 900 s, respectively, starting from a pure HS state (red dots, reverse-SOXIESST) and a pure LS state (olive dots, SOXIESST). The black lines are fits of the spectra obtained by the linear combination of the pure HS and LS spectra so as to extract the spin fractions.

"full photon flux".) Solving the above differential rate equations simultaneously while satisfying the initial conditions at t = 0, *i.e.* (i) $\gamma_{HS} = 0$, $\gamma_{LS} = 1$, (SOXIESST) and (ii) $\gamma_{HS} = 1$, $\gamma_{LS} = 0$ (reverse-SOXIESST), and fitting to the experimental data yields the values of the rate constants as $k_{1f} = 6.1(1) \times 10^{-3}\,\mathrm{s}^{-1}$, $k_{2f} = 6.5(3) \times 10^{-4}\,\mathrm{s}^{-1}$, $k_{3f} = 3.9(4) \times 10^{-4}\,\mathrm{s}^{-1}$, and $k_{4f} \to 0$. (The absence of the conversions from HS to LS' is in agreement with that reported in the literature [66].) This gives the SOXIESST effective cross-section ($k_{1f}/\mathbf{I}_0$) as $\approx 6\,\text{Å}^2$, which is $\approx 5.0 \times 10^2$ times the effective cross-section of LIESST reported for 0.4 ML of [Fe(H_2B(pz)$_2$)phen] on HOPG [31], and about ≈ 44 times that reported for this complex in thin film [103]. Applying model (I) with the same initial conditions as above fitted quite well with the experimental spin switching rates initially, but deviates with the increase in exposure time, as shown in Fig. 3.4 b, blue curve, which, in other words, confirms the time evolution of the LS' states.

To discuss the mechanism responsible for the observed SOXIESST and reverse-SOXIESST, we first estimate the x-ray absorption rate per molecule. The off-resonant absorption cross-section of an [Fe(H_2B(pz)$_2$)bipy] molecule can be calculated as the sum of the tabulated values of the absorption cross sections of its chemical constituents [104] to be 0.050 Å^2 at 690 eV. The cross section at resonant absorption at the Fe L_3-edge is typically a factor of 5 to 15 higher than the tabulated cross section edge jump of 0.015 Å^2. The estimated absorption rates per [Fe(H_2B(pz)$_2$)bipy] molecule in our expriment, as obtained from the product of the cross section and the photon flux density, have values of 0.5×10^{-4} s^{-1} and 2×10^{-4} s^{-1} for the non-resonant and resonant absorption, respectively. These are much lower than the observed SOXIESST transition rates. Hence, we can rule out the possibility of spin switching directly by x-ray absorption in the molecules. On the other hand, the estimated resonant absorption rate is in the same range as the experimentally observed rate of SOXPC, suggesting that direct x-ray absorption in the molecules might indeed be responsible for the photochemistry.

In the case of hard x-ray-induced spin-state switching reported for the bulk Fe(phen)$_2$(NCS)$_2$ complex [105], the authors attributed secondary electrons originating from a remote ionization as being responsible for the switching process. It can be assumed that the same process applies for SOXIESST as well. Interestingly, no hard x-ray-induced photochemistry (HAXPC) was observed. The reason for the observation of SOXPC and the absence of HAXPC could lie in the possible difference in the complexes' effective cross section to soft and hard x rays.

The dependence of the x-ray-induced spin-state switching on photon energy *i.e.*, at resonant or non-resonant energy, can provide additional information on the underlying mechanism. If, for example, SOXIESST were due to direct excitation of the molecules by x rays, one would expect to see a large difference in the switching rates for illuminations at resonance (709.8 eV) or off-resonance (say, 690.0 eV) x-ray energies, paralleling the difference in resonant and non-resonant absorption cross section. To test this, two x-ray-induced switching rates — starting from the

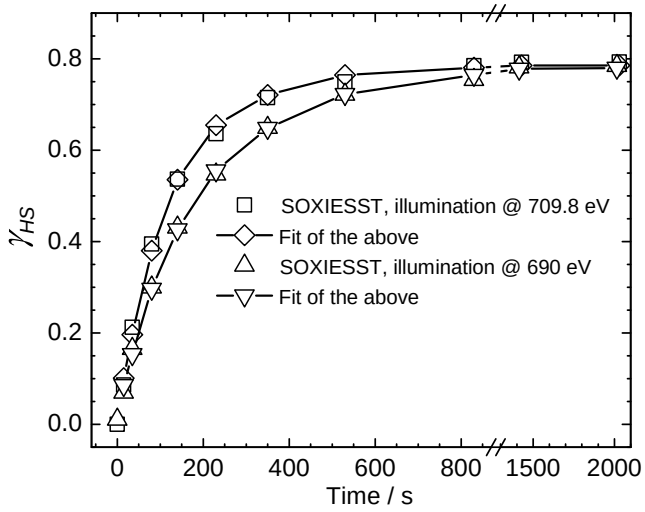

Figure 3.5: Time evolution of SOXIESST upon illumination with two different photon energies: at resonance (709.8 eV), □, and at off-resonance (690.0 eV), △. Also shown are the fits based on model (I), ◊ and ▽.

LS states — are recorded by illuminating the sample at resonance photon energy (709.8 eV) and at an off-resonance (690.0 eV). For both series, the sample is exposed alternatively to the monochromatic x-ray beam with full photon flux, and to an attenuated x-ray beam for recording the spectra. The time evolution of γ_{HS} for both series is shown in Fig. 3.5 (□ and △ for 709.8 and 690.0 eV, respectively). By using model (I) and ignoring SOXPC for simplicity, the time evolution of γ_{HS} induced both by monochromatic x-ray exposure and that during recording the spectrum has a solution of the form:

$$\begin{aligned}\gamma_{HS}(\Delta t_1, \Delta t_2) = \frac{e^{-(k_{1d}+k_{2d})\Delta t_1-(k_{1m}+k_{2m})\Delta t_2}}{(k_{1d}+k_{2d})(k_{1m}+k_{2m})}[e^{(k_{1d}+k_{2d})\Delta t_1}(k_{1d}k_{2m}-k_{2d}k_{1m} \\ + e^{(k_{1m}+k_{2m})\Delta t_2}k_{1m}(k_{1d}+k_{2d}))+(k_{1m}+k_{2m}) \\ (k_{1d}(\gamma_{HS0}-1)+k_{2d}\gamma_{HS0})]\end{aligned} \tag{3.5}$$

where Δt_1 is the time it takes to record one spectrum, which is ~ 73 s, Δt_2 is the discrete exposure time to the unattenuated monochromatic x rays, and γ_{HS0} is the HS fraction before every consecutive exposure to the x rays. The rate constants k_{1d} and k_{2d} have the same meaning as in equation (1), while k_{1m} and k_{2m} are the rate constants for the transitions LS $\rightarrow$ HS and HS $\rightarrow$ LS induced by monochromatic x rays, respectively. Substituting the value of the rate constants k_{1d} and k_{2d} obtained from equation (1) into equation (5) and fitting it with the experimental data of Fig. 3.5 by the method of least squares, the following values are obtained for the rate constants: $k_{1m} = 5.5(3) \times 10^{-3}\,\mathrm{s}^{-1}$ and $k_{2m} = 1.5(1) \times 10^{-3}\,\mathrm{s}^{-1}$ on illumination with x-ray energy at resonance (709.8 eV) and $k_{1m} = 3.6(2) \times 10^{-3}\,\mathrm{s}^{-1}$ and $k_{2m} =$

$1.02(7) \times 10^{-3}\,s^{-1}$ for the off-resonance (690.0 eV) illumination. The probabilities of LS $\rightarrow$ HS transitions, $k_{1m}/(k_{1m}+k_{2m})$, and HS $\rightarrow$ LS transitions, $k_{2m}/(k_{1m}+k_{2m})$, are remarkably similar in both cases; *i.e.*, ~ 0.79 and ~ 0.21, respectively.

The difference in the rates of about 50% between resonant and off-resonant illumination is clearly smaller than the difference in absorption, thus also ruling out a direct optical excitation of the molecules as responsible mechanism for SOXIESST. At the resonance x-ray energy, the photocurrent, and thus the number of emitted secondary electrons, is higher by only about 12 % than at the off-resonance energy. These 12% additional secondary electrons, however, are generated in the molecular layer and may thus have a higher probability of interacting with the molecules than the electrons originating from the substrate. This could account for the about 50% higher rate constants at the resonance as compared to the off-resonance case. This argument is supported by the report of a similarly high rate constant for SOXIESST as reported herein for a bulk SCO complex, but obtained with a much reduced photon flux of about 12 % of $\mathbf{I}_0$) [102]. This is consistent with more efficient switching when all the secondary electrons originate from the complex itself.

Electron-induced excited spin state trapping (ELIESST) has been reported for a bilayer of [Fe($H_2B(pz)_2$)phen] on Au(111), studied by STM: the LS to HS transition is observed by applying a sample voltage in the range of 2.5 – 3.0 V with the STM tip positioned at a nanometer above the molecules, and a HS to LS transition is observed when the sample voltage is maintained in the range of 1.6 – 1.8 V and the current strongly increased [68]. The authors suggest that the LS $\rightarrow$ HS spin transition occurs via a mechanism where electrons are injected into the unoccupied orbitals that excite the LS molecule to LS^-, followed by a relaxation to an intermediate state I^-, which then statistically relaxes to the HS or LS states. This is further corroborated by a DFT calculation that showed that for LS molecules, the energy difference between HOMO and LUMO is ~ 2.1 eV [68]. We propose a similar mechanism for SOXIESST: for the LS molecule, the injection of the x-ray-induced secondary electrons to the unoccupied orbitals leads to a weakening of the Fe - N coordination bond. Consequently, the bond lengthens, resulting in a reduction of the ligand field strength. When the electron hops off, the molecule relaxes statistically to the HS and the LS states.

The reverse–SOXIESST process may be argued to undergo a similar mechanism to that of reverse–LIESST process. Recall that the LIESST process in SCO complexes is understood as being due to the intersystem crossing that involves the excitation of electrons from the electronic ground state ($^1A_1$, LS state) to the metal-to-ligand charge transfer states (^{1,3}MLCT), from whence the electrons undergo fast decay to the quintet ligand field state ($^5T_2$, metastable HS state) *via* the low-lying triplet ligand field excited states (^{3}T), which is shown in Fig. 1.4. Conversely, the reverse–LIESST process can be carried out by irradiation in the near-IR region, whereby the electrons in the $^5T_2$ HS state are excited to the ^{5}E ligand field state, from whence they relax to the $^1A_1$ LS state, although it is not as efficient as

that of LIESST because of the large overlap between the ^5E and $^5T_2$ states [106]. The time constants for every step involved in the process have been probed in detail by ultrafast optical and x-ray spectroscopy [107, 108].

For the electron-induced HS $\rightarrow$ LS transition (reverse-SOXIESST), a strong injection of electrons of energy $1.6-1.8$ eV to the sample was needed [68]. This energy is in the same range as that of the energy difference between $^5T_2$ and ^5E states — indicating that reverse–SOXIESST process might occur *via* the intersystem crossing in a manner similar to reverse–LIESST process, possibly through the direct excitation of electrons in the metastable HS state, caused by interaction with secondary electrons. Moreover, reverse-SOXIESST process is relatively slow, similar to the reverse-LIESST process. A similar effect of soft x-ray and optical near-IR irradiation as in SCO complexes (HS $\rightarrow$ LS) has also been reported in another class of molecules, namely cobalt dioxolene, which undergoes redox isomerism both with soft x-ray and optical near-IR irradiations [109].

One can get a better appreciation of the mechanism proposed herein for SOXIESST (and reverse–SOXIESST) processes from the energy distribution of secondary electrons from metal–x-ray interactions; the secondary electrons' energy vs. intensity distribution from various conducting surfaces, induced by x rays of the energy range $100-10{,}000$ eV, are fairly similar and can best be described as a convolution of two exponential decays or of a Gaussian and an exponential decay, having maximum intensity in the region of $\sim 1 - 2$ eV [110]. These electrons could then induce the spin-state switching, similarly to ELIESST, by injection into unoccupied molecular orbitals for LS $\rightarrow$ HS and by an excitation of the molecule's electronic system by inelastic scattering for the HS $\rightarrow$ LS transition.

In fact, the assumption made herein of SOXIESST (and reverse-SOXIESST) as being caused by x-ray–induced secondary electrons has been proven experimentally by Wäckerlin *et al.* [111].[2] In a thin film (70 nm) of [Fe(H_2B(pz)$_2$)bipy] prepared on a ferrolectric substrate PMN-PT ([Pb($Mg_{1/3}Nb_{2/3}$)O_3]$_{1-x}$[$PbTiO_3$]$_x$, x = 0.32), SOXIESST measurements performed at 3 K are found to be greatly dependent upon the direction of poling the substrate: for the substrate with the electric dipoles pointing away from the substrate's surface ((+)-poled substrate), the SOXIESST rates are found to be more than an order of magnitude larger as compared to that from the substrate with the electric dipoles pointing in the opposite direction (pointing inwards, (–)-poled substrate). This observation can be understood in terms of the higher probability of interaction of the x-ray-generated secondary electrons and the molecules in the case of (+)-poled substrate. The (+)-poled substrate has higher electron affinity than the (–)-poled one; consequently, more secondary electrons are prevented from leaving the substrate and are confined around the surface. (This process will result in a reduced total electron yield (TEY) — the mode by which XAS is recorded — from the (+)-poled substrate as compared to the negatively-poled one, as is reported [111].) The surface-confined secondary elec-

[2] This is a later study than the SOXIESST investigations reported herein

trons, in the case of the (+)-poled substrate, then caused excitation of the molecules, resulting in higher SOXIESST yield [111].

"I believe alien life is quite common in the universe, although intelligent life is less so. Some say it has yet to appear on planet Earth."

— Stephen Hawking

4

TRACING THE EVOLUTION OF COOPERATIVE SPIN CROSSOVER

This chapter attempts to address the evolution of cooperative effects in the spin-state transition of SCMs — an issue of huge interest, both from the fundamental and application point of view — with an [Fe(H_2B(pz)$_2$)bipy] molecules deposited on an HOPG substrate. Between the submonolayers and the multilayers, the cooperative effects couldn't have been more dramatic — the submonolayers exhibit an apparent anticooperative spin switching, while the multilayers starting from a bilayer exhibit a distinct cooparative behaviour, as evidenced by the degree of steepness in their temperature-dependent spin-crossover curves. The thermodynamic parameters driving the spin-transition process is derived using the classical model of Slichter and Drickamer. In contrast, the light-induced spin-crossover at low temperature show a non-cooperative spin switching, right from the submonolayers to multilayers. The stability of the light-induced HS state at low temperatures for molecules in direct contact with the substrate — namely, 0.35(4)- and 0.65(8)-ML samples — are further investigated at 8, 20, 30, and 40 K; it revealed a rather unstable HS state, and unusual HS→LS decay, as compared to the bulk behaviour. These findings are relevant for applications involving spin-state bistability, and are expected to serve as useful guidelines in designing SCM-based devices.

The main results from this chapter have been published in:
Nat. Commun. **9**, 2984 (2018).

4.1 Introduction — Cooperative effects

The spin-transition process in SCMs is largely governed by the nature and the degree of interactions the molecules undergo during the transition process. Such inter-molecular interactions — commonly referred to as cooperative effects, which means a correlation between the transiting spin centres giving rise to cooperative or anticooperative interactions — are not hard to see, considering that the spin-state switching from the HS state to the LS state or *vice-versa* involves a re-ordering of the electronic configurations, a change in the magnetic state, as well as a change in the molecules' sizes. The re-ordering of the electronic configurations in the two different spin states, of course, arises from the different occupancy of the e_g and t_{2g} energy levels — the energy levels resulting from the ligand-field-induced $3d$ orbital splitting of the central Fe(II) ion. It has been recently proposed that electrostatic interactions arising out of these electronic re-arrangements might be largely responsible for cooperative effects in the spin transition of SCMs [46, 47]. Traditionally, however, for bulk SCMs, elastic interactions between the molecules have been invoked to rationalize the occurrence of cooperativity: the elastic strains arises from the volume contraction (or expansion) accompanying the spin transition from the HS-to-LS (or LS-to-HS) [42, 112].

Exploring the nature and degree of cooperative effects — if it is cooperative or anticooperative and their coupling strengths — for molecules on surfaces is a topic of huge interest, as these effects ultimately determine the spin-state bistability and hysteresis. But such studies are rare and pretty much unexplored mainly due to the challenges associated with retaining control over the SCO property upon contact with surfaces. Herein, an attempt is made to address this issue with an [Fe(H_2B(pz)$_2$)bipy] molecule deposited on an HOPG surface — where the spin-crossover behaviour is unhindered by the surface and a complete spin switching of the HS $\leftrightarrow$ LS state with temperature, and LS $\rightarrow$ HS state with light at low temperatures are achieved at coverages ranging from 0.35(4) to 10(1) ML. The HS$\rightarrow$LS relaxation of the submonolayers at low temperatures (8—40 K) showed a dramatic departure from the bulk–material behaviour.

4.2 Cooperative effects in temperature-induced spin transition

Samples of [Fe(H_2B(pz)$_2$)bipy] deposited on an HOPG surface of coverages 0.35(4), 0.69(8), 2.0(3), 3.9(5) and 10(1) ML are prepared and their spin states are probed on varying the temperature from room temperature (RT) to low temperature (LT) of upto 5 K. The spin states are traced through the L_3 edge of the central Fe(II) atom, *i.e.*, electronic transitions involving $2p^4_{3/2}3d^6 \rightarrow 2p^3_{3/2}3d^7$. The samples are cooled at the rate of 4 K$\cdot$min^{-1} and their Fe L_3 spectra are recorded simultaneously. As an example — and in order to avoid monotony — the RT and LT spectra of only the

10(1)- and the 0.35(4)-ML samples are shown in Fig. 4.1 (d and e); the RT spectrum is characterized by two main peaks at 708.1 and 708.9 eV, and the LT spectrum [1] by a single main peak at 709.4 eV. These spectral line shapes have been established as characteristic of the HS and the LS states, as already described in Chapter 3. The spectrum at any other intermediate temperature is a linear combination between the two. As an example, Fig. 4.2 (a) shows the systematic variation of the spectral profiles for the 3.9(5)-ML sample, as it is cooled from RT down to 50 K. This characteristic variation in the spectral profiles as a function of temperature is true for all the samples, albeit the value of temperature in obtaining the characteristic LT spectra are different across the different samples.

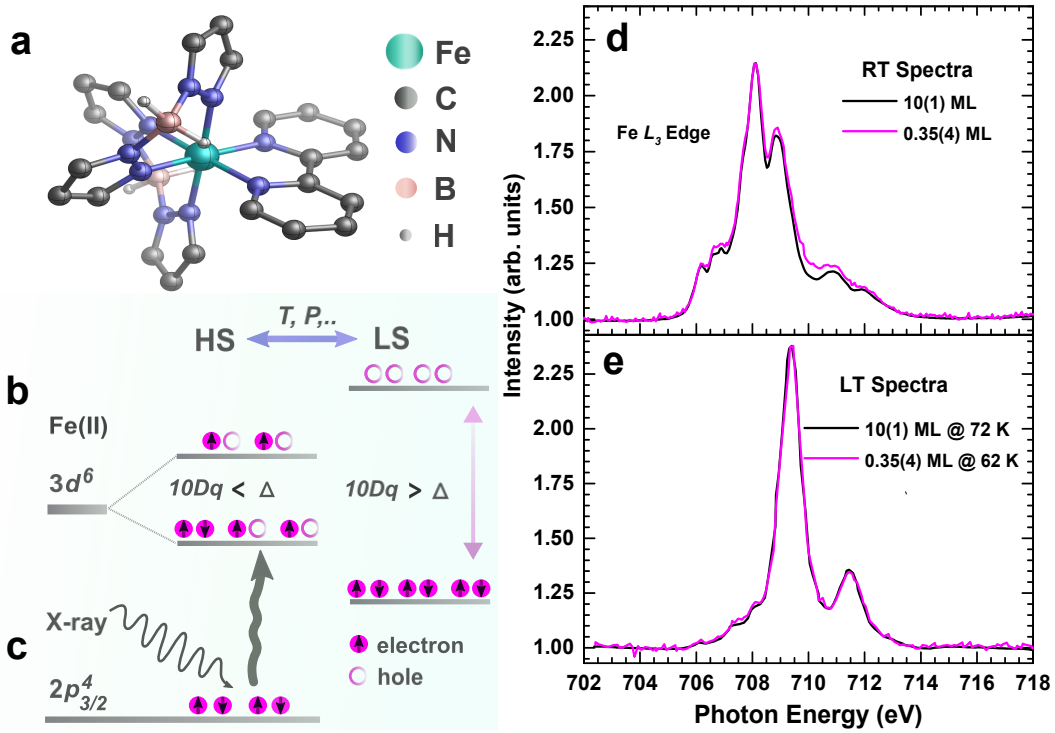

Figure 4.1: High-spin and low-spin states of spin-crossover molecules as revealed by x-ray absorption spectroscopy. (a) 3D-model of [Fe(H_2B(pz)$_2$)bipy], created from the single crystal structure data provided in Ref. 73; (b) The size of the ligand field splitting of the Fe $3d^6$ orbital into e_g and t_{2g} ($10Dq$) relative to the mean spin-pairing energy (Δ) leads to the HS or LS state; (c) Interaction of x rays with $2p^4_{3/2}$ electrons and their excitation to the $3d$ orbitals (Fe L_3 edge); (d) RT Fe L_3 absorption spectra of 10(1) ML and 0.35(4) ML of [Fe(H_2B(pz)$_2$)bipy] on HOPG (black and magenta lines, respectively), and (e) at 72 K and 62 K (black and magenta lines, respectively). The absorption intensities of the 0.35(4)-ML sample have been scaled to that of the 10(1)-ML sample. Figure adapted from ref. 65

[1] The low-temperature spectrum here refers to the pristine spectrum recorded before light illumination or the before the on-set of SOXIESST

The fraction of HS molecules (γ_{HS}) at any given temperature is estimated by fitting the corresponding spectrum to that of a linear combination of the characteristic RT and LT spectra. The low-temperature HS and LS spectra across all the coverages have similar line shapes upon scaling, though the HS spectra at RT show some minor variations.[2] The RT spectral profile comparison of all the samples is shown in Fig. 4.2 (b). For uniformity, the RT spectrum of 10(1)-ML sample is taken as the reference HS state for all the coverages, with its γ_{HS} assumed to be 0.91 in conformity with that reported for the bulk molecule [49]. The presence of a certain quantity of LS molecules at RT in thin films of [Fe(H_2B(pz)$_2$)bipy] —similar to the bulk— has also been reported elsewhere [113].

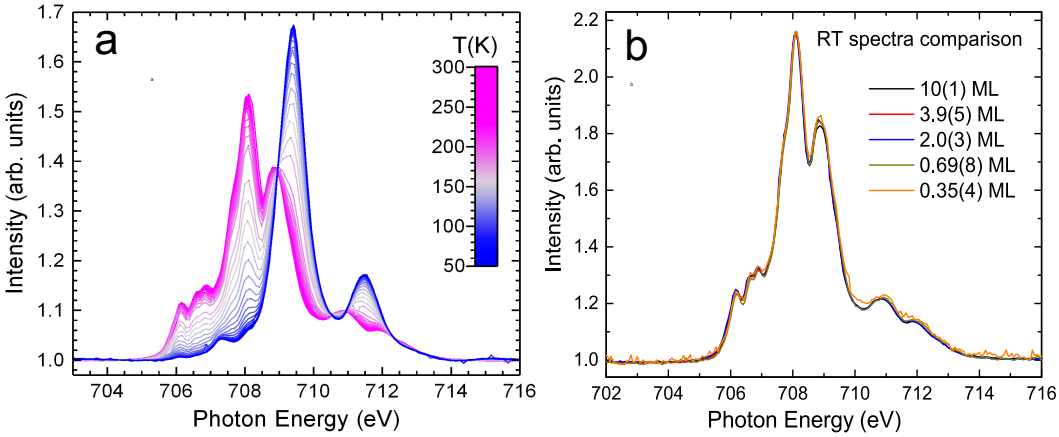

Figure 4.2: (a) Temperature-dependent Fe L_3 XA spectra of the 3.9(5)-ML sample recorded while cooling from room temperature to 50 K at a rate of 4 K·min^{-1}; (b) RT Fe L_3 spectral comparison of different coverages of [Fe(H_2B(pz)$_2$)bipy] deposited on an HOPG surface

The results of variation in γ_{HS} as a function of temperature is shown in Fig. 4.3 (a); they are characterized by a gradual to a relatively steeper spin transition when going from submonolayer to multilayer coverages, indicating an increase in cooperativity in the spin-switching processes.

Herein, the observed cooperative effects in the spin transition at all coverages are described using the classical thermodynamic model of Slichter and Drickamer (S–D model) [48]. In this model, a term $\Gamma \cdot (1 - \gamma_{HS}) \cdot \gamma_{HS}$ is introduced in the expression of Gibb's free energy, where Γ is a phenomenological interaction parameter. The macroscopic S–D model is similar to the microscopic two-level Ising-like model in the mean-field approach [114]. A model based on interacting HS and LS domains (as opposed to HS and LS states) still yields a Gibb's free energy similar to the S–D model [115]. Wavefunction *ab initio* calculations also reproduced the S–D model [46], which has been used recently to explore the possibility of an enhanced cooperativity in surface-supported 2D metal-organic frameworks [116]. At

[2]The minor variation in RT spectral profiles translates as about 3% variation in the spin-state compositions; γ_{HS} = 0.91 and 0.88 for the 10(1)- and 0.35(4)-ML samples, respectively

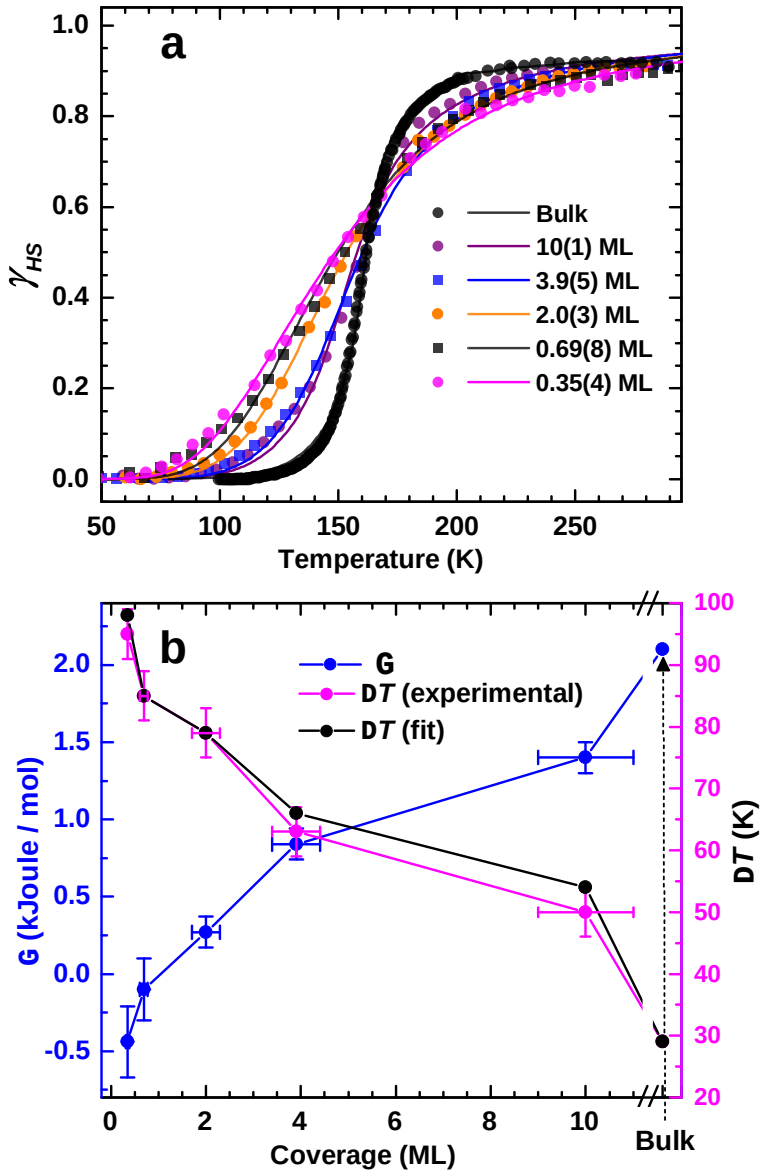

Figure 4.3: Temperature-dependent spin-crossover curves as signatures of cooperative effects. (a) Temperature-dependent spin-crossover of different coverages of [Fe(H_2B(pz)$_2$)bipy] on HOPG along with that of the bulk data; the dots represent experimental data while the solid lines are fits obtained from the Slichter-Drickamer model. (b) Dependence of the interaction parameter Γ (left-axis) and the transition width ΔT (right-axis) as a function of the molecular coverage, indicating the inverse relation between the two. The bulk material data is taken from ref. 49. Figure adapted from ref. 65

equilibrium, the S–D model leads to the implicit equation:

$$\ln\left(\frac{1-\gamma_{HS}}{\gamma_{HS}}\right) = \frac{\Delta H + \Gamma(1-2\gamma_{HS})}{RT} - \frac{\Delta S}{R} \tag{4.1}$$

where ΔH and ΔS are the differences in enthalpy and entropy, respectively, between the HS and LS states; R is the universal gas constant. The experimental input in equation (4.1) is the HS fraction γ_{HS}. Of the three fitting parameters, namely, $\Gamma, \Delta H$ and ΔS; ΔH and ΔS are related by the transition temperature $T_{1/2}$ (defined as the temperature where the population of the HS and the LS species are equal), as $\Delta H = T_{1/2} \cdot \Delta S$. If $\Gamma = 0$, then Equation (4.1) reduces to the van't Hoff's model, *i.e.,* as a system comprising of non-interacting molecules.

Table 4.1: Thermodynamic parameters. The 80-to-20% width of the temperature-dependent spin-crossover curve, the interaction parameter, the entropy and enthalpy differences ΔS and ΔH, respectively, between the HS and LS states and the transition temperature $T_{1/2}$.

Coverage (ML)	ΔT(K)		Γ (kJ mol^{-1})	ΔS^*	ΔH^*	$T_{1/2}$ (K)	
0.35(4)	95(4)[a]	98[b]	-0.44(0.23)	43(3)	6.4(4)	150(2)[a]	148.5[b]
0.69(8)	85(4)	85	-0.1(2)	44(3)	6.6(5)	153(2)	150
2.0(3)	79(4)	79	0.3(1)	44(1)	6.7(2)	154(2)	154
3.9(5)	63(4)	66	0.8(1)	44(2)	7.0(3)	162(2)	160
10(1)	50(4)	54	1.4(1)	39(2)	6.2(3)	160(2)	158
Bulk[c]	29	27	2.1	47.4	7.7	159.5	162

[*] ΔS in J mol^{-1}K^{-1}, and ΔH in kJ mol^{-1}; [a] Experimental data; [b] Determined from best fit of the model; [c] Bulk data taken from ref. 49. The uncertainties of Γ, ΔH, and ΔS given in parentheses are the standard errors as obtained from the fit of the non-linear model. The uncertainties of ΔT and $T_{1/2}$ are estimated from the scattering of the data points.

The results obtained by a fit of the experimental data by the S–D model using the method of least-square deviation are presented in Table 4.1 together with bulk data taken from Moliner *et al.* [49]. It yields a gradual evolution in cooperative spin transition in going from submonolayers to multilayers: negative interaction parameters at 0.35(4) (Γ = -0.44(0.23) kJ mol^{-1}) and 0.69(8) ML (Γ = -0.1(2) kJ mol^{-1}), positive in 2.0(3) ML (Γ = 0.3(1) kJ mol^{-1}), and further increasing with increasing coverage. In contrast, the entropy change ΔS and the enthalpy change ΔH across all coverages yield roughly constant values. The result for Γ is plotted in Figure 4.3 b as a function of coverage (blue data points, left axis). The interaction parameter Γ and the transition width ΔT, also shown in Fig. 4.2 (b), show an inverse relation. The similar values of ΔT obtained from the experimental data and the S–D model fit across all coverages (Figure 4.3 b right axis, magenta and black dots) are an indication of the suitability of the model in tracing the evolution of cooperativity in the

spin-transition processes in ultrathin films.

The build-up of cooperativity in molecular layers of only a few monolayers thickness indicates the presence of intermolecular interactions across the molecular layers. While a two-dimensional arrangement such as submonolayer islands exhibits an apparent antagonistic behavior arising either from interactions that favour unlike-spin states or from a distribution in the energy barriers between the two spin states, clear signs of cooperative spin switching are observed starting already from the second layer. The further increase in the degree of cooperativity with increasing thickness could be related to the higher coordination of molecules in the inner layers compared to the surface layers, the reduction in the relative amount of surface or interface molecules, and/or the reduced importance of molecules in direct contact with the substrate.

It is interesting to compare the results presented here with spin-crossover nanoparticles, although the direct external environments of SCMs on the surface and those of nanoparticles are different in that the nanoparticles are always coated with a stabilizer which acts as a rigid matrix. Nevertheless, spin-crossover nanoparticles are also found to exhibit a gradual temperature-dependent spin-transition like the one observed here in the case of ultra-thin films, but with the transition temperatures being proportional to the particles' sizes. However, at particle sizes of less than 10 nm, hysteretic behaviour (memory effects) appears — which have been attributed to an increase in the lattice stiffness leading to greater cooperative effects [117]. The presence (or absence) of hysteretic behaviour in these ultra-thin films of [Fe(H_2B(pz)$_2$)bipy] is not known, as the spin-state change in the opposite direction, *i.e.*, temperature ramp-up from low- to room-temperature, has not been measured. It is worth noting that a small hysteresis of about 4 K has been reported in a relatively thick vacuum-deposited film (355 nm) of [Fe(H_2B(pz)$_2$)bipy] [113], despite the absence of such a behaviour in the bulk [49, 73]. To the best of our knowledge, however, for vacuum-deposited films with thickness in the range of our samples — maximum thickness of about 12 nm — the presence of hysteresis has never been reported.

4.2.1 Details of the S–D model fit

The variations in the mean squared deviations (m.s.d.) between the fits of the Slichter–Drickamer model and the experimental data with respect to a variation in one of the parameters — the interaction parameter Γ, the enthalpy change ΔH, and the entropy change ΔS — while fitting the other two are shown in Fig. 4.4. The minima of m.s.d. of the ultra-thin films are similar to that of the bulk sample, or lower in the case of the 2.0(3)- and 3.9(5)-ML samples, indicating the suitability of the model in describing the thermally-induced spin crossover in ultra-thin films.

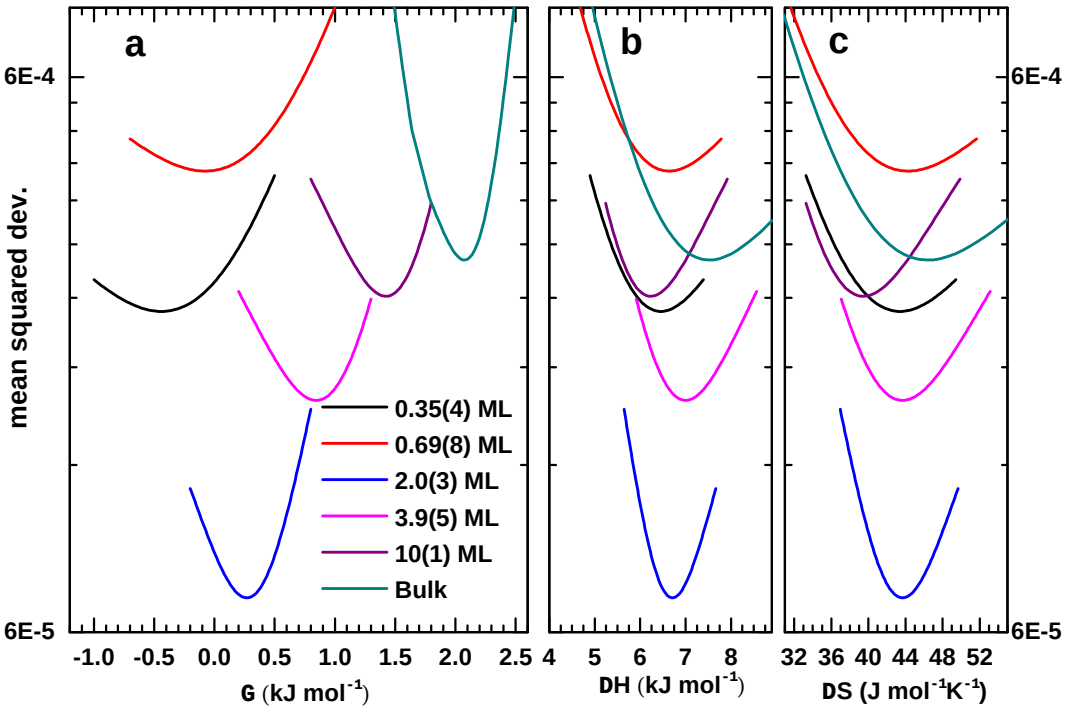

Figure 4.4: Dependence of the mean squared deviations on the variation in one of the parameters of the Slichter–Drickamer model while fitting the other two, for the samples ranging from 0.35(4) ML to the bulk; (a) Γ, (b) ΔH, and (c) ΔS. The experimental data for obtaining the bulk fits is taken from ref. 49

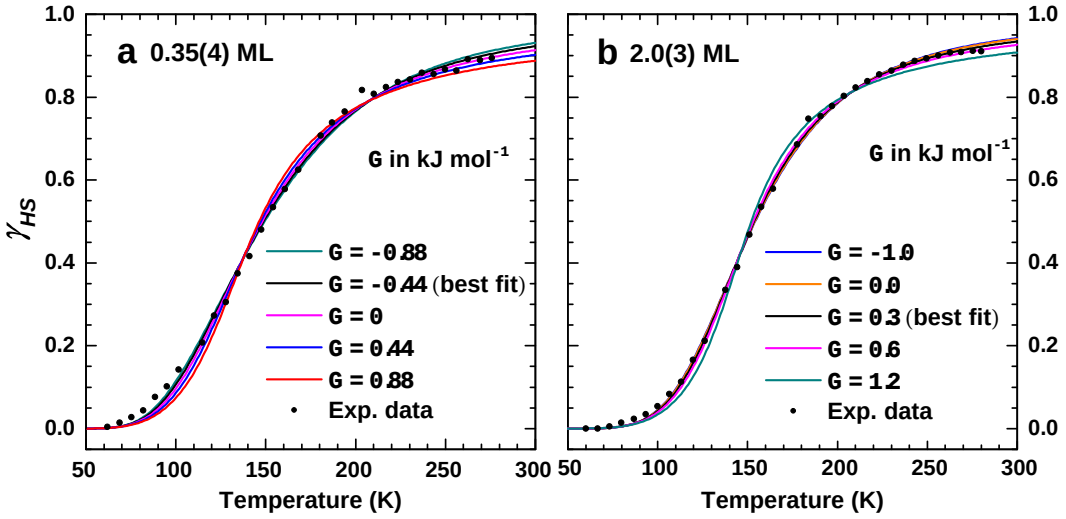

Figure 4.5: Fitting curves for different fixed values of Γ around the best-fit values in the case of 0.35(4)-ML (left panel) and 2.0(3)-ML (right panel) samples. Black dots are the corresponding experimental data.

Fig. 4.5 shows a comparison of the fits obtained by keeping the interaction parameter Γ in the S-D model fixed at certain values (fitting only ΔS and ΔH)- for the case of the 0.35(4)- and 2.0(3)-ML samples. The resulting best fit parameters for ΔS and ΔH are listed in Table 4.2. The effect of a higher (lower) value of Γ can be partly compensated by lower (higher) values of ΔH and ΔS. However, the shape of the temperature-dependent spin transition curve does not stay the same as well as the HS content at 300 K. There are clear minima in the mean squared deviation of the fits as a function of Γ, as shown in Fig. 4.4.

Table 4.2: Values of the fit parameters of Fig. 4.5.

Coverage (ML)	Γ*	ΔH	ΔS
0.35(4)	-0.88	7.2(1)	48.1(8)
	-0.44	6.4(4)	43(3)
	0.0	5.7(1)	38.7(7)
	0.44	5.0(1)	33.9(7)
	0.88	4.3(1)	29.1(9)
2.0(3)	-1.0	9.3(2)	60(1)
	0.0	7.2(1)	47.1(5)
	0.3	6.6(1)	43.4(4)
	0.6	6.0(1)	39.5(4)
	1.2	4.9(1)	32(1)

* Γ and ΔH in kJ mol^{-1}; ΔS in J mol^{-1}K^{-1}

4.2.2 Spin-crossover theory without cooperative effects

To further underscore the evolution of cooperative effects with increasing thickness in the present samples, it is imperative to check if the spin-crossover curves as presented in Fig. 4.3 (a) can be explained by a model with no cooperative effects. To show this, in Fig. 4.6 are plotted the calculated thermal SCO curves at certain values of γ_{HS} for different values of ΔH and ΔS, keeping the transition temperature $T_{1/2} = \Delta H/\Delta S$ constant at 155 K. The curves have been calculated assuming no cooperativity, *i.e.*, $\Gamma = 0$, which reduces the Slichter-Drickamer model to the van't Hoff's model.

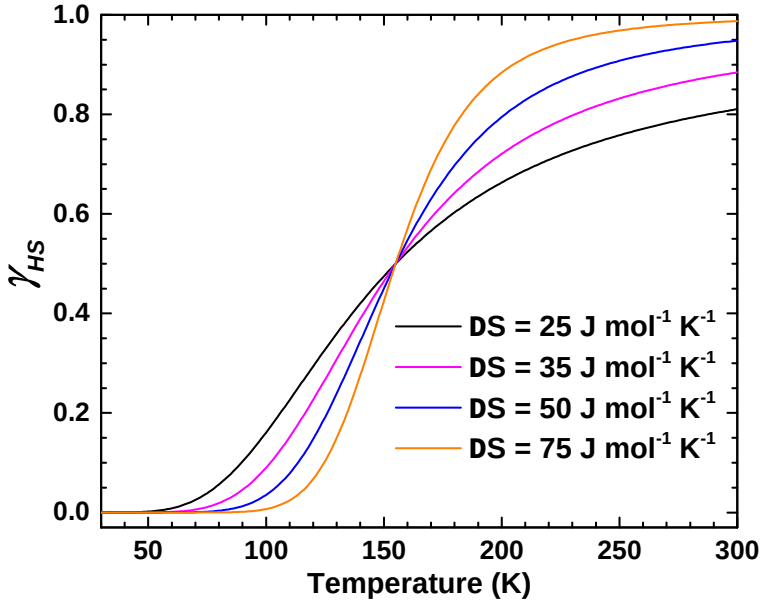

Figure 4.6: Calculated relative amount of HS molecules as a function of temperature, assuming no cooperativity ($\Gamma = 0$) and $T_{1/2} = \Delta H/\Delta S = 155$ K

Different values of ΔH and ΔS lead to different widths of the thermal spin-state transition, but at the same time significantly influence the amount of HS molecules γ_{HS} at room temperature. This is in contradiction to the experimental result shown in Fig. 4.2 (b), where the RT spectral profiles are similar across different coverages, indicating a uniform composition in the spin fractions — although the transition widths changed significantly across the different coverages. Hence, cooperative effects have to be taken into account for explaining the thermal-induced spin-crossover phenomenon in the present samples.

4.3 Light-induced excited spin-state trapping

SCMs can be converted from the ground LS state to a metastable HS state at low temperatures by excitation with light of suitable wavelengths, which came to be known as light-induced excited spin-state trapping (LIESST). The LIESST phe-

nomenon was discovered for the first time by Decurtins *et al.* [50]. Since then, light has become one of the most widely used stimuli for exploring spin-crossover phenomena. The process of LIESST has been well investigated and well understood as being due to inter-system crossing — electrons in the ground LS state are excited to the metal-to-ligand charge-transfer states (MLCT), and then undergo fast relaxation back to either the LS or the HS state — as schematically depicted in Fig. 4.7 (a). The various steps involved in the LIESST process have been revealed in vivid details with ultrafast optical and x-ray spectroscopies [107, 108].

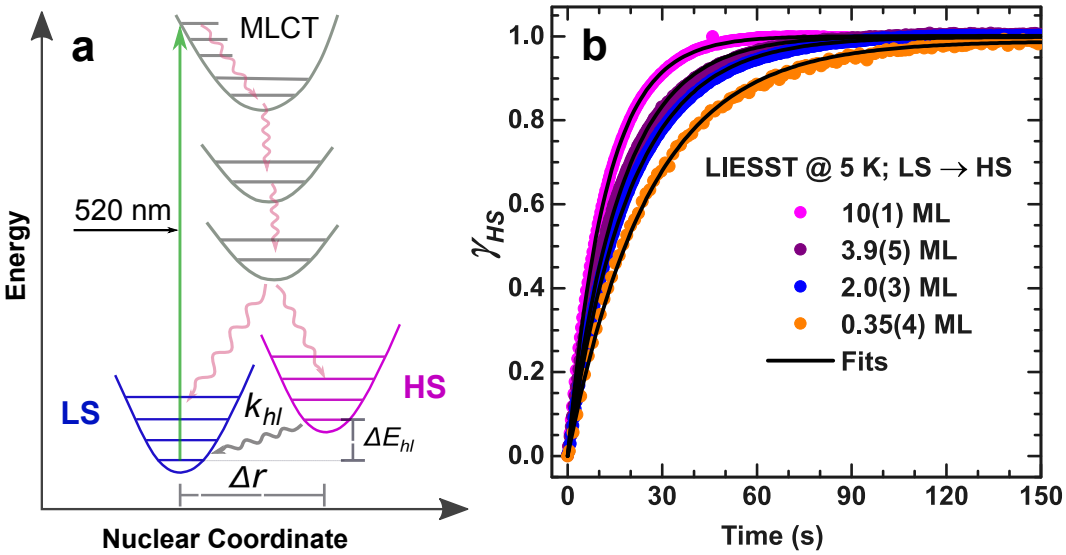

Figure 4.7: Light-induced excited spin-state trapping (LIESST). (a) Schematic representation of the light-induced LS → HS state transition — the excitation of electrons from the LS state to the MLCT (metal-to-ligand charge transfer) states, and subsequent relaxation to the HS state via intermediate states — and the eventual decay of HS to the LS state with a rate constant k_{hl}; (b) Light-induced LS → HS state transition at 5 K for the different samples of [Fe(H_2B(pz)$_2$)bipy] deposited on HOPG

4.3.1 LIESST as independent of cooperative effects

The light-induced HS → LS conversions are investigated for the different coverages of [Fe(H_2B(pz)$_2$)bipy] deposited on an HOPG surface, by using light of wavelength $\lambda = 520$ nm at 5 K. The results are shown in Figure 4.7 b. The growth of the HS state population upon illumination is determined by recording a time scan of the absorption signal with the x-ray energy fixed at 708.1 eV.[3] The Fe L_3 edge spectra recorded before and after such a time-scan are shown in Fig. 4.8; these are used to ascertain the conversion of the spin states. The spectral profiles are consistently identical across all coverages before and after illumination. The spectra recorded before il-

[3]The intensity of the absorption signal at 708.1 eV above the background signal is proportional to the HS content

lumination are taken as representing the LS state (S = 0) and after illumination as representing the HS state (S = 2). The spectral line shapes of the HS and LS states are very similar to the ones obtained from multiplet calculations [31, 70].

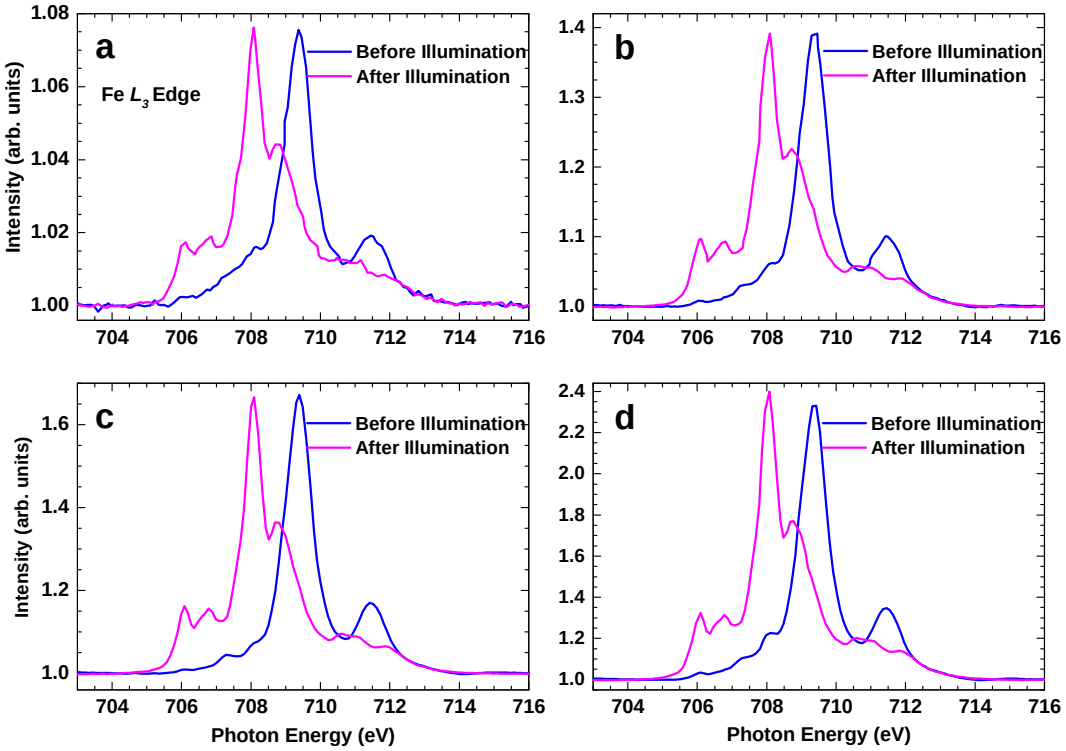

Figure 4.8: Fe L_3 XA spectra taken before (blue) and after (magenta) illumination for the LIESST experiments at 5 K given in Fig. 4.7 (b). (a) 0.35(4) ML; (b) 2.0(3) ML; (c) 3.9(5) ML, and (d) 10(1) ML

The HS fraction γ_{HS} as a function of illumination time is obtained by normalization of the recorded time-scan signal between 0 (the LS state) and 1 (the HS state). Fitting the LS→HS transition with a single exponential function yields rate constants of 0.065(1), 0.0501(1), 0.0583(2), and 0.0823(1) s^{-1} for 0.35(4), 2.0(3), 3.9(5), and 10(1) ML, respectively. However, these rate constants consist of light- as well as x-ray contributions; the latter arising from the x-ray exposure during the time-scan. One can incorporate both the light- and x-ray-induced spin transitions in a simple rate equation of the form:

$$\frac{d\gamma_{HS}}{dt} = (k_L + k_S)(1 - \gamma_{HS}) - k_{rS}\gamma_{HS} \tag{4.2}$$

where k_L is the rate constant for the light-induced LS→HS state transitions; k_S and k_{rS} are the rate constants due to SOXIESST (x-ray-induced LS→HS state transitions) and reverse-SOXIESST (x-ray-induced HS→LS state transitions), respectively.

The light and x-ray components can be separated by making use of the val-

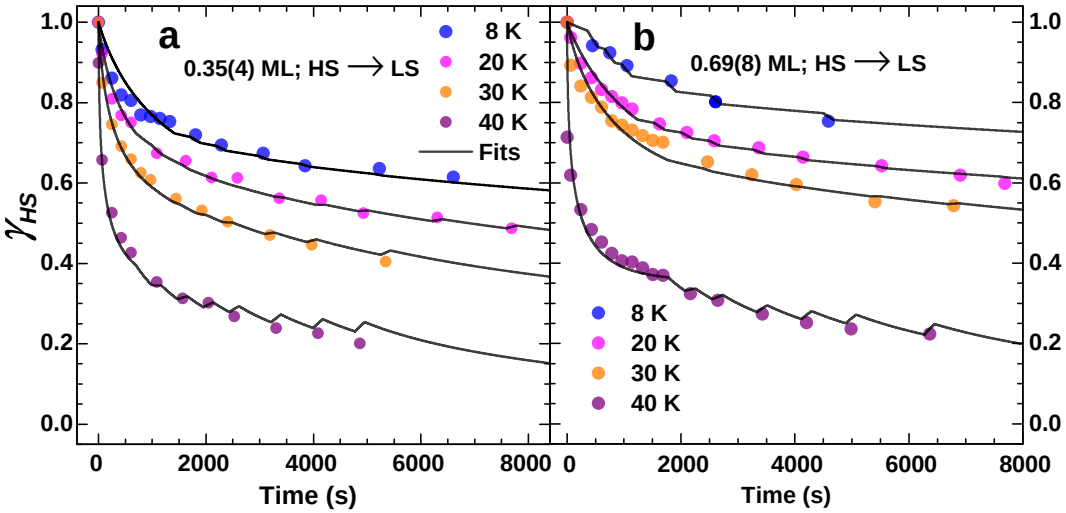

Figure 4.9: The HS→LS relaxation at 8, 20, 30, and 40 K of (a) 0.35(4)-ML sample, and (b) 0.69(8)-ML sample (dots). The solid lines are the result of a simultaneous fit to Equation 4.3 together with the x-ray-induced rates. The step-like features at the data points are due to the contributions to the rate constants from x rays

ues of k_S and k_{rS} reported in the same system and recorded with the same photon flux density — 0.8 ML of [Fe(H_2B(pz)$_2$)bipy] on HOPG at 5 K — which are $3.50(3) \times 10^{-4}\,s^{-1}$ and $2.3(1) \times 10^{-4}\,s^{-1}$, respectively [67]. The rate constants solely from LIESST are then estimated as 0.0369(1), 0.0505(1), 0.0589(2), and 0.0827(1) s^{-1} for 0.35(4), 2.0(3), 3.9(5), and 10(1) ML, respectively. With the green LED photon flux density of $4.2(8) \times 10^{14}$ photons $s^{-1}mm^{-2}$, the corresponding effective cross sections are estimated as 0.009(2), 0.012(2), 0.014(3), and 0.019(4) Å^2, respectively. Since each of the curves can be fitted by a mono-exponential function albeit with different rate constants, it is concluded that the light-induced LS→HS transition arises from an individual molecule–photon interactions without any role of cooperative effects. This result is in agreement with LIESST in bulk SCMs, where it is also found to be a single–molecule phenomenon [77]. The observed efficient switching of the spin states with light in these SCMs in contact with an HOPG surface can be exploited for applications in optical memory and display elements [81].

4.3.2 Stability of the light-induced HS state

Fig. 4.9 shows the results of HS→LS relaxation measurements of 0.35(4)- and 0.69(8)-ML samples at 8, 20, 30, and 40 K. The measurements are done by firstly switching the sample to the HS state by green-LED illumination. With the illumination off, the subsequent spin relaxation is traced from Fe L_3 spectra recorded as a function of time. The low-temperature HS→LS relaxation process is characterized by an initial fast relaxation and then slows down with time, leading to a stretched exponential.

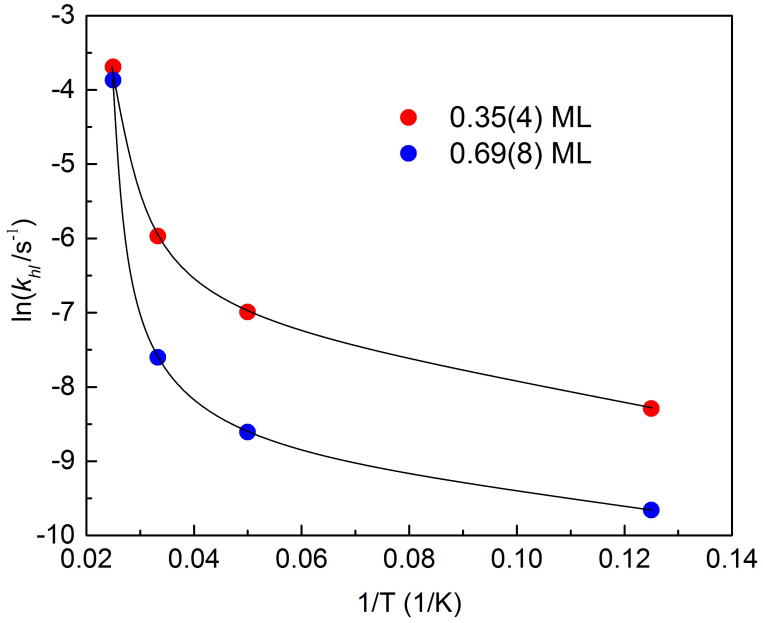

Figure 4.10: Comparison of the HS→LS relaxation rate constants k_{hl} as a function of temperature, of 0.35(4) ML (red dots) and 0.69(8) ML (blue dots) of [Fe(H_2B(pz)$_2$)bipy] deposited on an HOPG surface. solid lines are guides to the eyes

This is in sharp contrast to the bulk, where the HS state is rather stable in the temperature range considered here, and only in the thermally-activated regime (> 40 K), the spin relaxation become pronounced and exhibits sigmoidal-type characteristics [49]. The HS→LS relaxation observed on the surface can be modelled with a phenomenological equation involving a negative interaction parameter α:

$$\frac{\partial \gamma_{HS}}{\partial t} = -k_{hl}\,\gamma_{HS}\exp[\alpha(1-\gamma_{HS})] \tag{4.3}$$

where k_{hl} denotes the HS→LS relaxation rate constant. Equation (4.3) is similar to the phenomenological model introduced by Hauser to explain the HS→LS relaxation in the bulk SCMs, but with α replaced by α/T in the thermally activated regime so as to account for the sigmoidal-type HS→LS relaxation behaviour [54]. For an accurate modeling of the HS→LS relaxation, the x-ray-induced spin transitions occurring during the data acquisition as given in Equation 4.2, namely, $k_S \cdot (1-\gamma_{HS})$ for LS→HS and $k_{rS}\cdot\gamma_{HS}$ for HS→LS transitions have to be included in Equation (4.3) [67]. A simultaneous fit of Equation (4.3) to the spin relaxation measurements at all temperatures including the SOXIESST (and the reverse-SOXIESST) terms yields the value of the interaction parameter α to be $-6.3(3)$ and $-6.4(3)$ for the 0.35(4)- and 0.69(8)-ML sample, respectively. A comparison of $\ln(k_{hl}(T))$ for both coverages is given in Figure 4.10. In comparison to the 0.69(8)-ML sample, the metastable HS state of the 0.35(4)-ML sample decays much more rapidly to the ground state (LS state) in the temperature range between 8 and 30 K. However, at

40 K, the relaxation rates become similar: $0.025(5)$ and $0.021(7)\,s^{-1}$ for the 0.35(4) and 0.69(8)-ML sample, respectively. In the bulk relaxation data provided in ref. 49, the relaxation rate at 42 K is about three orders of magnitude lower than that of the submonolayer samples at 40 K.

These differences in the decay rates might arise either from enhanced tunnelling rates or a reduction in the energy barriers between the HS and LS wells; or a combination of both, in the submonolayer samples as compared to the bulk (the quantum tunneling rate is related to the characteristic vibrational frequency of the [FeN6] core [54]). It should be noted regarding the incorporation of x-ray-induced corrections as applied to the HS→LS relaxation of Fig. 4.9 that, the rates are assumed to be independent of temperature; the direction of the steps depends on the amount of the HS or the LS fraction at the instant of measurements; at high HS contents, the x-ray-induced effect is dominated by reverse-SOXIESST resulting in the downward steps, while the reverse is true in the case of high LS contents (SOXIESST domination and upward steps). The height of the steps depends on the "distance" to the SOXIESST saturation spin state of 60% HS [67].

4.4 Relating Γ and α

From the foregoing analyses, one can see that the thermal-induced spin transition and the metastable HS relaxation to the LS ground state at low temperatures are characterized by the interaction parameters Γ and α respectively, with both assuming negative values. For SCMs in the bulk, α and Γ are related by a constant, $\alpha = p\Gamma$ [54], as described in Chapter 1 Section 1.1.4. Using the values of the parameters given in ref. 49, p is estimated to be $1.3 \times 10^{-3}\,J^{-1}$ mol for [Fe($H_2B(pz)_2$)bipy] in the bulk. For the 0.35(4)-ML sample and assuming that the same relation still holds (given the negative values of both α and Γ), a value of $p = 1.4(9) \times 10^{-2} J^{-1}$ mol is obtained. The higher value of p by about an order of magnitude in the 0.35(4)-ML sample as compared to the bulk might be attributed to a reduced characteristic vibrational frequency of the [FeN_6] core in the former, possibly due to molecule–substrate interactions.

Alternatively, a distribution in the energy barriers between HS and LS states — arising from disorder or conformational flexibility of the ligand — can also result in a stretched exponential HS→LS relaxation, as reported in the case of some bulk SCMs exhibiting strong cooperativity in the temperature-induced spin transition, but nevertheless displaying a stretched-exponential spin relaxation due to such factors [55, 118]. It is therefore not clear whether the stretched exponential decay results exclusively from an antagonistic (or anticooperative) spin transition. Regardless of the mechanism, it should be mentioned that this is the first report on the HS→LS relaxation of SCMs on a surface exhibiting a stretched exponential decay.

"Scientific views end in awe and mystery, lost at the edge in uncertainty, but they appear to be so deep and so impressive that the theory that it is all arranged as a stage for God to watch man's struggle for good and evil seems inadequate."

— Richard P. Feynman

5

SPIN CROSSOVER ON SURFACES: THE ROLE OF METHYLS

This chapter concerns with the on-surface engineering of spin-crossover behaviour on HOPG, Au(111) and Bi(111) by modifying the ligands of the two closely-related molecules [Fe(H_2B(pz)$_2$)phen] and [Fe(H_2B(pz)$_2$)bipy]. The complex [Fe(H_2B(pz)$_2$)phen] is reported to undergo decomposition into its components [Fe(H_2B(pz)$_2$)] and phenanthroline upon adsorption on a gold surface [72]. We strategize to prevent the decomposition by adding four methyl groups [me_4] to the phenanthroline ligand. The new compound [Fe(H_2B(pz)$_2$)$_2$(phen$-me_4$)] exhibits spin-crossover behaviour in the bulk and in thin films deposited on a quartz substrate — similar to the parent molecule.[1] *The stability and spin-crossover behaviour on a gold surface upon thermal evaporation was investigated using both XAS and STM; the compound is found decomposed into its component parts — [phen$-Me_4$] and [Fe(H_2B(pz)$_2$)] — similar to the behaviour of the parent molecule. The two complexes when deposited on a Bi surface exhibit identical spin-crossover behaviour — the molecules stay intact on the surface, but the spin-state bistability is retained only by less than half of the molecules, with the rest being trapped in the HS state. Yet, their spin-crossover behaviour on an HOPG surface couldn't be starker: While the parent molecule exhibits both thermal- and light-induced spin-crossover, the daughter molecule is trapped in the HS state, without undergoing any observable change in the chemical structure. This intriguing behaviour is further explored by measuring the orientation of the molecules on the surfaces, using XAS.*

Part of the results from this chapter have been published in:
ACS Nano **9**, (2015) 8960 &
J. Mater. Chem. C **3**, (2015) 7870 &
J. Phys. Chem. C **121**, (2017) 1210.

[1] [Fe(H_2B(pz)$_2$)phen] and [Fe(H_2B(pz)$_2$)bipy] will be referred to as the parent molecules; any compound or compounds derived from the parent molecules will be referred to as the daughter molecules

5.1 Engineering spin-crossover behaviour through ligand modification

It is known that the nature of ligands attached to the Fe(II)-ion centres of SCMs in the bulk can greatly alter/affect the mode of spin transition. This is because spin-crossover phenomena in the bulk are driven by cooperative effects, which is generally attributed to elastic interactions between the spin-transiting Fe(II)-ion centres due to volume increase and decrease accompanying the spin transitions. What is of interest to us within our collaborative work is to see if adding some other organic compounds such as methyl groups to the phenanthroline ligand of [Fe(H_2B(pz)$_2$)phen] and bipyridine of [Fe(H_2B(pz)$_2$)bipy] can weaken the molecule–substrate interaction, thereby preserving the integrity of the compound(s) when deposited on a gold substrate [72]. It would also be interesting to study the behaviour of these modified molecules on an HOPG surface to see what the ligand modification had on the spin-crossover behaviour.

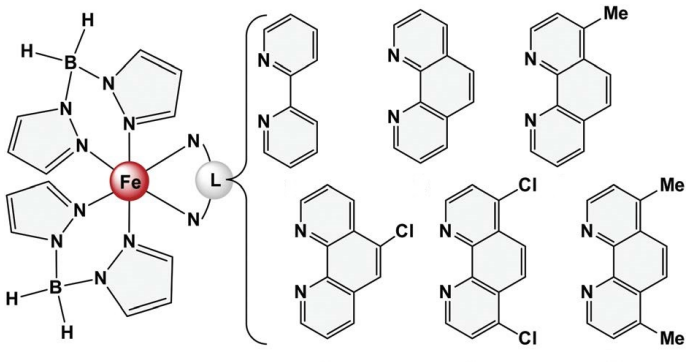

Figure 5.1: Parents and (some of) the daughter molecules. Figure adapted from ref. 63

Towards this end, our collaborators Naggert *et al.* from Christian-Albrecht Universität Kiel synthesized a series of molecules, in which the phenanthroline and the bipyridine ligand of the complex [Fe(H_2B(pz)$_2$)phen] and [Fe(H_2B(pz)$_2$)bipy], respectively, is functionalized with methyl, dimethyl, chloro, and dichloro groups [63], as shown in Fig. 5.1; as well as with tetra-methyls (not shown in the Figure). The temperature- and light-induced spin-crossover behaviour of the compounds shown in Fig. 5.1 in the bulk and in the thin film — including a detailed analyses of their crystal structures — can be found in ref. 63. In the context of this thesis — as is also mentioned in the preceding paragraphs — the SCO behaviour of the molecule functionalized with four methyl groups, [Fe(H_2B(pz)$_2$)$_2$(phen−me$_4$)], starting from the bulk behaviour down to the submonolayer coverage deposited on Au(111), Bi(111) and on HOPG substrates, as well as bilayer on HOPG is investigated in detail. Also, the temperature-induced spin-crossover behaviour of a submonolayer of [Fe(H_2B(pz)$_2$)$_2$(phen−me$_2$)] deposited on an HOPG surface is also investigated and its behaviour compared to that of the former. For

convenience — and wherever necessary — the compounds [Fe(H_2B(pz)$_2$)phen], [Fe(H_2B(pz)$_2$)$_2$(phen−me$_2$)], and [Fe(H_2B(pz)$_2$)$_2$(phen−me$_4$)] are sometimes labelled as **1**, **2**, and **3**, respectively. HOPG substrate is of particular interest as both the two closely-related molecules [Fe(H_2B(pz)$_2$)phen] and [Fe(H_2B(pz)$_2$)bipy] are found to preserve their spin-crossover behaviour even on direct contact with it [31, 65]. Hence, the spin-crossover behaviour of the methylated compounds of both the parent molecules are further investigated and compared on an HOPG surface.

5.2 [Fe(H_2B(pz)$_2$)phen] and its derivatives on HOPG

The complex [Fe(H_2B(pz)$_2$)phen] is one of the more widely investigated SCM on a surface, as it is one of the few molecules stable against thermal evaporation. In the bulk material, the spin-crossover behaviour with temperature, light and pressure has been reported [49, 73, 96]. In particular, the complex in the bulk exhibits a small hysteresis of about 2.3 K in the temperature-dependent spin-transition curve — indicating cooperativity in the spin transition processes [49]. On a gold surface, [Fe(H_2B(pz)$_2$)phen] is found to undergo fragmentation into the high-spin [Fe(H_2B(pz)$_2$)] and the phenanthroline ligand, resulting in the loss of spin-crossover behaviour. However, the molecules once decoupled from the surface — starting from the bilayer — retain their spin-state bistability [72]. In fact, the first observation of electron-induced excited spin-state trapping (ELIESST) with an STM tip was made in a double layer of [Fe(H_2B(pz)$_2$)phen] on a gold surface [68].

In contrast, the complex exhibits thermal- as well as light-induced spin-crossover even upon direct contact with an HOPG surface [31]. The Fe L_3–edge spectral pattern at 300 K, and before and after illumination with a green LED at 6 K is shown in Fig. 5.2 (a), which bears all the hallmarks of a 'clean' temperature- and light-induced spin-state transition, similar to what had already been described in the case of [Fe(H_2B(pz)$_2$)bipy] on the same substrate in the preceding Chapters. Fig. 5.2 (b) shows the spin-state variation as the temperature is decreased from 300 K down to 6 K; the spin-state switching from the HS state (S = 2) to the LS state (S = 0) is complete at about 80 K. At lower temperatures (below 50 K), there is a gradual buildup of the HS state due to the x-ray induced effects (SOXIESST). The temperature-induced spin transition is rather gradual, and can be modelled as a system of non-interacting molecules as opposed to the bulk system that exhibits cooperative spin transition [73].

The light-induced LS-to-HS conversion at 5 K — which was carried out by illuminating the sample with light of wavelength 520 nm — is also very efficient, with a time constant of 20.4(7) s. Starting from the light-induced metastable HS state at 6 K, the system can be converted to the LS state by raising the sample temperature to about 70 K, showing the reversibility in the spin transitions (Fig. 5.2 (green dots)). The efficient light-induced switching observed in this system holds great promise

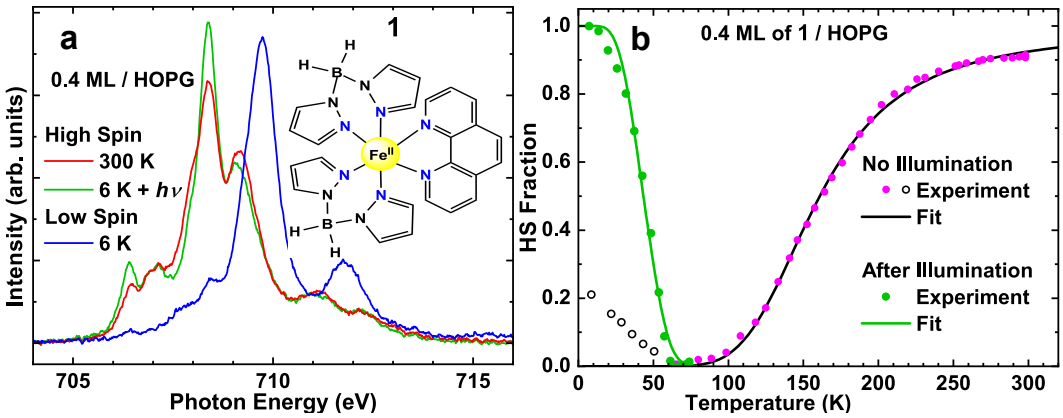

Figure 5.2: 0.4 ML of $[Fe(H_2B(pz)_2)phen]$ deposited on an HOPG surface. (a) Fe L_3 spectra at 300 K (red coloured line), before and after illumination with a green LED at 6 K (blue and green lines, respectively) as a measure of the spin-state of the molecule. (b) Fraction of HS molecules as a function of temperature during cooling the sample without illumination (magenta dots); the green dots indicate temperature-variation of the HS state — starting from the light-induced HS at 6 K, and with light illumination ON — as the sample temperature is ramp-up to about 90 K. The light illumination-free temperature-induced spin transition is fitted with a model based on non-interacting molecules. The relaxation of the light-induced HS state is fitted with Arrhenius law. Inset: 2D chemical structure of $[Fe(H_2B(pz)_2)phen]$. Figure adapted from ref. 31

for application in optical storage devices. In the existing data storage devices, information — encoded by magnetic states — is processed *via* magnetic fields, resulting in energy dissipation. Realizing SCM–based data storage devices where information can be processed by light is expected to drastically reduce energy consumption.

The two daughter molecules $[Fe(H_2B(pz)_2)_2(phen-me_2)]$ and $[Fe(H_2B(pz)_2)_2(phen-me_4)]$, of ∼0.4 ML each on an HOPG surface, showed sharply contrasting spin-crossover behaviour with regard to the parent molecule; while the former exhibit only a partial spin crossover — which can be directly inferred from the presence of the high-spin-state peak at ∼708.4 eV of the Fe L_3-edge spectrum recorded at 20 K, shown in Fig. 5.3 (a) (blue line) — the latter is trapped in the HS state at all temperatures, which is inferred directly from the similar spectral patterns of the Fe L_3-edge spectra recorded at three different temperatures: 300, 150 and 30 K, shown in Fig. 5.3 (b). The role of the HOPG surface in locking the spin state of $[Fe(H_2B(pz)_2)_2(phen-me_4)]$ is further explored in a 2.2-ML sample, as shown in Fig. 5.3 (c). There is a noticeable reduction in the intensity of high-spin-state peak at ∼708.4 eV, with a concomitant increment in the intensity of the low-spin-state peak at ∼709.5 eV of the Fe L_3-edge spectrum recorded at 10 K, relative to that recorded at 300 K.

This is an indication that $[Fe(H_2B(pz)_2)_2(phen-me_4)]$ molecules, once decou-

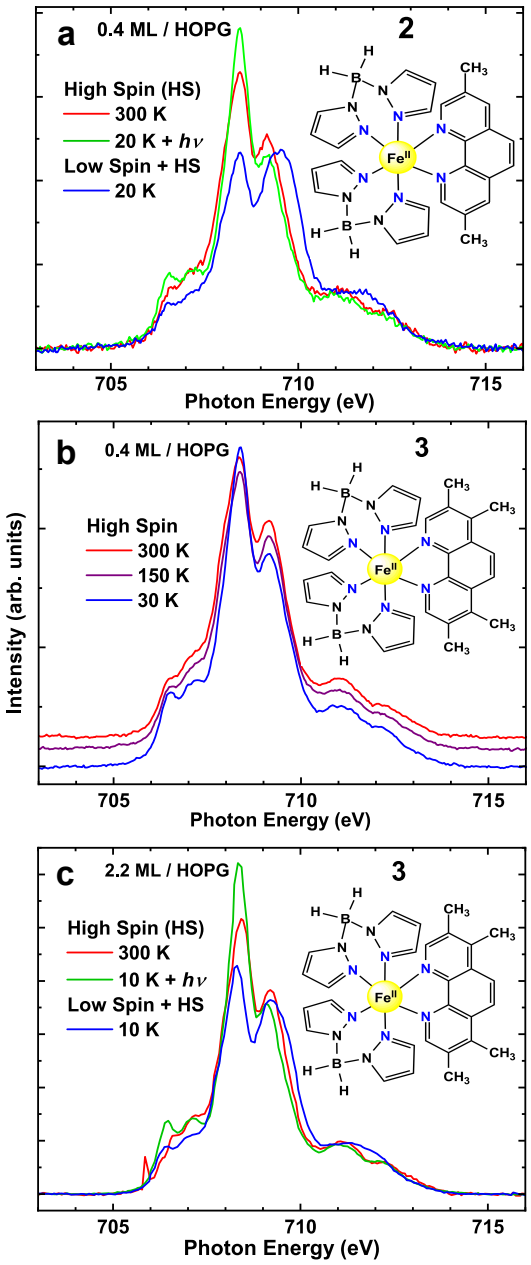

Figure 5.3: (a) Fe L_3 spectra at 300 K (red coloured line), before and after illumination with a green LED at 20 K (blue and green lines, respectively) of 0.4 ML of [Fe(H$_2$B(pz)$_2$)$_2$(phen−me$_2$)] deposited on an HOPG surface; (b) Fe L_3 spectra of 0.4 ML of [Fe(H$_2$B(pz)$_2$)$_2$(phen−me$_4$)] deposited on an HOPG surface, recorded at 300, 150 and 30 K; and (c) Fe L_3 spectra of ∼2.2 ML of [Fe(H$_2$B(pz)$_2$)$_2$(phen−me$_4$)] deposited on an HOPG surface recorded at 300 K (red line), before and after illumination with a green LED at 10 K (blue and green lines, respectively)

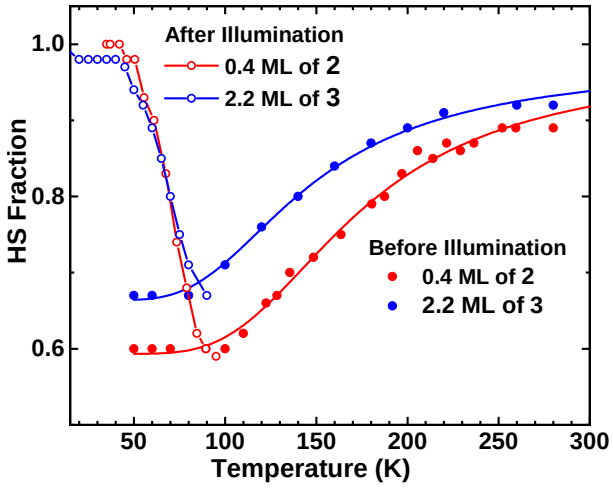

Figure 5.4: Temperature dependent spin-state compositions of 0.4 ML of $[Fe(H_2B(pz)_2)_2(phen-me_2)]$ (**2**, red solid circles) and 2.2 ML $[Fe(H_2B(pz)_2)_2(phen-me_4)]$ (**3**, blue solid circles), both deposited on an HOPG substrate. Solid lines are guides to the eyes. Open circles represent the thermally-activated spin-state switching in the low-temperature range (20—100 K), starting from the light-induced HS state at 20 K and raising the temperature to 100 K

pled from the HOPG surface, undergo spin transition. But not all of the molecules lying at the bilayer or higher exhibit spin transition. One can estimate the spin-state composition of the daughter molecules at any given temperature by using the Fe L_3-edge spectra of the parent molecule $[Fe(H_2B(pz)_2)phen]$ recorded at 300 K and 6 K (before green LED illumination) — shown in Fig.5.2 (a) — as reference HS and LS state spectrum, respectively; any given spectrum of the daughter molecules can be reproduced by linearly combining the reference spectra. Following this procedure, the spin-state compositions of both the daughter molecules are estimated at different temperatures and are shown in Fig. 5.4. For the 0.4-ML $[Fe(H_2B(pz)_2)_2(phen-me_2)]$ sample, a minimum HS content of 60(5)% is obtained at around 100 K on lowering the temperature from the maximum HS state of about 90(5)% at 300 K, implying that about 30(5)% of HS molecules are switched to the LS state with temperature. Interestingly, all the LS molecules of about 40(5)% got switched to the HS state on illuminating with green LED at 20 K — and can be converted back to the ground LS state on raising the temperature to 100 K.

For the 2.2-ML sample of $[Fe(H_2B(pz)_2)_2(phen-me_4)]$, a minimum HS content of about 67(5)% is obtained at around 82 K on lowering the temperature from the maximum HS content of about 92(5)% at 300 K. The question is: How much of the molecules decoupled from the substrate — *i.e.*, lying at the bilayer or higher — undergo spin transition from the HS state to the LS state with temperature? This can, of course, be answered by simple arithmetic; the 67(5)% HS content can be broken down into 100% HS contribution coming from the first monolayer and 40(5)% HS contribution coming from the remaining 1.2 monolayers. Thus, 52(5)%

of HS molecules decoupled from the HOPG surface undergo transition to the LS state with temperature (8(5)% of the 60(5)% LS molecules at 100 K are already in the LS state at 300 K). On illumination with a green LED at 10 K, almost all the LS molecules are switched to the HS state, which subsequently can be converted back to the ground LS state by raising the sample temperature to 100 K.

What is of interest, then, is the reason for the loss of spin-crossover behaviour of [Fe(H$_2$B(pz)$_2$)$_2$(phen−me$_4$)] molecules upon direct contact with the HOPG surface. It could be molecular fragmentation, molecular distortion, or enhanced molecule-substrate interaction *via* methyl groups. From the N *K*-edge of both [Fe(H$_2$B(pz)$_2$)phen] and [Fe(H$_2$B(pz)$_2$)$_2$(phen−me$_4$)] molecules measured at different angles between the HOPG surface normal and the electric field polarization vector of the x rays — presented in Section 5.4 — fragmentation or distortion of the molecule from the usual octahedral symmetry that characterized SCMs, can be ruled out. In fact, the daughter molecule [Fe(H$_2$B(pz)$_2$)$_2$(phen−me$_4$)], assumes similar orientation to that of the parent molecules on the HOPG surface. Of what remains that can possibly induce spin-state locking is the methyl-mediated interaction — possibly through the formation of hydrogen bonding and/or Van der Waals forces — between the molecules and the HOPG substrate. Any interaction force strong enough to prevent molecule contraction — a reduction in the Fe–N bond lengths by about 0.2 Å — will effectively prevent HS to LS state conversions. Molecular packing will be the main factor responsible for the loss of spin crossover in those molecules not in direct contact with the HOPG surface. It should be pointed out that — albeit not presented here — [Fe(H$_2$B(pz)$_2$)bipy], upon adding two and four methyl groups to the bipyridine ligand, exhibit similar spin-crossover behaviour to that of the correspondingly similar [Fe(H$_2$B(pz)$_2$)$_2$(phen−me$_2$)] and [Fe(H$_2$B(pz)$_2$)$_2$(phen−me$_4$)] molecules on HOPG surface.

5.2.1 Bulk and thin film spin-crossover behaviour of daughter molecule

The new molecule [Fe(H$_2$B(pz)$_2$)$_2$(phen−me$_4$)] — referred to as the daughter molecule — was synthesized and the temperature-induced spin transition in the bulk was measured by our collaborators at Christian-Albrecht Universität (CAU), Kiel (AG-Tuczek) by magnetic susceptibility measurements; this is shown in Fig. 5.5. The sample exhibits a gradual spin transition with χ_MT values ranging from 3.56 cm^3 K mol^{-1} at 300 K to 0.27 cm^3 K mol^{-1} at 5 K, and a transition temperature $T_{1/2}$ of 141 K; this behaviour is similar to that of the parent molecule functionalized with dimethyl groups at the phenanthroline ligand [63]. The temperature-induced spin-transition behaviour can be described by a Boltzmann distribution, indicating the absence of cooperative behaviour in the spin-transition processes.

Thin films of [Fe(H$_2$B(pz)$_2$)$_2$(phen−me$_4$)] are prepared on a quartz substrate; the complex is evaporable at 175řC at a pressure of 3×10^{-2} mbar, and at 165řC in the UHV pressure of 10^{-8} mbar. The temperature-induced spin transition in the thin film is traced by UV/vis absorption spectra, which is shown in Fig.5.6 (left-

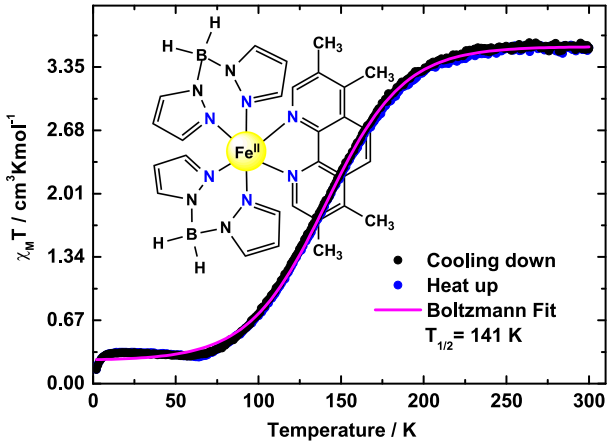

Figure 5.5: Spin-crossover behaviour of the daughter molecule in the bulk. Variation of χ_MT as a function of temperature, for the bulk sample of [Fe(H_2B(pz)$_2$)$_2$(phen−me$_4$)], during cooling (black dots), and heating (blue dots). The magenta line is the Boltzmann fit to the data. The SQUID measurement is carried out by AG–Tuczek at CAU-Kiel

panel). The spectra at 298 K and at 5 K show contrasting patterns: the MLCT bands at 298 K are characterized by a single broad peak at around 530 nm, which then evolved to the more intense double peak centred at 539 and 600 nm on lowering the temperature to 5 K. The spectra at any intermediate temperature can be generated by linearly combining the spectra at 298 and 5 K. Similar spectral patterns at similar temperatures have also been observed for a thin film of the parent complex [Fe(H_2B(pz)$_2$)phen] [62]; this is an indication for the thermal-induced spin transition from the HS state at 298 K to the LS ground state at 5 K.

Fig. 5.6 (left-panel, green line) shows the spectrum at 5 K of vacuum-evaporated thin film sample after illumination with light of wavelength 519 nm for 5 min; the spectrum assumes a pattern similar to that recorded at 298 K due to the conversion of the molecules from the LS to the HS state. The temperature-dependent spin-crossover curve of the thin film sample is shown in Fig. 5.6 (right-panel); the spin transition is rather gradual but can still be approximated with a Boltzmann fit — much like the bulk behaviour (Fig. 5.3) — albeit the transition temperature $T_{1/2}$ of 148 K being slightly greater than that of the latter (141 K). The light-induced metastable HS state can be converted to the LS ground state on raising the temperature to 70 – 80 K (Fig. 5.6 (right-panel, green line)), showing the reversibility in the spin state transitions.

5.2.2 Daughter molecules on Au(111)

One of the motivation in functionalizing the phenanthroline ligand with methyl groups is to see if it can help preserve the integrity as well as the spin-crossover behaviour of the molecule upon adsorption on Au(111). Fig. 5.7 shows the Fe L_3-edge XA spectra of 0.6 ML of [Fe(H_2B(pz)$_2$)$_2$(phen−me$_4$)] deposited on Au(111)

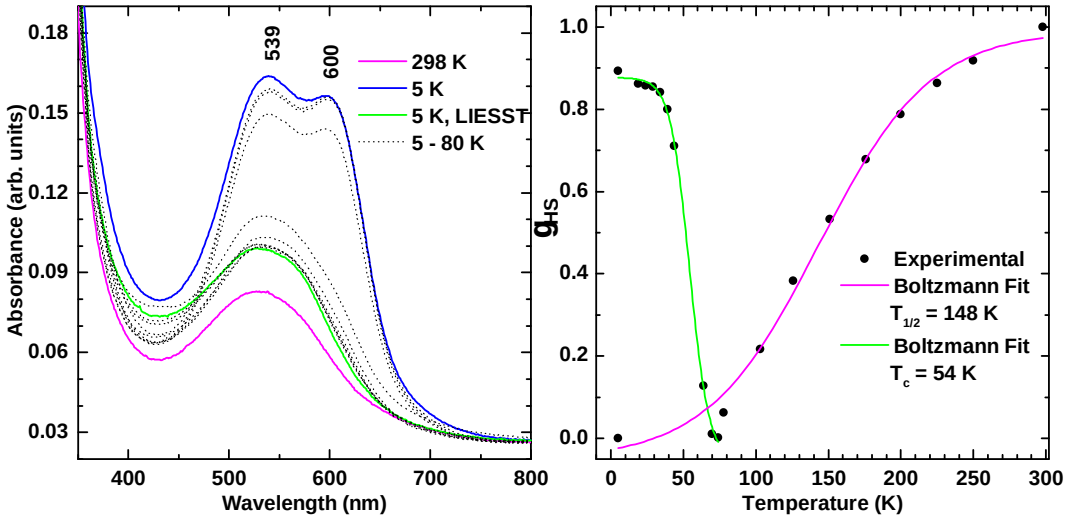

Figure 5.6: Spin-crossover behaviour of the daughter molecule in thin film, prepared on a quartz substrate. Left-panel: The UV/vis spectra of a vacuum-deposited film of $[Fe(H_2B(pz)_2)_2(phen-me_4)]$ on a quartz substrate on varying temperature ranging from 298 K (magenta line) to 5 K (blue line); the spectrum representing the light-induced metastable HS state at 5 K is shown in green colour. The grey lines represent the thermal-induced spin relaxation of the metastable HS state at 5 K to the LS ground state on raising the temperature to 70 — 80 K. Right-panel: the quantified HS fractional variation with temperature along with the Boltzmann fit (magenta line). The measurements are carried out by AG–Tuczek at CAU-Kiel

substrate, recorded at 300 and 40 K; both the spectra are characterized by similar spectral profiles with a single peak at 708.1 eV, without any multiplet structures. This is a clear departure from spectral patterns of molecules deposited on an HOPG substrate, or that of the bulk material. The nature of the molecule is further probed with scanning tunnelling microscopy (STM).

STM is a powerful technique for investigating the local structure and the spin-crossover behaviour; molecules in HS state have higher conductivity and larger size, as compared to those in the LS state. With this, the molecules in the two different spin states can be differentiated from the STM topography. Our collaborators from Christian-Albrecht Universität Kiel, AG-Berndt, performed STM measurements of a submonolayer of $[Fe(H_2B(pz)_2)_2(phen-me_4)]$ deposited on Au(111). Fig. 5.8 (a) shows a typical constant-current topography of a submonolayer of the complex $[Fe(H_2B(pz)_2)_2(phen-me_4)]$ deposited on Au(111) surface at ambient conditions, with the images recorded at 4.5 K in an ultra-high vacuum chamber. Two distinct types of molecular image is identified: (1) one structure consists of two bright protrusions (0.30(0.01) nm), and a relatively shallow bean-shaped structure at one end (marked by solid-circle in Fig. 5.8 (a)); (2) the other — marked by a dashed circle in Fig. 5.8 (a) — has a symmetric two-bean-shaped features.

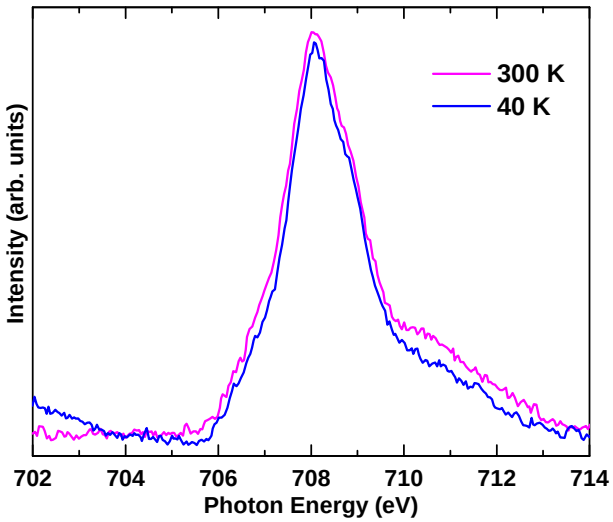

Figure 5.7: XAS of the daughter molecule on Au(111). Fe L_3 XA spectra of 0.6 ML [Fe(H_2B(pz)$_2$)$_2$(phen−me$_4$)] deposited on Au(111), recorded at 300 K (magenta), and 40 K (blue)

In an investigation of the parent molecule [Fe(H_2B(pz)$_2$)phen] deposited on Au(111), the two bean-shaped structures have been shown to be due to two phenanthroline molecules arranged in the form of a dimer [72]. By analogy, the similar structure observed here is concluded as being due to two phen-me$_4$ molecules arranged in the same manner. In addition, phen-me$_4$ appears to be about 0.4 nm longer than phenanthroline, which is consistent with the presence of four methyl molecules. Density functional theory (DFT) calculations of the constituents of the complex [Fe(H_2B(pz)$_2$)$_2$(phen−me$_4$)], namely, [Fe(H_2B(pz)$_2$)] and phen-me$_4$, and their interactions in the gas phase was performed by our collaborators in order to ascertain the other structure shown in Fig. 5.8 (b) [98]. The DFT-calculated gas-phase structures of isolated [Fe(H_2B(pz)$_2$)] and phen-me$_4$ are shown in fig. 5.8 (c); they are arranged in a bimolecular cluster which can be snugly overlaid onto the STM image of Fig. 5.8 (b) — phen-me$_4$ ligand as the bean-shaped structure, and the bright and protruding part attributable to [Fe(H_2B(pz)$_2$)]. The brightness of [Fe(H_2B(pz)$_2$)] is due to the molecule being in the HS state [72]. The calculated length of 0.64 nm of [Fe(H_2B(pz)$_2$)] is in good agreement with the STM-measured length of 0.63 nm.

The arrangements of phen-me$_4$ and [Fe(H_2B(pz)$_2$)], and their interactions in the gas phase is further explored using the DREIDING force-field calculations [98]. This results in phen-me$_4$—[Fe(H_2B(pz)$_2$)] distance as 1.15 nm, which is close to the STM-measured distance of 1.17(6) nm. Thus, the combined STM-XAS measurements of the complex [Fe(H_2B(pz)$_2$)$_2$(phen−me$_4$)] on Au(111), showed conclusively that the complex dissociate into phen-me$_4$ and [Fe(H_2B(pz)$_2$)] parts. We attribute the substrate-induced dissociation of the complex as being due to dispersion interaction between them. This conclusion is in line with a recent theoretical

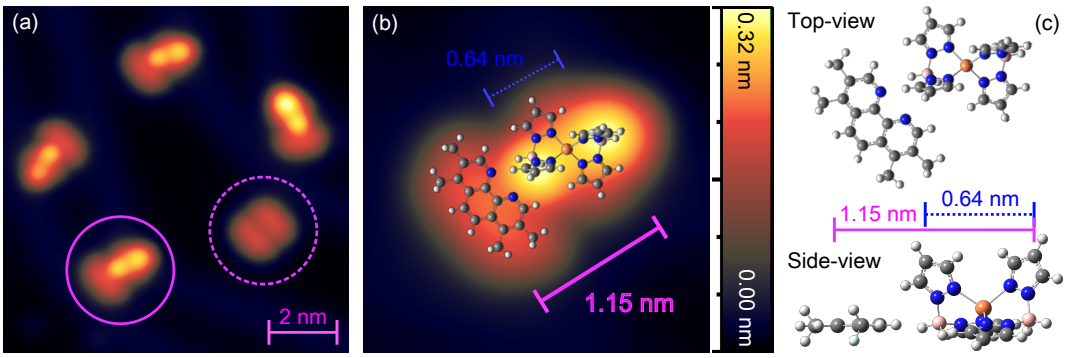

Figure 5.8: STM topography recorded at 4.5 K in ultra-high vacuum. (a) Constant-current topography of $[Fe(H_2B(pz)_2)_2(phen-me_4)]$ deposited on Au(111) at ambient temperature; (b) Zoom-in of the image under the solid circle in (a); and (c) Top and side views of the calculated structure of $[Fe(H_2B(pz)_2)]$ and phen-me_4 interacting in the gas phase, where two characteristic lengths are indicated. The calculated structure can be superimposed onto the STM image in (b). The measurements are carried out by AG–Berndt at CAU-Kiel

work that shows that dispersion interaction can indeed influence the relative stability of molecules on metal surfaces [119].

5.3 Parent and daughter molecules on Bi(111)

Bi is a semi-metal with low density of states at the Fermi level [120]; this allowed a reduction in the van der Waal's interaction of the substrate with molecules like spiropyran — and help retained their photo-reactivity on the surface, which is otherwise not possible on other metal surfaces [121]. This led us to think that Bi(111) surface could also preserve the spin-crossover behaviour. Fig. 5.9 shows the Fe L_3 XA spectra of the parent molecule $[Fe(H_2B(pz)_2)phen]$ (left-panel) and the daughter molecule $[Fe(H_2B(pz)_2)_2(phen-me_4)]$ (right-panel), each of 0.3 ML coverage, deposited on Bi(111) surface. Both the molecules exhibit an identical two-peak spectral profile — fingerprint of dominant HS state — at 300 K (magenta lines). On decreasing the temperature to 60–70 K, the characteristic LS peak at 709.3 eV emerged, with a concomitant reduction in the intensity at 708.1 eV corresponding to the HS state — a sign of the spin-state switching. Moreover, the intensity corresponding to the HS and the LS states of the spectra for both the molecules are almost identical at 60–70 K (blue lines, Fig. 5.9) — an indication of similar amount of molecules losing/retaining their spin-crossover behaviour.

Measuring the spin fractional variation with temperature can reveal a great deal on the nature of the spin transition processes. Accordingly, the Fe L_3 XA spectra are recorded at different temperatures on cooling the sample from 300 K to low temperatures, for 0.3 ML of each of the complexes $[Fe(H_2B(pz)_2)phen]$ and $[Fe(H_2B(pz)_2)_2(phen-me_4)]$ deposited on B(111) substrate. Fig. 5.10 (dots) shows

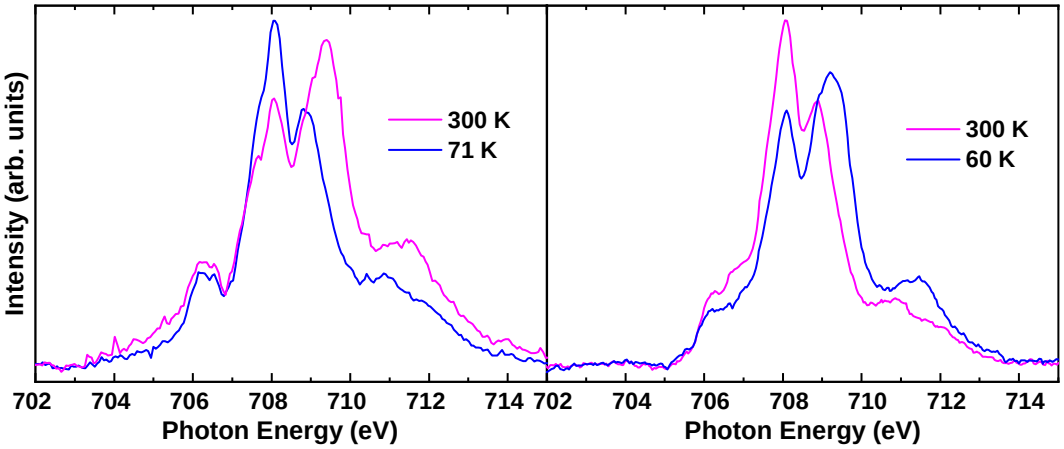

Figure 5.9: XAS of the molecules on Bi(111). Fe L_3 XA spectra of 0.3 ML each of [Fe(H_2B(pz)$_2$)phen] (left panel) and [Fe(H_2B(pz)$_2$)$_2$(phen−me$_4$)] (right panel) deposited on HOPG; magenta and blue lines indicate the room-temperature and low-temperature spectra, respectively

the HS fraction γ_{HS} variation with temperature of [Fe(H_2B(pz)$_2$)phen](right-panel) and [Fe(H_2B(pz)$_2$)$_2$(phen−me$_4$)](left panel). The spin fractions are calculated from a reference HS and LS spectra of 0.4 ML of [Fe(H_2B(pz)$_2$)phen] deposited on an HOPG surface — where it undergoes complete HS to LS state switching with both temperature and light [31]. By linearly combining the reference HS and LS spectra, any other spectral profile can be generated. The reference spectra are shown in Fig. 5.11 (a); and as an example, the corresponding fits to the room- and low-temperature (60 K) spectra of 0.3 ML of [Fe(H_2B(pz)$_2$)$_2$(phen−me$_4$)] is shown in Fig. 5.11 (b)&(c), respectively. By this procedure, the [Fe(H_2B(pz)$_2$)phen]−Bi(111) system is estimated to be composed of 88(5)% HS, decreasing to 46(5)% at 71 K — the maximum amount of states at low temperatures before the onset of SOXIESST; for [Fe(H_2B(pz)$_2$)$_2$(phen−me$_4$)]−Bi(111) system, the spin compositions are estimated as 95(5)% HS at 300 K and 51(5)% HS at 60 K. This co-existence in the spin states or the partial spin-state switching is quite a common occurrence for molecules in direct contact with solid surfaces, so much so that it came to be regarded as the true thermodynamic phase by some researchers [76], yet others speculating it to be a property intrinsic to spin-crossover molecules upon direct contact with solid surfaces [74].

The thermodynamics of the spin transition can be extracted from the van't Hoff's model, given by the following equation:

$$\gamma_{HS} = a + (1-a)\left(e^{\left(\frac{\Delta H}{RT} - \frac{\Delta S}{R}\right)} + 1\right)^{-1} \tag{5.1}$$

where a is the fraction of molecules trapped in the HS state, ΔH and ΔS are the enthalpy and entropy difference between the HS and the LS states, respectively; and R is the universal gas constant. From the fit of the experimental

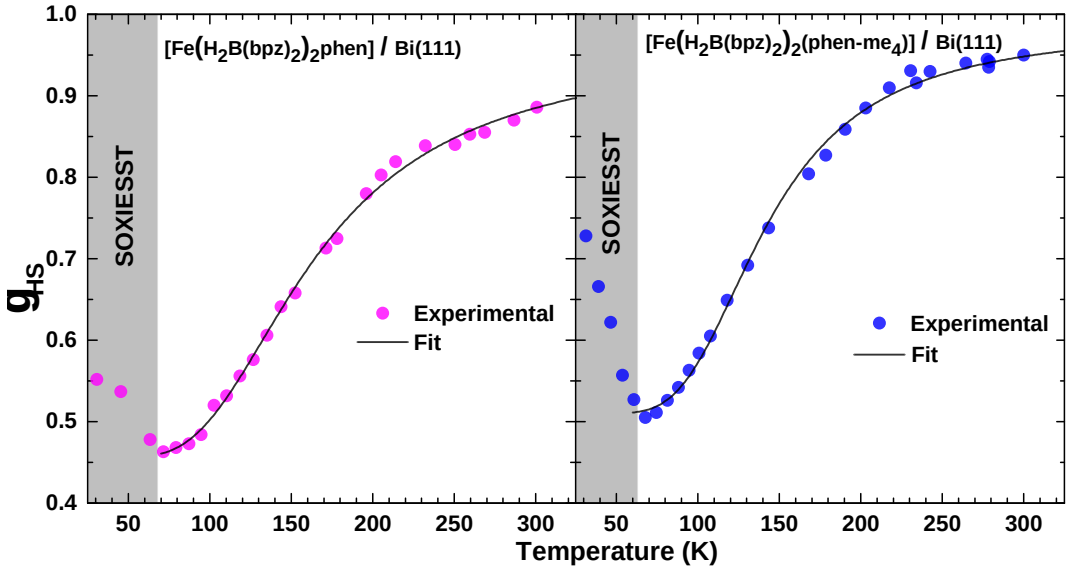

Figure 5.10: Temperature-dependent spin transition on Bi(111). The variation of γ_{HS} with temperature of [Fe(H_2B(pz)$_2$)phen] (left panel) and [Fe(H_2B(pz)$_2$)$_2$(phen−me$_4$)] (right panel) deposited on Bi(111), each of 0.3 ML coverage. The spin transition fittings are done treating the systems as non-interacting

data between 300 and 70(60) K, respectively, ΔH is estimated as 4.6(1) and 5.1(1) kJ mol^{-1}, and ΔS as 26.3(6) and 34.6(8) J K^{-1} mol^{-1}, for [Fe(H_2B(pz)$_2$)phen] and [Fe(H_2B(pz)$_2$)$_2$(phen−me$_4$)] , respectively. The temperature-independent high-spin fraction a amounts to 46(5)% for [Fe(H_2B(pz)$_2$)phen] and 51(5)% for [Fe(H_2B(pz)$_2$)$_2$(phen−me$_4$)] .

Both the complexes exhibit a pronounced x-ray as well as light-induced spin-state switching from the LS to the HS state; x-ray-induced LS→HS switching are shown in Fig. 5.10 in the shaded regions, at the left-panel for [Fe(H_2B(pz)$_2$)phen] and at the right-panel for [Fe(H_2B(pz)$_2$)$_2$(phen−me$_4$)]. The light-induced LS→HS switching of [Fe(H_2B(pz)$_2$)$_2$(phen−me$_4$)] on Bi(111) is shown in Fig. 5.12 (left-panel); illumination at 17 K for < 1 min with a wavelength of 520 nm under a photon flux of 2.5(5)$\times 10^{17}$ photons s^{-1} cm^{-2} increases the high-spin fraction from 48(5)% to 94(5)%. Upon further illumination the population remains constant. From an exponential fit, the time constant for the light-induced switching process under these conditions is estimated as 2.1(1) s. It should be noted that the spectra were recorded on a virgin position of the sample that had not been exposed to X-rays before in order to start with minimum SOXIESST.

Although no time-dependent measurements have been performed for [Fe(H_2B(pz)$_2$)phen] under illumination, clear evidence of LIESST effect is obtained for this molecule deposited on Bi(111) as well. Fig. 5.12 (right-panel) shows XA spectra at the Fe L_3 edge for the pristine sample at 5 K (magenta) and after 7 min illumination (blue) with a wavelength of 520 nm under a photon flux of 4.0(8)$\times 10^{16}$

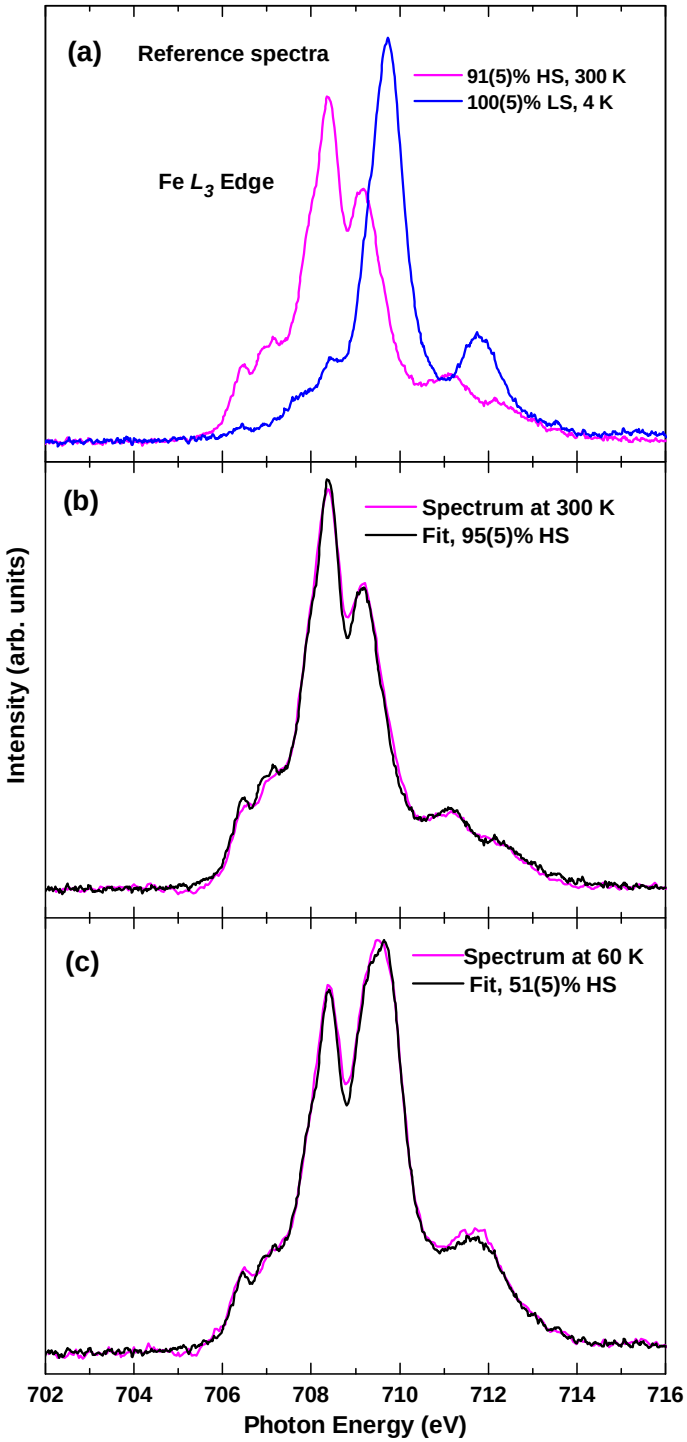

Figure 5.11: Estimation of the HS fraction from reference spectra. (a) Reference HS and LS spectra: room-temperature spectrum (magenta line) and the spectrum at 5 K (blue line) of 0.4 ML of [Fe(H_2B(pz)$_2$)phen] on HOPG; (b) Room-temperature spectrum (magenta) and (c) Spectrum at 60 K (magenta) of 0.3 ML of [Fe(H_2B(pz)$_2$)$_2$(phen−me$_4$)] on Bi(111), and their corresponding fits (black lines) from a linear combination of the reference spectra. HS fractions at 300 K and at 60 K are estimated as 95(5)% and 51(5)%, respectively

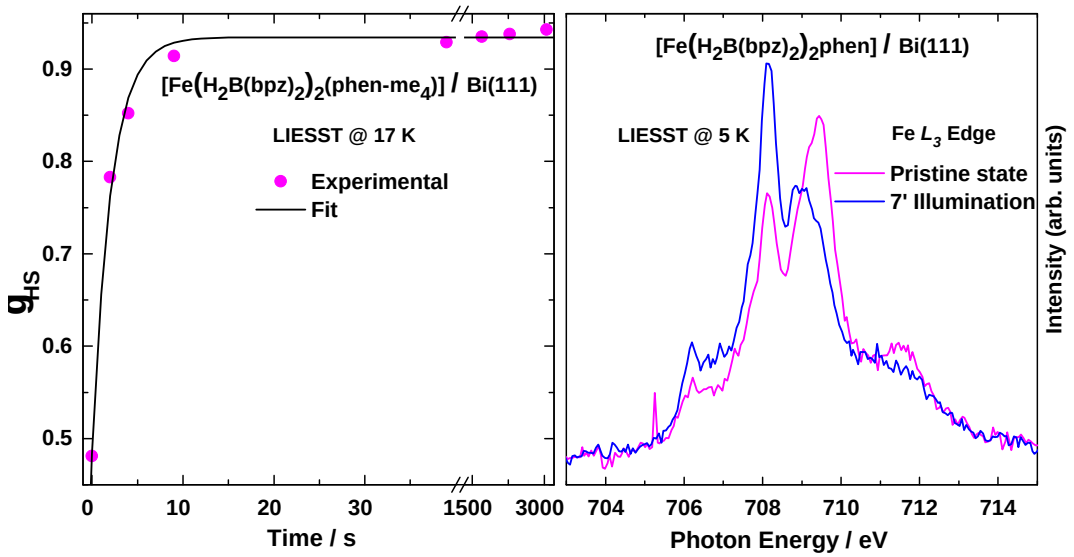

Figure 5.12: Light-induced excited spin-state trapping on Bi(111). Left panel: Light-induced LS-to-HS conversion curve of 0.3 ML of [Fe(H_2B(pz)$_2$)phen] deposited on Bi(111) at 17 K; Right-panel: Fe L_3 XA spectrum before (magenta) and after illumination (blue) at 5 K of 0.3 ML of [Fe(H_2B(pz)$_2$)phen] deposited on Bi(111)

photons $s^{-1}cm^{-2}$. At 5 K in the pristine state, γ_{HS} is determined as 48(5)%; after 7 min illumination, it increases to 80(5)%.

5.4 Molecular orientations on Au, Bi and HOPG

The molecular orientation on different surfaces can be determined from the N *K*-edge XA spectra recorded at two different angles between the surface and the electric field polarization vector of a linearly polarized x ray [122]. It is based on the premise that the x-ray absorption intensity is dependent on the degree of overlap between the electric field vector of the x ray and the localized/non-localized π^* bonds. For example, if the N-atom bond(s) are confined to a certain plane, and if it lies flat or close to the surface — implying the π^* orbital planes lying perpendicular to the surface — then the N *K*-edge XA recorded with its electric field vector close to the surface normal will yield higher intensity as compare to that recorded at an angle away from it; from the ratio of these two intensities, the molecular orientation can be computed.

5.4.1 Parent–molecule orientation on HOPG

Calculation of the molecular orientation by the procedure as outlined in the preceding paragraph is complicated for bulky compounds like SCMs consisting of several N atoms, and the N bonds not confined to any particular plane. As an example, the closely-related SCMs [Fe(H_2B(pz)$_2$)phen] and [Fe(H_2B(pz)$_2$)bipy] — both having similar crystal structure in the bulk — have altogether 10 N atoms; the

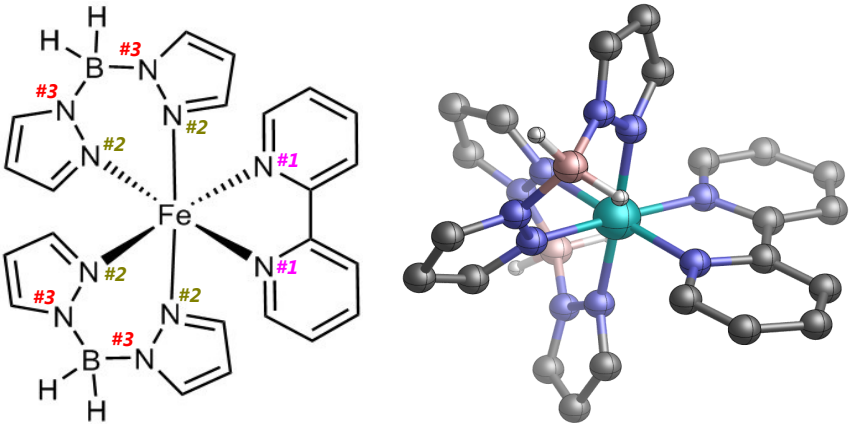

Figure 5.13: Chemical structure of [Fe(H_2B(pz)$_2$)bipy]. 2D (left panel) and 3D (right panel) chemical structure of [Fe(H_2B(pz)$_2$)bipy] in the bulk. The N atoms are numbered from 1—3 based on their binding energies, giving rise to the three characteristic peaks in the N *K*-edge spectral profile

chemical structure of [Fe(H_2B(pz)$_2$)bipy] is shown in Fig. 5.13. The 10 N atoms can be grouped into 3 based on their binding energies: 2 N atoms from the phenanthroline ligand (marked as #1 in the Figure), 4 N atoms from pyrazole ligands in direct coordination with the Fe-atom (#2), and 4 others not in direct coordination with the Fe-atom (#3), also from the pyrazole ligands.

Nevertheless, one can obtain a qualitative idea about the molecular orientation from the angle-dependent measurements of the N *K*-edge spectra. First, the angle-dependent N *K*-edge spectra of both the molecules [Fe(H_2B(pz)$_2$)phen] and [Fe(H_2B(pz)$_2$)bipy] on HOPG — of about 0.3 and 0.6 ML, respectively — are presented; this is shown in Fig. 5.14. The spectra are recorded at normal (90ř) and grazing (30ř and 25ř) between the surface normal and the electric field vector of the x-ray beam. As expected of a stable molecule, all spectral profiles consists of three peaks corresponding to the N atoms grouped into 3 based on their chemical environments. In the literature [72], it is reported that the first peak at 399.2 eV is due to the two N atoms from the phenanthroline ligand (marked #1 in Fig. 5.13); the other two peaks at 400.6 and 401.4 eV are due to the N atoms from the two pyrazole ligands (marked #2 & #3 in Fig. 5.13).

By a brief glance at the angle-dependent N *K*-edge spectra of Fig. 5.14, one can immediately arrive at a couple of conclusions on the nature of the molecular assembly on the HOPG surface: (i) Both the molecules are preferentially oriented on the surface, as indicated by the difference in peak intensities, when recorded at normal and grazing angles; (ii) Both the molecules have roughly similar orientation on the surface, as indicated by similar intensity-ratio of all the three peaks, between grazing- and normal-angled spectra. This observation is hardly surprising, as both the molecules exhibit similar behaviour on the HOPG surface — undergoing com-

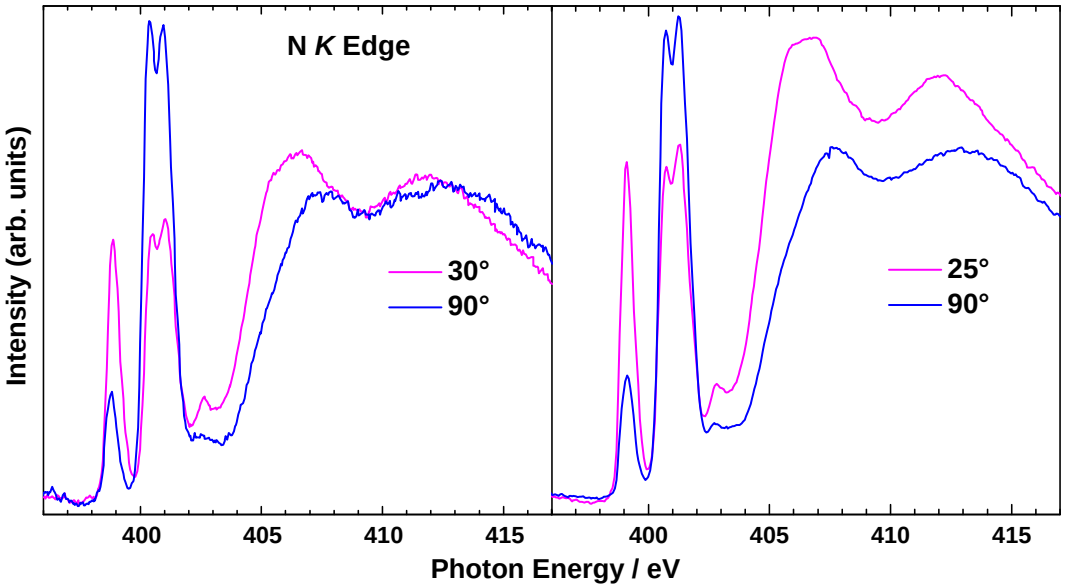

Figure 5.14: Orientation of the parent molecules on HOPG. Left panel: Room-temperature N *K*-edge XA spectra of 0.3 ML of [Fe(H_2B(pz)$_2$)phen] on HOPG; Right panel: Room-temperature N *K*-edge XA spectra of 0.6 ML of [Fe(H_2B(pz)$_2$)bipy] on HOPG. The magenta- and blue-coloured spectra are recorded at grazing (30ř and 25ř) and normal (90ř) between the surface normal and the electric field vector of the linearly polarized x-ray beam

plete spin-state transition with light and temperature [31, 65]. The orientation of the phenanthroline ligand from the N *K*-edge spectral peak at 399.2 eV can be estimated quantitatively, as the bonds of two N atoms of the phenanthroline ligand are confined to the plane of the ligand itself (*c.f.* Fig. 5.13). Thus, the plane of the phenanthroline ligand is estimated to lie 39(5)ř in the case of [Fe(H_2B(pz)$_2$)phen], and 38(5)ř for the in of [Fe(H_2B(pz)$_2$)bipy] — both *w.r.t.* the HOPG surface.

With regard to the two pyrazole ligands, their preferential orientation on the surface is also evident, as can be seen from the difference in the intensities of the peaks at 400.6 and 401.1 eV of the spectra recorded at grazing and normal angles. However, quantifying the orientation angle *w.r.t.* the surface — as is done in the case of phenanthroline ligand — is complicated, as the N atoms grouped as #2 and #3, cannot be associated with any particular, well-defined plane. It is safe to assume, however, that both [Fe(H_2B(pz)$_2$)phen] and [Fe(H_2B(pz)$_2$)bipy] complexes on the HOPG surface retained the octahedral arrangements of the FeN_6 core — as any other symmetry will result in the loss of SC property. Thus, the N *K*-edge XA spectral profiles of [Fe(H_2B(pz)$_2$)phen] and [Fe(H_2B(pz)$_2$)bipy] on HOPG surface; the asymmetry in the spectral intensity recorded at grazing and normal angles between the surface normal and the electric polarization vector of the x ray, as shown in Fig. 5.14, can be taken as the fingerprint of the molecules preserving their octahedral symmetry and hence retaining their spin-state bistability. This conclu-

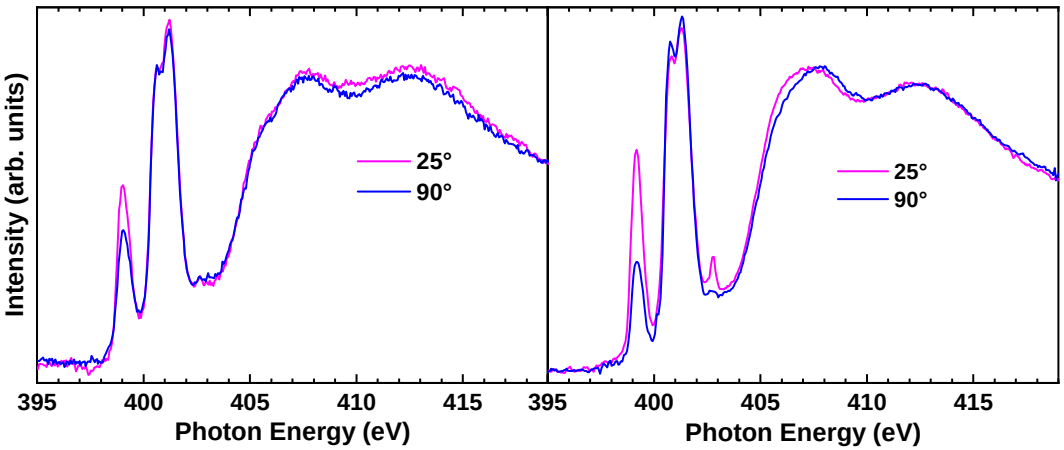

Figure 5.15: Orientation on Bi(111). Room-temperature N *K*-edge spectra of 0.3 ML each of [Fe(H_2B(pz)$_2$)phen] (left panel) and [Fe(H_2B(pz)$_2$)$_2$(phen−me$_4$)] (right panel), deposited on a Bi(111) surface, taken at grazing (25ř) and the normal angles between the surface normal and the electric field vector of the x-ray beam

sion is supported by the N *K*-edge spectra measured for [Fe(H_2B(pz)$_2$)phen] and [Fe(H_2B(pz)$_2$)$_2$(phen−me$_4$)] deposited on Bi(111), given in the following sections.

5.4.2 Parent– and daughter–molecule orientations on Bi(111)

To recall, both the molecules [Fe(H_2B(pz)$_2$)phen] and [Fe(H_2B(pz)$_2$)$_2$(phen−me$_4$)] exhibit identical spin-crossover behaviour on Bi(111) surface — in terms of the nature of both temperature- and light-induced spin-state switching, and the amount of molecules that retain their spin-state bistability, as shown in Fig. 5.10 & 5.12. A qualitative measure of the molecular orientation of a submonolayer of both the molecules — by means of their angle-dependent N *K*-edge XA spectra between the surface normal and the electric field vector of the linearly polarized x-ray beam — are recorded to further shed some light on their spin-crossover behaviour; this is shown in Fig. 5.15.

As can be seen, the N *K*-edge XA spectra of both the samples — [Fe(H_2B(pz)$_2$)phen] and [Fe(H_2B(pz)$_2$)$_2$(phen−me$_4$)], each of 0.3 ML on Bi(111) — exhibit similar spectral profiles, reflecting the similarity in their spin-crossover behaviour. The phenanthroline ligand orientation — calculated from the intensity ratio of the peak at 399.2 eV, between the spectra recorded at 25ř and 90ř — is estimated to lie at 49(5)ř *w.r.t.* Bi(111) surface in the case of [Fe(H_2B(pz)$_2$)phen], and at 44(5)ř in the case of [Fe(H_2B(pz)$_2$)$_2$(phen−me$_4$)]. On the other hand, the intensity of the peaks at 400.6 and 401.4 eV for both the samples — arising from the N atoms of the two pyrazole ligands — are independent of the measurement angles. This can be due to two factors: either the pyrazole ligands (and the molecules) are randomly distributed on the surface and with no preferential orientation, or that the two pyrazole ligands lie exactly at/close-to the so-called magic angle (54.7ř) [122].

Although it is not clear which of the above mentioned factors are responsible, there is a case to be made for the random orientation of molecules as being the dominant factor — if not the only factor — giving rise to the observed spectral profile, from the point of view of the geometrical symmetry of SCMs. Preserving the octahedral symmetry of the FeN_6 core — responsible for spin-state bistability — give rise to a definite orientation of the molecules on a surface (Fig. 5.14); molecules assuming any other geometry or distorted away from the octahedral symmetry will result in the loss of spin-crossover behaviour. By this argument, it is easy to explain the spin-state co-existence of both the molecules $[Fe(H_2B(pz)_2)phen]$ and $[Fe(H_2B(pz)_2)_2(phen-me_4)]$ at low temperatures on Bi(111) surface: molecules retaining their spin-state bistability and undergoing spin-state transition are the ones whose octahedral symmetry of the FeN_6 core is preserved, and those trapped in the HS state at all temperatures — about 50% for either molecules — are the ones without this symmetry. The distribution of molecules with and without the octahedral symmetry of their FeN_6 core give rise to an overall random orientation of the molecules on the surface. However, it should be noted that preserving the octahedral symmetry of molecules on surfaces is a necessary, but not sufficient condition for retaining the spin-crossover behaviour, as will be shown in the case of $[Fe(H_2B(pz)_2)_2(phen-me_4)]$ on an HOPG surface.

5.4.3 Daughter–molecule orientation on Au and HOPG

To re-state, the SCM $[Fe(H_2B(pz)_2)_2(phen-me_4)]$ is trapped in the HS state at all temperatures on both Au(111) and on HOPG surfaces — but due to different reasons — as can be inferred from their respective Fe L_3-edge spectral profiles: it consists of just one peak on Au(111) (Fig. 5.7), and two peaks on HOPG (Fig. **??**). The different routes by which the molecule lose the spin-crossover behaviour is revealed vividly from the N *K*-edge XA spectral profiles; these are shown in Fig. 5.16 — the left panel shows the spectra measured at grazing (25ř) and normal (90ř) angles — as it is in the previous cases — of 0.4 ML on HOPG, and the right panel that of 0.6 ML on Au(111) surfaces.

On the HOPG surface, the N *K*-edge XA spectra is strikingly similar in almost every aspects to that of the parent molecules $[Fe(H_2B(pz)_2)phen]$ and $[Fe(H_2B(pz)_2)bipy]$ on the same substrate (*c.f* Fig. 5.14). Moreover, the room-temperature Fe L_3 spectral profile of $[Fe(H_2B(pz)_2)_2(phen-me_4)]$ on HOPG (*c.f* Fig. 5.14, with the associated multiplet structures, are similar in every aspects to that of the parent molecules on the same substrate at the same temperature [31, 65]. Based on these similarities, one can make the following conclusions: (i) The octahedral symmetry of the FeN_6 core is preserved for $[Fe(H_2B(pz)_2)_2(phen-me_4)]$ on HOPG, as is the case with the parent molecules, (ii) There is no observable difference(s) between $[Fe(H_2B(pz)_2)_2(phen-me_4)]$ and the parent molecules on HOPG surface at room-temperature — both in terms of their orientation or the spin-state.

Given this, how do one account for the loss of spin-state bistability in

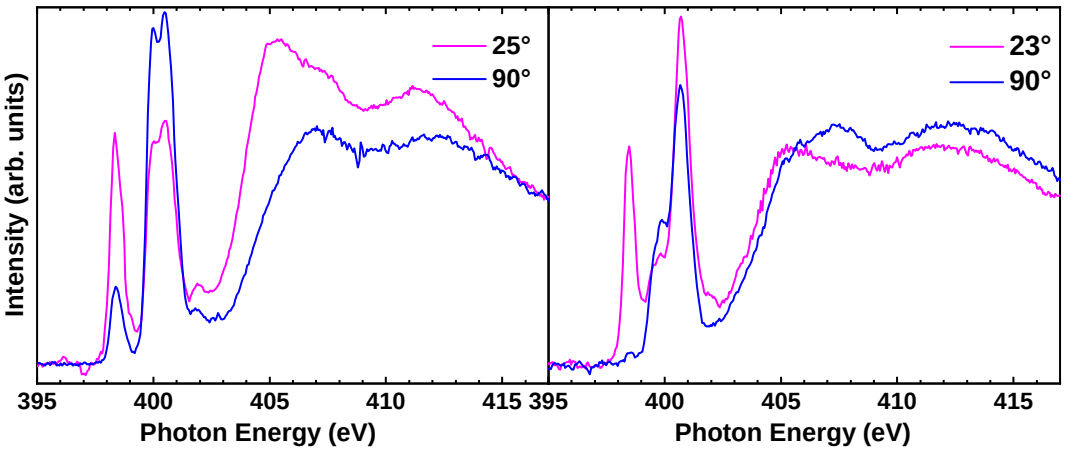

Figure 5.16: Orientation [Fe(H_2B(pz)$_2$)$_2$(phen−me$_4$)] on HOPG and Au(111). Room-temperature N *K*-edge spectra of 0.3 ML each of [Fe(H_2B(pz)$_2$)phen] (left panel) and [Fe(H_2B(pz)$_2$)$_2$(phen−me$_4$)] (right panel), deposited on an Au(111) surface, taken at the grazing (25ř) and the normal angles between the surface normal and the electric field vector of the x-ray beam

[Fe(H_2B(pz)$_2$)$_2$(phen−me$_4$)] on HOPG, while the same is preserved in the case of the parent molecules on the same substrate? Based on the results obtained from the XAS measurements — as outlined above — the answer may lie on the enhanced interaction between the [Fe(H_2B(pz)$_2$)$_2$(phen−me$_4$)] and the HOPG surface, hindering the contraction of the molecules so as to assume the LS state. [2] It is clear that the enhanced molecule-substrate interaction would solely arise from compounds added to [Fe(H_2B(pz)$_2$)$_2$(phen−me$_4$)], namely, the four methyl groups functionalized to the phenanthroline ligand — the chemical structure of [Fe(H_2B(pz)$_2$)$_2$(phen−me$_4$)] is shown as the inset of Fig. 5.5. These methyl-mediated interaction between the molecule and the substrate could be either/both through the formation of hydrogen-bonding and van der Waal's interactions.

For 0.6 ML of [Fe(H_2B(pz)$_2$)$_2$(phen−me$_4$)] on a Au(111) substrate, the N *K*-edge XA spectrum recorded at grazing angle (25ř) is characterized by three π^* resonances at 399.2, 400.6 and 401.4 eV; for the spectrum recorded at 90ř angle, the resonance at 399.2 eV vanishes, as shown in Fig. 5.16 (left panel). This is due to the fragmentation of the molecule into the HS [Fe(H_2B(pz)$_2$)] and phen-me$_4$ ligand; the latter is calculated to lie flat on the surface. This is agreement with the STM investigations, already presented in section 5.2.2. The parent molecule [Fe(H_2B(pz)$_2$)phen] is also found to be fragmented into [Fe(H_2B(pz)$_2$)] and phenanthroline components on the same surface [72] . Thus, the addition of four methyl compounds has no effect in terms of preserving the molecules' integrity or the spin-crossover behaviour upon adsorption on Au(111) surface.

[2] SCMs undergo volume contraction in the LS state, and *vice-versa* in the HS state

"Words can be meaningless — if they are used in such a way that no sharp conclusions can be drawn."

— Richard P. Feynman

CONCLUSIONS AND OUTLOOK

From the investigation of x-ray-induced spin switching at 5 K of 0.8 ML of [Fe(H_2B(pz)$_2$)bipy] deposited on an HOPG surface, it is clear that x rays can induce a change in the chemical structure of SCMs, apart from switching the spin state. This is observed to be highly dependent upon the photon flux; by maintaining the photon flux in the region of 10^9 photons s^{-1} mm^{-2}, the spin switching can be greatly suppressed, and the chemical alteration avoided altogether. These findings are highly relevant in view of the importance of x ray-based techniques in probing SCMs. To further advance this field of research — SCMs on solid surfaces — finding new non-invasive techniques, or applying the already known suitable techniques in investigating submonolayer or monolayer of molecules deposited on surfaces, such as differential reflectance spectroscopy [123], would greatly help.

The complex [Fe(H_2B(pz)$_2$)bipy] when deposited on an HOPG substrate consistently retains its spin-crossover — induced both by temperature and light — at the coverages ranging from submonolayers to multilayers. This is remarkable in light of what is generally observed in surface deposited SCMs where the norm is either a partial or a complete loss of SCO property. However, the light-induced metastable HS state at low temperatures is unstable and follows a dramatic departure in the mode of spin relaxation to the ground LS state, in comparison to the bulk material. While in the bulk material, there are two clear temperature regimes of the spin relaxation — the low temperature regime of up-to 40 K where the photo-induced HS state is rather stable and the relaxation occurs *via* quantum tunnelling, and the thermally-activated regime (> 40 K) where the relaxation follows sigmoidal-type characteristics – no such demarcation of temperature regimes is observed in the case of [Fe(H_2B(pz)$_2$)bipy] molecules in direct contact with an HOPG surface; the HS-to-LS relaxation in the investigated range from 8—40 K follows a stretched-exponential curve.

The stretch-exponential relaxation can be modelled by introducing an interaction parameter α in the decay equation. The relaxation parameter α can be related to the interaction parameter Γ of the thermally-induced spin-crossover model of Slichter and Drickamer; they both have negative values, suggesting that in the submonolayer coverages on HOPG, the molecules undergo an anticooperative spin transition. From the thermal spin-crossover curve, a free-molecule-like behaviour is indicated, and only from the bilayer onwards, cooperative spin transition is ev-

idenced. Since the bistability and the occurrence of hysteresis are determined by cooperativity, it is desired — from a device–applications point of view — to have strongly cooperative spin transition starting from the monolayer.

One approach would be to add some ligands to the already known SCMs that preserved their SCO on surfaces, such as [Fe(H_2B(pz)$_2$)bipy] and [Fe(H_2B(pz)$_2$)phen] on HOPG reported in this thesis; the additional ligands to function as linkages between the molecular units and thereby promoting cooperative interactions. Methylation of the ligands, especially from the phen- and bipy-motif appeared to be not a good approach — addition of two methyls led to a partial spin switching, while four methyls led to the loss of SCO altogether on an HOPG surface. However, methylation of ligands have no effect on the nature of SCO behaviour on Au(111) and Bi(111) surfaces; the molecules still break-apart on Au(111), while only $\sim$50% retained their SCO on Bi(111), analogous to the behaviour of the non-methylated parent molecules.

The fundamental challenges faced with surface-deposited SCMs, namely, retaining the molecular integrity, the SCO phenomenon and avoiding spin-state coexistence at room- and low-temperatures, can be overcome by suitable molecule-substrate combinations; only that reports on such suitable combinations are rare. One reason for it is the scarcity of vacuum evaporable SCMs. The other reason is the variety, or the lack of, of substrates on which SCMs are investigated. HOPG is the only substrate — reported so far — on which SCMs can undergo 'clean' spin-state transition with light and temperature.

BIBLIOGRAPHY

[1] T. L. Friedman: *Moore's law turns 50*. in: New York Times, (2015). 1

[2] S. Anthony: *IBM unveils worlds first 5 nm chip*. in: Ars Technica, (2017). 1

[3] M. M. Waldrop: *The chips are down for Moore's law*. in: Nature, (2016). 1

[4] N. A. Spaldin: *Fundamental Materials Research and the Course of Human Civilization*. in: arXiv:1708.01325, (2017). 1, 2

[5] M. Ellis: *Gadgets and Gigawatts: Policies for energy efficient electronics*. (2009). 2

[6] S. A. Wolf, D. D. Awschalom, R. A. Buhrman, J. M. Daughton, S. von Molnár, M. L. Roukes, A. Y. Chtchelkanova, and D. M. Treger: *Spintronics: A Spin-Based Electronics Vision for the Future*. Science **294**, 1488–1495 (2001), doi:10.1126/science.1065389. 2

[7] A. Fert: *Origin, Development, and Future of Spintronics (Nobel Lecture)*. Angew. Chem. Int. Ed. **47**, 5956-5967 (2008), doi:10.1002/anie.200801093.

[8] S.D. Bader and S.S.P. Parkin: *Spintronics*. Annu. Rev. Cond. Mat. Phys **1**, 71-88 (2010), doi:10.1146/annurev-conmatphys-070909-104123. 2

[9] S. Manipatruni, D. E. Nikonov, and I. A. Young: *Beyond CMOS computing with spin and polarization*. Nature Physics **14**, 338-343 (2018), doi:10.1038/s41567-018-0101-4. 2

[10] Q. Cao, S.-J. Han, J. Tersoff, A. D. Franklin, Y. Zhu, Z. Zhang, G. S. Tulevski, J. Tang, and W. Haensch: *End-bonded contacts for carbon nanotube transistors with low, size-independent resistance*. Science **350**, 68-72 (2015), doi:10.1126/science.aac8006. 2

[11] J. Glanz: *A Quantum Leap for Computers?*. Science **269**, 28–29 (1995), doi:10.1126/science.269.5220.28. 2

[12] S. Chen: *Atomic arrays power quantum computers*. Science **361**, 1300–1301 (2018), doi:10.1126/science.361.6409.1300.

[13] Editorial: *Classical and quantum computers are vying for superiority*. in: Nature, (2018). 2

[14] J. E. Moore: *The birth of topological insulators*. Nature **464**, 194 (2010), doi:10.1038/nature08916. 2

[15] C. Chappert, A. Fert, and F. N. Van Dau: *The emergence of spin electronics in data storage*. Nat. Mater. **6**, 813 (2007), doi:10.1038/nmat2024. 2

[16] D. Castelvecchi: *Europe shows first cards in €1-billion quantum bet*. in: Nature, (2018). 2

[17] A. Cho: *After years of avoidance, Department of Energy joins quest to develop quantum computers*. in: Science, (2018).

[18] G. Popkin: *Update: Quantum physics gets attentionand brighter funding prospectsin Congress*. in: Science, (2018). 2

[19] S. J. van der Moolen, R. Naaman, E. Scheer, J. B. Neaton, A. Nitzan, D. Natelson, N. J. Tao, H. van der Zant, M. Mayor, M. Ruben, M. Reed, and M. Calame: *Visions for a molecular future*. Nat. Nanotech. **8**, 385 (2013), doi:10.1038/nnano.2013.101. 2, 5

[20] A. Cornia and P. Seneor: *The molecular way*. Nat. Mater. **16**, 505 (2017), doi:10.1038/nmat4900. 2, 3

[21] M. Ratner: *A brief history of molecular electronics*. Nat. Nanotech. **8**, 378 (2013), doi:10.1038/nnano.2013.110. 2

[22] E. Lörtscher: *Wiring molecules into circuits*. Nat. Nanotech. **8**, 381 (2013), doi:10.1038/nnano.2013.105. 3

[23] M. Cinchetti, V. A. Dediu, and L. E. Hueso: *Activating the molecular spinterface*. Nat. Mater. **16**, 507 (2017), doi:10.1038/nmat4902.

[24] C. Barraud, P. Seneor, R. Mattana, S. Fusil, K. Bouzehouane, C. Deranlot, P. Graziosi, L. Hueso, I. Bergenti, V. Dediu, F. Petroff, and A. Fert: *Unravelling the role of the interface for spin injection into organic semiconductors*. Nat. Phys. **6**, 615 (2010), doi:10.1038/nphys1688.

[25] M. Galbiati, S. Tatay, C. Barraud, A. V. Dediu, F. Petroff, R. Mattana, and P. Seneor: *Spinterface: Crafting spintronics at the molecular scale*. MRS Bull. **39**, 602607 (2014), doi:10.1557/mrs.2014.131.

[26] J. R. Petta, S. K. Slater, and D. C. Ralph: *Spin-Dependent Transport in Molecular Tunnel Junctions*. Phys. Rev. Lett. **93**, 136601 (2004), doi:10.1103/PhysRevLett.93.136601.

[27] F. Al MaMari, T. Moorsom, G. Teobaldi, W. Deacon, T. Prokscha, H. Luetkens, S. Lee, G. E. Sterbinsky, D. A. Arena, D. A. MacLaren, M. Flokstra, M. Ali, M. C. Wheeler, G. Burnell, B. J. Hickey, and O. Cespedes: *Beating the Stoner criterion using molecular interfaces*. Nature **524**, 69 (2015). 3

[28] S. K. Kuppusamy and M. Ruben: *Emerging trends in spin crossover (SCO) based functional materials and devices*. Coord. Chem. Rev. **346**, 176-205 (2017). 3

[29] D. Aravena and E. Ruiz: *Coherent Transport through Spin-Crossover Single Molecules*. J. Am. Chem. Soc. **134**, 777-779 (2012), doi:10.1021/ja2090096. 3, 19

[30] A. C. Aragonés, D. Aravena, J. I. Cerdá, Z. Acís-Castillo, H. Li, J. A. Real, F. Sanz, J. Hihath, E. Ruiz, and I. Díez-Pérez: *Large Conductance Switching in a Single-Molecule Device through Room Temperature Spin-Dependent Transport*. Nano Lett. **16**, 218-226 (2016), doi:10.1021/acs.nanolett.5b03571. 3

[31] M. Bernien, H. Naggert, L. M. Arruda, L. Kipgen, F. Nickel, J. Miguel, C. F. Hermanns, A. Krüger, D. Krüger, E. Schierle, E. Weschke, F. Tuczek, and W. Kuch: *Highly Efficient Thermal and Light-Induced Spin-State Switching of an Fe(II) Complex in Direct Contact with a Solid Surface*. ACS Nano **9**, 8960-8966 (2015), doi:10.1021/acsnano.5b02840. 4, 17, 21, 29, 40, 42, 47, 64, 71, 72, 80, 85, 87

[32] L. Cambi and L. Szegő: *Über die magnetische Susceptibilität der komplexen Verbindungen*. Ber. Dtsch. Chem. Ges. **64**, 2591-2598 (1931). 8

[33] A. Hauser: *Ligand Field Theoretical Considerations*. in: Spin Crossover in Transition Metal Compounds I, edited by Gütlich, P. and Goodwin, H.A., Springer Berlin Heidelberg (2004), doi:10.1007/b13528. 8, 9, 10, 14

[34] R. C. Stoufer, D. W. Smith, E. A. Clevenger, and T. E. Norris: *Complexes of Cobalt(II). I. On the Anomalous Magnetic Behavior of Some Six-Coordinate Cobalt(II) Complexes*. Inorg. Chem. **5**, 1167-1171 (1966), doi:10.1021/ic50041a020. 8

[35] G. Navon and W. Klaeui: *Cobalt-59 NMR of a cobalt(III) spin-crossover compound*. Inorg. Chem. **23**, 2722-2725 (1984), doi:10.1021/ic00185a036. 8

[36] J. H. Ammeter, R. Bucher, and N. Oswald: *High-spin-low-spin equilibrium of manganocene and dimethylmanganocene*. J. Am. Chem. Soc. **96**, 7833-7835 (1974), doi:10.1021/ja00832a049. 8

[37] P. G. Sim and E. Sinn: *First manganese(III) spin crossover, first d4 crossover. Comment on cytochrome oxidase*. J. Am. Chem. Soc. **103**, 241-243 (1981), doi:10.1021/ja00391a067. 8

[38] D. M. Halepoto, D. G. L. Holt, L. F. Larkworthy, G. J. Leigh, D. C. Povey, and G. W. Smith: *Spin crossover in chromium(II) complexes and the crystal and molecular structure of the high spin form of bis[1,2-bis(diethylphosphino)ethane]di-iodochromium(II*. J. Chem. Soc., Chem. Commun., 1322-1323 (1989), doi:10.1039/C39890001322. 8

[39] S. Sugano, Y. Tanabe, and H. Kamimura: *Multiplets of transitionmetal ions in crystals*. Vol. 33, Academic Press (1970). 8, 10

[40] A. Real, J. Zarembowitch, O. Kahn, and X. Solans: *Magnetic interaction and spin transition in iron(II) dinuclear compounds. Crystal structure of (.mu.-2,2'-bipyrimidine)bis[(2,2'-bipyrimidine)bis(thiocyanato)iron(II)]*. Inorg. Chem. **26**, 2939-2943 (1987), doi:10.1021/ic00265a005. 11

[41] K. Boukheddaden, S. Miyashita, and M. Nishino: *Elastic interaction among transition metals in one-dimensional spin-crossover solids*. Phys. Rev. B **75**, 094112 (2007), doi:10.1103/PhysRevB.75.094112. 12

[42] H. Spiering: *Elastic Interaction in Spin-Crossover Compounds*. Vol. 235, Springer Berlin Heidelberg (2004), doi:10.1007/b95427. 12, 54

[43] G. D'Avino, A. Painelli, and K. Boukheddaden: *Vibronic model for spin crossover complexes*. Phys. Rev. B **84**, 104119 (2011), doi:10.1103/PhysRevB.84.104119. 12

[44] C. Timm: *Collective effects in spin-crossover chains with exchange interaction*. Phys. Rev. B **73**, 014423 (2006), doi:10.1103/PhysRevB.73.014423. 12

[45] H. Banerjee, M. Kumar, and T. Saha-Dasgupta: *Cooperativity in spin-crossover transition in metalorganic complexes: Interplay of magnetic and elastic interactions*. Phys. Rev. B **90**, 174433 (2014), doi:10.1103/PhysRevB.90.174433. 12

[46] M. Kepenekian, B. Le Guennic, and V. Robert: *Magnetic bistability: From microscopic to macroscopic understandings of hysteretic behavior using ab initio calculations*. Phys. Rev. B **79**, 094428 (2009), doi:10.1103/PhysRevB.79.094428. 12, 54, 56

[47] M. Kepenekian, B. Le Guennic, and V. Robert: *Primary Role of the Electrostatic Contributions in a Rational Growth of Hysteresis Loop in Spin-Crossover Fe(II) Complexes*. J. Am. Chem. Soc. **131**, 11498-11502 (2009), doi:10.1021/ja9031677. 12, 54

[48] C. P. Slichter and H. G. Drickamer: *Pressure Induced Electronic Changes in Compounds of Iron*. J. Chem. Phys. **56**, 2142-2160 (1972), doi:10.1063/1.1677511. 13, 56

[49] N. Moliner, L. Salmon, L. Capes, M. C. Muñoz, J. F. Létard, A. Bousseksou, J. P. Tuchagues, J. J. McGarvey, A. C. Dennis, and M. Castro: *Thermal and Optical Switching of Molecular Spin States in the [FeL[$H_2B(pz)_2$]$_2$] Spin-Crossover System (L = bpy, phen)*. J. Phys. Chem. B **106**, 4276 (2002), doi:10.1021/jp013872b. 13, 19, 42, 56, 57, 58, 59, 60, 66, 67, 71

[50] S. Decurtins, P. Gütlich, C.P. Köhler, H. Spiering, and A. Hauser: *Light-induced excited spin state trapping in a transition-metal complex: The hexa-1-propyltetrazole-iron (II) tetrafluoroborate spin-crossover system*. Chem. Phys. Lett. **105**, 1-4 (1984), doi:http://dx.doi.org/10.1016/0009-2614(84)80403-0. 13, 43, 63

[51] A. Hauser: *Reversibility of light-induced excited spin state trapping in the Fe(ptz)$_6$(BF_4)$_2$, and the $Zn_{1x}Fe_x$(ptz)$_6$(BF_4)$_2$ spin-crossover systems*. Chem. Phys. Lett. **124**, 543 - 548 (1986), doi:https://doi.org/10.1016/0009-2614(86)85073-4. 13

[52] G. Chastanet, M. Lorenc, R. Bertoni, and C. Desplanches: *Light-induced spin crossover—Solution and solid-state processes*. Comptes Rendus Chimie **21**, 1075-1094 (2018), doi:https://doi.org/10.1016/j.crci.2018.02.011. 13

[53] E. Buhks, G. Navon, M. Bixon, and J. Jortner: *Spin conversion processes in solutions*. J. Am. Chem. Soc. **102**, 2918-2923 (1980), doi:10.1021/ja00529a009. 15

[54] A. Hauser, J. Jeftić, H. Romstedt, R. Hinek, and H. Spiering: *Cooperative phenomena and light-induced bistability in iron(II) spin-crossover compounds*. Coord. Chem. Rev. **190-192**, 471-491 (1999), doi:https://doi.org/10.1016/S0010-8545(99)00111-3. 15, 16, 66, 67

[55] V. Mishra, R. Mukherjee, J. Linares, C. Balde, C. Desplanches, J.-F. Létard, E. Collet, L. Toupet, M. Castro, and F. Varret: *Temperature-Dependent Interactions and Disorder in the Spin-Transition Compound [Fe^{II}(L)$_2$][ClO_4]$_2$ůC$_7$H$_8$ Through Structural, Calorimetric, Magnetic, Photomagnetic, and Diffuse Reflectance Investigations*. Inorg. Chem. **47**, 7577-7587 (2008), doi:10.1021/ic8002977. 15, 67

[56] M. Cavallini: *Status and perspectives in thin films and patterning of spin crossover compounds*. Phys. Chem. Chem. Phys. **14**, 11867-11876 (2012), doi:10.1039/C2CP40879A. 16, 17

[57] H. Soyer, C. Mingotaud, M. L. Boillot, and P. Delhaes: *Spin Crossover of a Langmuir-Blodgett Film Based on an Amphiphilic Iron(II) Complex*. Langmuir **14**, 5890-5895 (1998), doi:10.1021/la9803934. 16

[58] M. Matsuda and H. Tajima: *Thin Film of a Spin Crossover Complex [Fe(dpp)$_2$](BF_4)$_2$*. Chem. Lett. **36**, 700-701 (2007), doi:10.1246/cl.2007.700. 16

[59] Y. Galyametdinov, V. Ksenofontov, A. Prosvirin, I. Ovchinnikov, G. Ivanova, P. Gütlich, and W. Haase: *First Example of Coexistence of Thermal Spin Transition and Liquid-Crystal Properties*. Angew. Chem., Int. Ed. **40**, 4269-4271 (2001), doi:10.1002/1521-3773(20011119)40:22<4269::AID-ANIE4269>3.0.CO;2-8. 16

[60] G. Molnár, S. Cobo, J.A. Real, F. Carcenac, E. Daran, C. Vieu, and A. Bousseksou: *A Combined Top-Down/Bottom-Up Approach for the Nanoscale Patterning of Spin-Crossover Coordination Polymers*. Adv. Mater. **19**, 2163-2167 (2007), doi:10.1002/adma.200700448. 17

[61] S. Shi, G. Schmerber, J. Arabski, J. B. Beaufrand, D. J. Kim, S. Boukari, M. Bowen, N. T. Kemp, N. Viart, G. Rogez, E. Beaurepaire, H. Aubriet, J. Petersen, C. Becker, and D. Ruch: *Study of molecular spin-crossover complex Fe(phen)$_2$(NCS)$_2$ thin films*. Appl. Phys. Lett. **95**, 043303 (2009), doi:10.1063/1.3192355. 17

[62] H. Naggert, A. Bannwarth, S. Chemnitz, T. von Hofe, E. Quandt, and F. Tuczek: *First Observation of Light-Induced Spin Change in Vacuum Deposited Thin Films of Iron Spin Crossover Complexes*. Dalton Trans. **40**, 6364 (2011), doi:10.1039/C1DT10651A. 76

[63] H. Naggert, J. Rudnik, L. Kipgen, M. Bernien, F. Nickel, L. M. Arruda, W. Kuch, C. Nather, and F. Tuczek: *Vacuum-evaporable spin-crossover complexes: physicochemical properties in the crystalline bulk and in thin films deposited from the gas phase*. J. Mater. Chem. C **3**, 7870-7877 (2015), doi:10.1039/C5TC00930H. 17, 37, 70, 75

[64] M. Bernien, D. Wiedemann, C. F. Hermanns, A. Krüger, D. Rolf, W. Kroener, P. Müller, A. Grohmann, and W. Kuch: *Spin Crossover in a Vacuum-Deposited Submonolayer of a Molecular Fe(II) Complex*. J. Phys. Chem. Lett. **3**, 3431-3434 (2012), doi:10.1021/jz3011805. 17, 21, 42

[65] L. Kipgen, M. Bernien, S. Ossinger, F. Nickel, A. J. Britton, L. M. Arruda, H. Naggert, C. Luo, C. Lotze, H. Ryll, F. Radu, E. Schierle, E. Weschke, F. Tuczek, and W. Kuch: *Evolution of cooperativity in the spin transition of an iron(II) complex on a graphite surface*. Nat. Commun. **9**, 2984 (2018), doi:10.1038/s41467-018-05399-8. 17, 23, 38, 55, 57, 71, 85, 87

[66] D. Collison, C. D. Garner, C. M. McGrath, J. F. W. Mosselmans, M. D. Roper, J. M. W. Seddon, E. Sinn, and N. A. Young: *Soft X-ray induced excited spin state trapping and soft X-ray photochemistry at the Iron $L_{2,3}$ edge in [Fe(phen)$_2$(NCS)$_2$] and [Fe(phen)$_2$(NCSe)$_2$] (phen = 1,10-phenanthroline)*. J. Chem. Soc., Dalton Trans., 4371-4376 (1997), doi:10.1039/A703728G. 17, 43, 45, 47

[67] L. Kipgen, M. Bernien, F. Nickel, H. Naggert, A. J. Britton, L. M. Arruda, E. Schierle, E. Weschke, F. Tuczek, and W. Kuch: *Soft-x-ray-induced spin-state switching of an adsorbed Fe(II) spin-crossover complex*. J. Phys.: Condens. Matter **29**, 394003 (2017). 17, 65, 66, 67

[68] T. G. Gopakumar, F. Matino, H. Naggert, A. Bannwarth, F. Tuczek, and R. Berndt: *Electron-Induced Spin Crossover of Single Molecules in a Bilayer on Gold*. Angew. Chem. Int. Ed. **51**, 6262–6266 (2012), doi:10.1002/anie.201201203. 17, 19, 49, 50, 71

[69] C. Cartier dit Moulin, P. Rudolf, A. M. Flank, and C. T. Chen: *Spin transition evidenced by soft x-ray absorption spectroscopy*. J. Phys. Chem. **96**, 6196-6198 (1992), doi:10.1021/j100194a021. 17, 42

[70] B. Warner, J. C. Oberg, T. G. Gill, F. El Hallak, C. F. Hirjibehedin, M. Serri, S. Heutz, M.-A. Arrio, P. Sainctavit, M. Mannini, G. Poneti, R. Sessoli, and P. Rosa: *Temperature- and Light-Induced Spin Crossover Observed by X-ray Spectroscopy on Isolated Fe(II) Complexes on Gold*. J. Phys. Chem. Lett. **4**, 1546-1552 (2013), doi:10.1021/jz4005619. 18, 20, 29, 64

[71] W. Kuch and M. Bernien: *Controlling the magnetism of adsorbed metalorganic molecules*. J. Phys.: Condens. Matter **29**, 023001 (2017). 18, 20

[72] T. G. Gopakumar, M. Bernien, H. Naggert, F. Matino, C. F. Hermanns, A. Bannwarth, S. Mühlenberend, A. Krüger, D. Krüger, F. Nickel, W. Walter, R. Berndt,

W. Kuch, and F. Tuczek: *Spin-Crossover Complex on Au(111): Structural and Electronic Differences Between Mono- and Multilayers*. Chem. Eur. J **19**, 15702-15709 (2013), doi:10.1002/chem.201302241. 18, 40, 69, 70, 71, 78, 84, 88

[73] J. A. Real, M. C. Muñoz, J. Faus, and X. Solans: *Spin Crossover in Novel Dihydrobis(1-pyrazolyl)borate [$H_2B(pz)_2$]-Containing Fe(II) Complexes. Synthesis, X-ray Structure, and Magnetic Properties of [FeL($H_2B(pz)_2)_2$] (L = 1,10-Phenanthroline and 2,2-Bipyridine)*. Inorg. Chem. **36**, 3008 (1997), doi:10.1021/ic960965c. 19, 37, 42, 55, 59, 71

[74] A. Pronschinske, Y. Chen, G. F. Lewis, D. A. Shultz, A. Calzolari, M. B. Nardelli, and D. B. Dougherty: *Modification of Molecular Spin Crossover in Ultrathin Films*. Nano Lett. **13**, 1429-1434 (2013), doi:10.1021/nl304304e. 19, 80

[75] S. Beniwal, X. Zhang, S. Mu, A. Naim, P. Rosa, G. Chastanet, J. F. Létard, J. Liu, G. E. Sterbinsky, D. A. Arena, P. A. Dowben, and A. Enders: *Surface-induced spin state locking of the [Fe($H_2B(pz)2)2(bipy)$] spin crossover complex*. J. Phys.: Condens. Matter **28**, 206002 (2016). 19, 20

[76] K. Bairagi, O. Iasco, A. Bellec, A. Kartsev, D. Li, J. Lagoute, C. Chacon, Y. Girard, S. Rousset, F. Miserque, Y. J. Dappe, A. Smogunov, C. Barreteau, T. Boillot, M.-L.and Mallah, and V. Repain: *Molecular-scale dynamics of light-induced spin cross-over in a two-dimensional layer*. Nat. Commun. **7**, 12212 (2016), doi:10.1038/ncomms12212. 20, 80

[77] P. Gütlich, A. Hauser, and H. Spiering: *Thermal and Optical Switching of Iron(II) Complexes*. Angew. Chem. Int. Ed. **33**, 2024-2054 (1994), doi:10.1002/anie.199420241. 20, 65

[78] K. Bairagi, A. Bellec, C. Fourmental, O. Iasco, J. Lagoute, C. Chacon, Y. Girard, S. Rousset, F. Choueikani, E. Otero, P. Ohresser, P. Sainctavit, M.-L. Boillot, T. Mallah, and V. Repain: *Temperature-, Light-, and Soft X-ray-Induced Spin Crossover in a Single Layer of FeII-Pyrazolylborate Molecules in Direct Contact with Gold*. J. Phys. Chem. C **122**, 727-731 (2018), doi:10.1021/acs.jpcc.7b11874. 20

[79] M. S. Alam, M. Stocker, K. Gieb, P. Müller, M. Haryono, K. Student, and A. Grohmann: *Spin-State Patterns in Surface-Grafted Beads of Iron(II) Complexes*. Angew. Chem. Int. Ed. **49**, 1159-1163 (2010), doi:10.1002/anie.200905062. 21

[80] B. T. Thole and G. van der Laan: *Branching ratio in x-ray absorption spectroscopy*. Phys. Rev. B **38**, 3158–3171 (1988), doi:10.1103/PhysRevB.38.3158. 21

[81] O. Kahn and C. J. Martinez: *Spin-Transition Polymers: From Molecular Materials Toward Memory Devices*. Science **279**, 44-48 (1998), doi:10.1126/science.279.5347.44. 21, 65

[82] M. Gruber, T. Miyamachi, V. Davesne, M. Bowen, S. Boukari, W. Wulfhekel, M. Alouani, and E. Beaurepaire: *Spin crossover in Fe(phen)$_2$(NCS)$_2$ complexes on metallic surfaces*. J. Chem. Phys. **146**, 092312 (2017), doi:10.1063/1.4973511. 22

[83] M. Gruber, V. Davesne, M. Bowen, S. Boukari, E. Beaurepaire, W. Wulfhekel, and T. Miyamachi: *Spin state of spin-crossover complexes: From single molecules to ultrathin films*. Phys. Rev. B **89**, 195415 (2014), doi:10.1103/PhysRevB.89.195415. 22

[84] S. Gueddida and M. Alouani: *Spin crossover in a single Fe(phen)$_2$(NCS)$_2$ molecule adsorbed onto metallic substrates: An ab initio calculation*. Phys. Rev. B **87**, 144413 (2013), doi:10.1103/PhysRevB.87.144413. 22

[85] K. S. Kumar, M. Studniarek, B. Heinrich, J. Arabski, G. Schmerber, M. Bowen, S. Boukari, E. Beaurepaire, J. Dreiser, and M. Ruben: *Engineering On-Surface Spin Crossover: Spin-State Switching in a Self-Assembled Film of Vacuum-Sublimable Functional Molecule*. Adv. Mater. **30**, 1705416 (2017), doi:10.1002/adma.201705416. 22, 23

[86] T. Miyamachi, M. Gruber, V. Davesne, M. Bowen, S. Boukari, L. Joly, F. Scheurer, G. Rogez, T. K. Yamada, P. Ohresser, E. Beaurepaire, and W. Wulfhekel: *Robust spin crossover and memristance across a single molecule*. Nat. Commun. **3**, 938 (2012), doi:10.1038/ncomms1940. 23

[87] T. Jasper-Toennies, M. Gruber, S. Karan, H. Jacob, F. Tuczek, and R. Berndt: *Robust and Selective Switching of an FeIII Spin-Crossover Compound on Cu_2N/Cu(100) with Memristance Behavior*. Nano Lett. **17**, 6613-6619 (2017), doi:10.1021/acs.nanolett.7b02481. 23

[88] S. Rohlf, M. Gruber, B. M. Flöser, J. Grunwald, S. Jarausch, F. Diekmann, Ma. Kalläne, T. Jasper-Toennies, A. Buchholz, W. Plass, R. Berndt, F. Tuczek, and K. Rossnagel: *Light-Induced Spin Crossover in an Fe(II) Low-Spin Complex Enabled by Surface Adsorption*. J. Phys. Chem. Lett. **9**, 1491-1496 (2018), doi:10.1021/acs.jpclett.8b00338. 23

[89] Hubell, J. H.: *Photon cross section compilation activity in the U. S. in the range 1 keV to 100 GeV*. J. Phys. Colloques **32**, C4-14-C4-20 (1971), doi:10.1051/jphyscol:1971403. 26

[90] H. Wende, Z. Li, A. Scherz, G. Ceballos, K. Baberschke, A. Ankudinov, J. J. Rehr, F. Wilhelm, A. Rogalev, D. L. Schlagel, and T. A. Lograsso: *Quadrupolar and dipolar contributions to x-ray magnetic circular dichroism at the Tb L3,2 edges: Experiment versus theory*. J. Appl. Phys. **91**, 7361-7363 (2002), doi:10.1063/1.1450792. 27

[91] J. Stöhr and H. C. Siegmann: *Magnetism From Fundamentals to Nanoscale Dynamics*. Springer Berlin/Heidelberg (2006), doi:10.1007/978-3-540-30283-4. 29

[92] E. Stavitski and F. M. F. de Groot: *The CTM4XAS Program for EELS and XAS Spectral Shape Analysis of Transition Metal L Edges*. Micron **41**, 687 (2010), doi:10.1016/j.micron.2010.06.005. 29

[93] Robert D. Cowan: *The theory of atomic structure and spectra*. University of California Press: Berkeley (1981). 29

[94] A. Uldry, F. Vernay, and B. Delley: *Systematic computation of crystal-field multiplets for x-ray core spectroscopies*. Phys. Rev. B **85**, 125133 (2012), doi:10.1103/PhysRevB.85.125133. 29

[95] J. Stöhr and D. A. Outka: *Determination of molecular orientations on surfaces from the angular dependence of near-edge x-ray-absorption fine-structure spectra*. Phys. Rev. B **36**, 7891 (1987), doi:10.1103/PhysRevB.36.7891. 30

[96] A. Galet, A. B. Gaspar, G. Agusti, M. C. Munoz, G. Levchenko, and J. A. Real: *Pressure Effect Investigations on the Spin Crossover Systems Fe[$(H_2B(pz)_2]_2$(bipy) and Fe[$(H_2B(pz)_2]_2$(phen)*. Eur. J. Inorg. Chem. **2006**, 3571-3573 (2006), doi:10.1002/ejic.200600517. 35, 42, 71

[97] M. Bernien: *X-Ray Absorption Spectroscopy of Fe Complexes on Surfaces: Electronic Interactions and Tailoring of the Magnetic Coupling*. Ph. D. thesis, Freie Universität Berlin, (2009). 37

[98] S. Ossinger, H. Naggert, L. Kipgen, T. Jasper-Toennies, A. Rai, J. Rudnik, F. Nickel, L. M. Arruda, M. Bernien, W. Kuch, R. Berndt, and F. Tuczek: *Vacuum-Evaporable Spin-Crossover Complexes in Direct Contact with a Solid Surface: Bismuth versus Gold*. J. Mater. Chem. C **121**, 1210-1219 (2017), doi:10.1021/acs.jpcc.6b10888. 37, 78

[99] H. C. Herper, M. Bernien, S. Bhandary, C. F. Hermanns, A. Krüger, J. Miguel, C. Weis, C. Schmitz-Antoniak, B. Krumme, D. Bovenschen, C. Tieg, B. Sanyal, E. Weschke, C. Czekelius, W. Kuch, H. Wende, and O. Eriksson: *Iron Porphyrin Molecules on Cu(001): Influence of Adlayers and Ligands on the Magnetic Properties*. Phys. Rev. B **87**, 174425 (2013), doi:10.1103/PhysRevB.87.174425. 39

[100] J. Stöhr: *NEXAFS Spectroscopy*. Vol. 25, Springer-Verlag: Berlin, Heidelberg (1992), doi:10.1007/978-3-662-02853-7. 39

[101] R. Nakajima, J. Stöhr, and Y. U. Idzerda: *Electron-yield saturation effects in L-edge x-ray magnetic circular dichroism spectra of Fe, Co, and Ni*. Phys. Rev. B **59**, 6421–6429 (1999), doi:10.1103/PhysRevB.59.6421. 39

[102] V. Davesne, M. Gruber, T. Miyamachi, V. Costa, S. Boukari, F. Scheurer, L. Joly, P. Ohresser, E. Otero, F. Choueikani, A. B. Gaspar, J. A. Real, W. Wulfhekel, M. Bowen, and E. Beaurepaire: *First glimpse of the soft x-ray induced excited spin-state trapping effect dynamics on spin cross-over molecules*. J. Chem. Phys. **139**, 074708 (2013), doi:10.1063/1.4818603. 45, 49

[103] E. Ludwig, H. Naggert, M. Kalläne, S. Rohlf, E. Kröger, A. Bannwarth, A. Quer, K. Rossnagel, L. Kipp, and F. Tuczek: *Iron(II) Spin-Crossover Complexes in Ultrathin Films: Electronic Structure and Spin-State Switching by Visible and Vacuum-UV Light*. Angew. Chem. Int. Ed. **53**, 3019-3023 (2014), doi:10.1002/anie.201307968. 47

[104] Eric Gullikson, X-Ray properties of the Elements. 47

[105] G. Vankó, F. Renz, G. Molnár, T. Neisius, and S. Kárpáti: *Hard-X-ray-Induced Excited-Spin-State Trapping*. Angew. Chem. Int. Ed. **46**, 5306-5309 (2007), doi:10.1002/anie.200604432. 47

[106] A. Hauser: *Intersystem crossing in Fe(II) coordination compounds*. Coord. Chem. Rev. **111**, 275-290 (1991), doi:http://dx.doi.org/10.1016/0010-8545(91)84034-3. 50

[107] W. Zhang, R. Alonso-Mori, U. Bergmann, C. Bressler, M. Chollet, A. Galler, W. Gawelda, R. G. Hadt, R. W. Hartsock, T. Kroll, K. S. Kjaer, K. Kubicek, H. T. Lemke, H. W. Liang, D. A. Meyer, M. M. Nielsen, C. Purser, J. S. Robinson, E. I. Solomon, Z. Sun, D. Sokaras, T. B. van Driel, G. Vanko, T.-C. Weng, D. Zhu, and K. J. Gaffney: *Tracking excited-state charge and spin dynamics in iron coordination complexes*. Nature **509**, 345-348 (2014), doi:10.1038/nature13252. 50, 63

[108] A. Cannizzo, C. J. Milne, C. Consani, W. Gawelda, C. Bressler, F. van Mourik, and M. Chergui: *Light-induced spin crossover in Fe(II)-based complexes: The full photocycle unraveled by ultrafast optical and X-ray spectroscopies*. Coord. Chem. Rev. **254**, 2677-2686 (2010), doi:http://dx.doi.org/10.1016/j.ccr.2009.12.007. 50, 63

[109] G. Poneti, M. Mannini, L. Sorace, P. Sainctavit, M.-A. Arrio, E. Otero, J. C.Cezar, and A. Dei: *Soft-X-ray-Induced Redox Isomerism in a Cobalt Dioxolene Complex*. Angew. Chem. Int. Ed. **49**, 1954-1957 (2010), doi:10.1002/anie.200906895. 50

[110] B. L. Henke, J. A. Smith, and D. T. Attwood: *0.1-10 keV x-ray-induced electron emissions from solids - Models and secondary electron measurements*. J. Appl. Phys. **48**, 1852-1866 (1977), doi:10.1063/1.323938. 50

[111] C. Wäckerlin, F. Donati, A. Singha, R. Baltic, S. Decurtins, S.-X. Liu, S. Rusponi, and J. Dreiser: *Excited Spin-State Trapping in Spin Crossover Complexes on Ferroelectric Substrates*. J. Phys. Chem. C **122**, 8202-8208 (2018), doi:10.1021/acs.jpcc.7b10941. 50, 51

[112] A. Bousseksou, G. Molnar, L. Salmon, and W. Nicolazzi: *Molecular spin crossover phenomenon: recent achievements and prospects*. Coord. Chem. Rev. **40**, 3313-3335 (2011), doi:10.1039/C1CS15042A. 54

[113] T. Palamarciuc, J. C. Oberg, F. El Hallak, C. F. Hirjibehedin, M. Serri, S. Heutz, J.-F. Letard, and P. Rosa: *Spin crossover materials evaporated under clean high vacuum and ultra-high vacuum conditions: from thin films to single molecules*. J. Mater. Chem. **22**, 9690-9695 (2012), doi:10.1039/C2JM15094H. 56, 59

[114] R. Zimmermann and E. König: *A model for high-spin/low-spin transitions in solids including the effect of lattice vibrations*. J. Phys. Chem. Solids **38**, 779-788 (1977), doi:https://doi.org/10.1016/0022-3697(77)90072-5. 56

[115] C. Cantin, J. Kliava, A. Marbeuf, and D. Mikaïlitchenko: *Cooperativity in a spin transition ferrous polymer: Interacting domain model, thermodynamic, optical and EPR study*. Eur. Phys. J. B **12**, 525-540 (1999), doi:10.1007/s100510051035. 56

[116] T. Groizard, N. Papior, B. Le Guennic, V. Robert, and M. Kepenekian: *Enhanced Cooperativity in Supported Spin-Crossover MetalOrganic Frameworks*. J. Phys. Chem. Lett. **8**, 3415-3420 (2017), doi:10.1021/acs.jpclett.7b01248. 56

[117] M. Mikolasek, G. Felix, W. Nicolazzi, G. Molnar, L. Salmon, and A. Bousseksou: *Finite size effects in molecular spin crossover materials*. New Journal of Chemistry **38**, 1834-1839 (2014), doi:10.1039/C3NJ01268A. 59

[118] C. Enachescu, J. Linares, F. Varret, K. Boukheddaden, E. Codjovi, S. G. Salunke, and R. Mukherjee: *Nonexponential Relaxation of the Metastable State of the Spin-Crossover System [Fe(L)$_2$](ClO$_4$)2ůH$_2$O [L = 2,6-Bis(pyrazol-1-ylmethyl)pyridine]*. Inorg. Chem. **43**, 4880-4888 (2004), doi:10.1021/ic049938+. 67

[119] J. C. F. Rodriguez-Reyes, C. G. F. Siler, W. Liu, A. Tkatchenko, C. M. Friend, and R. J. Madix: *van der Waals Interactions Determine Selectivity in Catalysis by Metallic Gold*. Journal of the American Chemical Society **136**, 13333-13340 (2014), doi:10.1021/ja506447y. 79

[120] P. Hofmann: *The surfaces of bismuth: Structural and electronic properties*. Progress in Surface Science **81**, 191-245 (2006), doi:https://doi.org/10.1016/j.progsurf.2006.03.001. 79

[121] G. Schulze, K. J. Franke, and J. I. Pascual: *Induction of a Photostationary Ring-Opening—Ring-Closing State of Spiropyran Monolayers on the Semimetallic Bi(110) Surface*. Phys. Rev. Lett. **109**, 026102 (2012), doi:10.1103/PhysRevLett.109.026102. 79

[122] J. Stöhr and D. A. Outka: *Determination of molecular orientations on surfaces from the angular dependence of near-edge x-ray-absorption fine-structure spectra*. Phys. Rev. B **36**, 7891-7905 (1987). 83, 86

[123] F. Nickel, M. Bernien, U. Lipowski, and W. Kuch: *Optical differential reflectance spectroscopy for photochromic molecules on solid surfaces*. Rev. Sci. Instrum. **89**, 033113 (2018), doi:10.1063/1.5019415. 89

List of acronyms

AEY	Auger electron yield
AFM	atomic force microscopy
AO	atomic orbital
BESSY	Helmholtz-Zentrum Berlin für Materialien und Energie (formerly Berliner Elektronenspeicherring-Gesellschaft für Synchrotronstrahlung mbH)
bipy	2,2′-bipyridine
DFT	density functional theory
ELIESST	electron-induced excited spin-state trapping
G	Gibb's free energy
HS	high spin
HOPG	Highly-oriented pyrolytic graphite
LED	light emitting diode
LFT	ligand field theory
LIESST	light-induced excited spin-state trapping
LS	low spin
me	CH_3
ML	monolayer or molecular layer
MLCT	Metal-to-ligand charge transfer state
MO	molecular orbital
NEXAFS	near-edge X-ray absorption fine structure
PEY	partial electron yield
phen	1,10-phenanthroline
pz	pyrazole
S	Total spin quantum number, also Haung-Rhys factor
SCMs	spin-crossover molecules
SCO	spin-crossover
SOXIESST	soft x-ray-induced excited state spin-state trapping
SQUID	superconducting quantum interference device
STM	scanning tunneling microscope
TEY	total electron yield
UHV	ultra high vacuum
UV/Vis	Ultra-violet/Visible

XA	x-ray absorption
XANES	X-ray absorption near-edge spectroscopy
XAS	x-ray absorption spectroscopy
XNLD	x-ray natural linear dichroism
XPS	x-ray photoelectron spectroscopy
γ_{HS}	High-spin fraction

LIST OF PUBLICATIONS

2018

• **L. Kipgen**, M. Bernien, S. Ossinger, F. Nickel, A. J. Britton, L. M. Arruda, H. Naggert, C. Luo, C. Lotze, H. Ryll, F. Radu, E. Schierle, E. Weschke, F. Tuczek, and W. Kuch: *Evolution of cooperativity in the spin transition of an iron(II) complex on a graphite surface*. Nat. Commun.**9**, 2984.

• F. Nickel, M. Bernien, D. Krüger, J. Miguel, A. J. Britton, L. M. Arruda, **L. Kipgen**, and W. Kuch: *Highly Efficient and Bidirectional Photochromism of Spirooxazine on Au(111)*. J. Phys. Chem. C **122**, 8031-8036.

2017

• **L. Kipgen**, M. Bernien, F. Nickel, H. Naggert, A. J. Britton, L. M. Arruda, E. Schierle, E. Weschke, F. Tuczek, and W. Kuch: *Soft-x-ray-induced spin-state switching of an adsorbed Fe(II) spin-crossover complex*. J. Phys.: Condens. Matter **29**, 394003.

• F. Nickel, M. Bernien, M. Herder, S. Wrzalek, P. Chittas, K. Kraffert, L. M. Arruda, **L. Kipgen**, and W. Kuch: *Light-induced photoisomerization of a diarylethene molecular switch on solid surfaces*. J. Phys.: Condens. Matter **29**, 374001.

• F. Nickel, M. Bernien, K. Kraffert, D. Krüger, L. M. Arruda, **L. Kipgen**, and W. Kuch: *Reversible Switching of Spiropyran Molecules in Direct Contact With a Bi(111) Single Crystal Surface*. Adv. Funct. Mater. **27**, 1702280.

• S. Ossinger, H. Naggert, **L. Kipgen**, T. Jasper-Toennies, A. Rai, J. Rudnik, F. Nickel, L. M. Arruda, M. Bernien, W. Kuch, R. Berndt, and F. Tuczek: *Vacuum-Evaporable Spin-Crossover Complexes in Direct Contact with a Solid Surface: Bismuth versus Gold*. J. Mater. Chem. C **121**, 1210-1219.

2015

• M. Bernien, H. Naggert, L. M. Arruda, **L. Kipgen**, F. Nickel, J. Miguel, C. F. Hermanns, A. Krüger, D. Krüger, E. Schierle, E. Weschke, F. Tuczek, and W. Kuch: *Highly Efficient Thermal and Light-Induced Spin-State Switching of an Fe(II) Complex in Direct Contact with a Solid Surface*. ACS Nano **9**, 8960-8966.

• H. Naggert, J. Rudnik, **L. Kipgen**, M. Bernien, F. Nickel, L. M. Arruda, W. Kuch, C. Nather, and F. Tuczek: *Vacuum-evaporable spin-crossover complexes: physicochemical properties in the crystalline bulk and in thin films deposited from the gas phase*. J. Mater. Chem. C **3**, 7870-7877.

CONFERENCE CONTRIBUTIONS

2018

• 10th Joint BER II and BESSY II User Meeting, Berlin; 05.—07.12.2018. Contribution: Poster, entitled *Evolution of cooperativity in the spin transition of an iron(II) complex on a graphite surface*

• European Conference on Molecular Spintronics (ECMolS 2018), Peñíscola – Spain; 21.—24.10.2018. Contribution: Poster, entitled *Evolution of cooperativity in the spin transition of an iron(II) complex on a graphite surface*

2017

• Ninth Joint BER II and BESSY II User Meeting, Berlin; 13.—15.12.2017. Contribution: Poster, entitled *Tuning the Spin-Crossover Behaviour of an Fe(II) Complex on Graphite with Methyl Groups*

• Operating Quantum States in Atoms and Molecules at Surfaces (QMol Conference 2017), Ascona – Switzerland; 10.—14.09.2017. Contribution: Poster, entitled *Tuning the Spin-Crossover Behaviour of an Fe(II) Complex on Graphite with Methyl Groups*

• DPG Spring Meeting of the Condensed Matter Section, Dresden; 19.—24.03.2017. Contribution: Poster, entitled *The Emegence of Cooperativity in the Coverage Dependent Temperature and Light Induced Spin State Switching of an Fe(II) Complex Adsorbed on a Graphite Surface*

2016

• Eight Joint BER II and BESSY II User Meeting, Berlin; 07.—09.12.2016. Contribution: Poster, entitled *Tuning the Spin-Crossover Behaviour of an Fe(II) Complex on Graphite with Methyl Groups*

• French-German Summer School on Molecular switches at the nanoscale, Mittelwihr – France; 04.—09.09.2016. Contribution: Poster, entitled *Thermal and Optical Spin-State Manipulation of Non-Interacting Fe(II) Complexes on Graphite and its Tuning by Ligand Modification*

• SFB658 Conference 2016: Molecular Switches and Functional Surfaces, Motzener See, Berlin; 10.—13.04.2016. Contribution: Poster, entitled *Thermal and Optical Spin-State Manipulation of Non-Interacting Fe(II) Complexes on Graphite and its Tuning*

by Ligand Modification

• 80th Annual Meeting of the DPG and DPG Spring Meeting, Regensburg; 06.—11.03.2016. Contribution: Talk, entitled *The Optical and Thermal Spin State Manipulation of [Fe(H_2B(pz)$_2$)bipy] and its Derivative Compounds on Graphite Surface*

2015

• Seventh Joint BER II and BESSY II User Meeting, Berlin; 09.—11.12.2015. Contribution: Poster, entitled *The Optical and Thermal Spin State Switching of [Fe(H_2B(pz)$_2$)bipy] on Surfaces*

• 2015 European School on Magnetism, Cluj-Napoca – Romania; 24.08—04.09.2015. Contribution: Poster, entitled *Investigation of Spin-Crossover Molecules [Fe(H_2B(pz)$_2$)phen] and F[Fe(H_2B(pz)$_2$)bipy] on Surfaces*

• 79th Annual Meeting of the DPG and DPG Spring Meeting, Berlin; 15.—20.03.2015. Contribution: Poster, entitled *XAS Study of the Spin-Crossover Molecules [Fe(H_2B(pz)$_2$)phen] and F[Fe(H_2B(pz)$_2$)bipy] on Surfaces*

SELBSTSTÄNDIGKEITSERKLÄRUNG (DECLARATION)

Hiermit erkläre ich, dass ich die vorliegende Arbeit mit dem Titel "X-Ray Investigation of Ultra-Thin Spin-Crossover Molecular Films" selbständig und nur unter Verwendung der angegebenen Literatur und Hilfsmittel angefertigt habe. Ich versichere, dass weder diese Arbeit noch Teile daraus in einem früheren Promotionsverfahren oder zur Erlangung eines anderen akademischen Grades eingereicht und dort angenommen oder für ungenügend befunden wurden.

(I hereby declare that my thesis entitled X-ray Investigation of Ultra-Thin Spin-crossover Molecular Films is the result of my own work, except where otherwise indicated. Further, this thesis contains no material that has been submitted previously, in whole or in part, for the award of any other academic degree or diploma.)

Berlin, en

Lalminthang Kipgen

ACKNOWLEDGEMENTS

First and foremost, I would like to thank Prof. Dr. Wolfgang Kuch for his guidance and for giving me the opportunity to pursue my PhD studies here in Berlin. I thank also Prof. Dr. Katharina Franke for kindly consenting to co-assess my thesis.

This thesis will not be the way it is — and definitely for the better! — without the help and guidance of the post-doc who's worked with me for the duration of my PhD studies; I couldn't thank him enough — Dr. Matthias Bernien. I would like to express my gratitude to all my colleagues who I share with the beamtimes at BESSY — in particular to Lucas Arruda, Andrew Britton, and Fabian Nickel.

I would like to thank my collaborators Holger Naggert and Sascha Ossinger from the group of Prof. Dr. Tuczek at Christian-Albrecht Universität, Kiel; all the spin-crossover molecules presented in this thesis were synthesized by them. I thank Torben Jasper-Tönnies from the group of Prof. Dr. Richard Berndt, also of Christian-Albrecht Universität, for the STM measurements. I highly appreciate the insightful — and often long — email correspondence I share with Prof. Dr. Felix Tuczek, together with Prof. Dr. Wolfgang Kuch and Dr. Matthias Bernien, while trying to make sense of the experimental results.

I would like to thank Marion Badow, Dr. Christian Frischkorn, and Irmhild Wegener for all their help. I gratefully acknowledge the financial support from the German research foundation (DFG) through SFB 658, SFB/TRR 227; and Physics Department, Freie Universität Berlin.

And, I thank my family for their constant support.